Fabrication and Characterisation of Bragg Grating Based Polymeric Optical Devices

ANDREAS POSPORI

Doctor Of Philosophy

– ASTON UNIVERSITY –

May 2017

ASTON UNIVERSITY

Fabrication and Characterisation of Bragg Grating Based Polymeric Optical Devices

ANDREAS POSPORI

Doctor Of Philosophy, 2017

Thesis Summary

The work presented in this thesis is mostly located in the field of polymer optical fibre (POF) based sensors. Polymeric materials are flexible, biocompatible, they have higher failure strain, and they have lower Young modulus compared with silica materials. The latter characteristic renders POF Bragg grating (POFBG) sensors more sensitive to fibre stress and pressure compared with the conventional silica based sensors. However, the POF technology is not mature enough and it has some drawbacks, including the high optical attenuation, poor fibre handling and connectorisation methods, and time-consuming POFBG inscription procedures. In this thesis, these issues are addressed. First, the attenuation effects on the performance of POFBG and Bragg grating based Fabry-Pérot (FP) interferometric sensors were comprehensively investigated and discussed. Then, POFBG inscriptions with the common He-Cd and the KrF laser systems were experimentally demonstrated. In the latter case, a POFBG inscription with only one laser pulse is presented for the first time, which is the fastest Bragg grating inscription time reported until now. A demountable POF connectorisation method with low connection loss and a simple, well-controlled thermal annealing process applied on POFBGs were also demonstrated in this thesis. The thermal annealing was initially used for multiplexing purposes due to the ability of fibre to shrink in length under specific thermal exposure. The fibre shrinkage can blue-shift the Bragg wavelength of the POFBG permanently. In this thesis, it is shown for the first time that shifting the Bragg wavelength to longer wavelengths permanently is also feasible. The fibre annealing was also used to improve the lifetime and the performance of POFBG devices. The sensors fabricated in this work were used to develop novel applications, such as ultrasound detection, liquid level monitoring, and direct erythrocyte concentration measurement.

Keywords: Polymer optical fibres, Bragg gratings, sensors, inscription, thermal annealing

This thesis is dedicated to my family for their endless support and love.

Acknowledgements

The research leading to these results has received funding from the People Programme (Marie Curie Actions) of the European Union's Seventh Framework Programme FP7/2007-2013/ under REA grant agreement No. 608382. This work was supported by Marie Curie Intra European Fellowships included in the 7th Framework Program of the European Union (projects PIEF–GA–2013–628604 and PIEF–GA–2011–302919). This work was funded by Fundação para a Ciência e Tecnologia (FCT)/MEC through national funds and when applicable co-funded by FEDER and PT2020 partnership agreement under the projects UID/EEA/50008/2013, and UID/CTM/50025/2013. We also acknowledge the financial support from FCT through the fellowships SFRH/BPD/109458/2015 and SFRH/BPD/76735/2011. This work was supported by the National Natural Science Foundation of China (NSFC) under Grants 61290312, 61107072, 61107073, and 61475032. It was also supported by the Program for Changjiang Scholars and Innovative Research Team in Universities of China (PCSIRT) and the "111 Project" of China Education Ministry.

Contents

List of Figures

List of Tables

1 Introduction

The work presented in this PhD thesis has been conducted in the framework of the project "Training and Research Involving Polymer Optical Devices" (TRIPOD), which was funded from the People Programme (Marie Curie Actions) of the European Union's Seventh Framework Programme FP7/2007-2013/ under REA grant agreement No 608382. The TRIPOD project is located in the field of optical fibre sensors and its purpose is to produce optimised Bragg grating sensors in polymer optical fibres efficiently and reliably, and improve the technology in general for enhanced commercial exploitation. The scientific team covers all aspects of the sensor fabrication path, from developing novel polymeric materials to fibre manufacturing, in-fibre sensor fabrication, and end-user applications for industrial companies. The work presented in this thesis is mostly focused on the fabrication process of the Bragg grating devices.

1.1 Thesis Topic and Motivation

Polymer optical fibre (POF) Bragg grating sensors have been extensively explored in this thesis. A typical fibre Bragg grating (FBG) structure is formed when the refractive index of the material is periodically modulated along the fibre core [1]. Thus, the propagating light partially reflects when it encounters layers of the material with a different refractive index. Each reflected wave interferes

with each other and the ones being in phase create a constructive interference in the opposite direction of the propagating light. The reflected light is centred at the Bragg wavelength, defined by the grating period and the introduced refractive index modulation in the material. The periodic refractive index modification is usually produced when a photosensitive material is deliberately exposed to a periodic intensity pattern created by interfering two ultraviolet (UV) laser beams [2].

The ability of the FBGs to act as mirrors can find applications in fibre lasers [3, 4] and their ability to act as optical band-stop filters can find applications in optical communications as dispersion compensators [5], wavelength-division multiplexers [6, 7], and Raman amplifiers [8, 9] to name a few. Bragg grating devices can be also used for sensing purposes [10, 11]. For example, any fibre straining or change of temperature can influence the period and the refractive index of the grating and the Bragg wavelength can be shifted. Therefore, the FBGs can be used as sensors and they can offer some advantages over the conventional electronic sensors. Optical fibre sensors can be used in remote distances due to the low fibre loss, they are immune to the electromagnetic interference enabling operation in environments with high electromagnetic noise (e.g. electrical motors), many sensors can be multiplexed along the fibre length, their small size allow them to be embedded for structural monitoring, and they can be used in harsh or explosive environments (e.g. fuel storage facilities, and radioactive areas) [12].

In the last three decades, the majority of the Bragg grating sensors were fabricated in silica optical fibres and they are commercially available for various application fields [13]. However recently, there is a motivation to fabricate Bragg grating sensors in POF due to the distinctive material properties of polymers compared with silica [14]. Polymeric materials have higher failure strain [15], flexibility in bending, and moderate biocompatibility with low injurious and toxic effects on biological systems [16]. The cytotoxicity level of each polymer material can vary depending on its chemical structure, including the type and the quantity of the residual monomers in the polymer [17]. Although the Pockels coefficients of polymers provide approximately 14% higher strain sensitivity to POF Bragg grating (POFBG) sensors compared with their silica counterparts [18], this difference is not adequate to motivate the use of POFBG sensors in strain detection applications, due to their other drawbacks. However, the lower Young modulus in polymers [19], renders POFBG sensors much more sensitive to fibre stress [20] and pressure [21] compared with silica sensors. For this reason, the POFBG devices become more attractive to be also used as acoustic wave sensors [22], with one potential application being the photoacoustic imaging. Besides the mechanical properties, there are some hydrophilic polymers, such as the poly(methyl methacrylate) (PMMA), that are able to absorb water. Sensors developed in this type of POF can be used in humidity monitoring applications [23]. The POFBGs also show enhanced temperature sensitivity due to the large thermo-optic coefficient of polymers [24]

compared with silica [25]. In addition, the thermo-optic coefficient of silica is positive, but for some polymeric materials it is negative, and the combination of silica and POFBG sensors can be used to independently measure temperature and strain [26], or temperature and humidity [27]. Another advantage of polymers is the ability to mix different organic compounds and chemically modify them in order to achieve some desirable material characteristics, such as nonlinearity enhancement [28], optical amplification [29], and selective response to specific biochemical species or any other chemical concentration [30].

1.2 Challenges and Thesis Objectives

Even though polymer has various advantages over silica material, POF technology is still not mature enough and various drawbacks exist, as a result the POFBG sensors were not at the start of this research commercially exploited. One of the main disadvantages of POF is its high optical attenuation; the typical PMMA optical fibres exhibit attenuation from 0.1 dB/m to 100 dB/m at 0.6 μm to 1.5 μm wavelength respectively [31]. Scientists tried to tackle this issue with some success, by producing a perfluorinated POF, commercially known as cyclic transparent optical polymer (CYTOP), which exhibit loss of 0.02 dB/m in the 1.5 μm wavelength region [32]. However, the attenuation is still higher than silica and there is still room of improvement. The reflectivity of Bragg gratings, especially fabricated in PMMA optical fibres, can be reduced by the fibre loss. The sensitivity of the Fabry-Pérot interferometric sensors can be also affected by the attenuation present in the interferometric cavity. For this reason, there is a need to fully understand the influence of the attenuation in POF devices. Therefore, a comprehensive system model has been developed to investigate the effect of the fibre loss on the POFBGs and Bragg grating based Fabry-Pérot sensors. This work is presented in chapter 3.

The first experimental objective of the thesis was to fabricate POFBG sensors in various types of POFs using the common He-Cd laser inscription system and the phase mask technique. This work is described in chapter 4, which also includes a novel method to fit the POF into a FC/PC demountable connector with low connection loss. Chapter 4 also demonstrates a novel methodology for POFBG multiplexing, where the Bragg wavelength can be tuned permanently to longer wavelengths. The sensors fabricated in the work described in chapter 4 were used by other researchers to develop novel applications (see chapter 7).

Another substantial challenge for researchers is to fully understand the photosensitivity mechanisms involved behind the photo-inscription process of POFBGs. The objective is to optimise the performance and reduce the fabrication time of sensors. The most common inscription wavelength is 325 nm and the typical exposure time is several tens of minutes [14]. One

way to increase photosensitivity is to add dopants in POFs. In 2015, it was shown that inscribing with a lower laser wavelength reduces the total POFBG inscription time [33]. The total inscription time was less than 30 seconds, which holds the record of the fastest inscription of POFBG until now. In this thesis, a POFBG inscription with only one KrF laser pulse was demonstrated for the first time. The pulse duration was only 15 ns, which indicates the total exposure time required to fabricate a POFBG. This is a breakthrough regarding the required photo-inscription time of a typical Bragg grating sensor. This work is presented in chapter 5.

An additional aim is to optimise the performance of the POFBG sensors. For example, the sensitivity of the sensors used in stress and force detection applications will increase when fibres with lower Young modulus are produced. In general, the material and optical properties of POF can be different depending on its polymerisation process, fibre drawing process and thermal history. Polymers are also viscoelastic materials, which means the strain and stress are not in phase when tension is applied. This characteristic introduces creep and hysteresis effects during the cyclic loading on the fibre, which reduce the accuracy of the POFBG sensor during strain monitoring [15]. One solution to reduce these effects is to apply a thermal treatment to the POF [34]. Thermal annealing was initially used for POFBG multiplexing purposes [35]. The ability of the POF to shrink in length when is exposed above the β-transition temperature of the polymer [36], causes the grating period to become smaller and the Bragg wavelength to blue shift permanently. Therefore, multiple POFBGs may be inscribed in the same fibre using only one phase-mask. At a later stage, the thermal annealing process was used to provide additional benefits to POFBG sensors, such as strain [37] and humidity [38] sensitivity enhancement, and longer operational range for temperature sensors [39]. In this thesis, we demonstrate that not only strain, but also force and stress sensitivities can be enhanced when thermal annealing is applied on the POFBG sensors. It is also shown that chemically etching POF to reduce its diameter can influence the performance of the POFBG sensors. The effects of the thermal annealing and chemical etching are demonstrated in chapter 6.

Another objective of this work was to record volume Bragg grating (VBG) devices (also called holograms) in PMMA bulk materials (see chapter 8). The aim is to investigate the possibility to inscribe VBG devices effectively and repeatable. The diffraction efficiency of the VBG is directly related with the introduced refractive index change in the material. Therefore, using the same exposure conditions in all cases, the photosensitivity difference between materials can be evaluated. Materials with higher photosensitivity are expected to show higher refractive index change. In this thesis, a comparison between phase mask and holographic fabrication techniques was made and evaluated. The final objective was to investigate the possibility to inscribe the smallest possible Bragg grating period. Ultimately, the smallest grating period that can be

produced equals half of the recorded wavelength. In this work, a VBG structure with period of 165 nm and Bragg wavelength of 485 nm in PMMA medium is demonstrated. This period is the lowest possible that can be inscribed with the He-Cd laser. The work reported in this thesis can be continued in the future to explore the influence of the size of grating period to the change of the refractive index introduced in the polymeric material. It is expected that as the period becomes shorter, the modulation of refractive index will be less due to the lower spatial recording resolution, which occurs due to the existence of the long polymer molecules.

The objectives of the work described in this thesis are:

1. Investigate the attenuation effects on POFBGs and Bragg grating based Fabry-Pérot sensors.
2. Inscribe POFBGs in various types of POFs with the He-Cd laser system.
3. Connectorise the POFBGs with connection loss less than 2 dB.
4. Multiplex the POFBG sensors using the thermal annealing process.
5. Inscribe POFBG devices with more than 90% reflectivity in less than 10 minutes.
6. Optimise the performance of POFBG sensors.
7. Distribute the sensors to other researchers in order to develop novel applications.
8. Investigate the possibility to effectively record volume Bragg gratings in PMMA materials.
9. Inscribe a Bragg grating structure with the shortest possible period.

1.3 Thesis Structure

In the current chapter, a brief introduction to the thesis topic, challenges and objectives has been presented. The following chapter presents the state of the art of POFs and Bragg gratings, including their historical development, characteristics, fabrication techniques and common sensing applications. The POFBGs and Bragg grating based Fabry-Pérot interferometric sensors are comprehensively presented in chapter 3. A system model has been developed in MATLAB to study the attenuation effects on the performance of Fabry-Pérot stress sensor when is formed with two uniform Bragg gratings. The model includes the loss factor along the physical length of the grating structures and along the interferometric cavity. Three different fibre materials are used as examples: PMMA, cyclic transparent optical polymer and fused silica. The sensors are also characterised in three different wavelength regions, where commercially components and detectors are readily available: 650 nm, 850 nm, and 1550 nm. However, the presented model

is not limited to these materials or wavelengths; it can be used to characterise any Bragg grating based device inscribed in one-dimensional optical medium with known mechanical and optical properties.

The chapter 4 shows experimentally various POFBG inscriptions that were performed in different types of POFs, utilising the common He-Cd laser system. It also demonstrates the method used to connectorise the POFBGs. After the fabrication, the POFBG sensors were multiplexed using the annealing method. Until now, the Bragg wavelength was possible to be tuned permanently only to shorter wavelengths. In chapter 4, it is demonstrated for the first time that tuning the Bragg wavelength permanently to longer wavelengths is also feasible.

The chapter 5 demonstrates experimentally the fabrication of POFBGs using the KrF laser system, which emits at 244 nm wavelength. The chapter introduce the first POFBG inscribed with only one UV laser pulse with duration of 15 ns. This is the fastest POFBG inscription reported until now. The grating was recorded in a single-mode PMMA optical fibre, with its core doped with benzyl dimethyl ketal for photosensitivity enhancement. The reflectivity of the POFBG was 98.4%. This work significantly improves the potential for commercial exploitation of the POFBG sensing technology.

The chapter 6 investigates the thermal annealing and chemical etching effects on strain, stress, and force sensitivities of POFBG sensors. A simpler, well-controlled and cost-effective POF annealing process is also demonstrated. It is previously reported in the literature that the annealing can improve the strain sensitivity of the POFBG sensors. In this work, it is shown for the first time that the stress and force sensitivities can be also improved by POF annealing. The influence of fibre etching on strain and stress sensitivities of POFBG sensors seems random and small. Despite that, the etching can be useful in applications used to detect force. In general, the thermal and chemical treatments can be used to enhance the performance of POFBG sensors.

The POFBG sensors produced with the He-Cd laser (described in chapter 4) were used by other researchers to develop novel applications, which are presented in chapter 7. The sensors were used for ultrasound detection, liquid level monitoring, and erythrocyte concentration detection. In chapter 8, there is a demonstration of the volume Bragg gratings inscription with the phase mask technique and the holographic method. In this work, a Bragg grating with very short period inscribed in polymeric materials has been reported. In chapter 9, there is a general discussion about the work presented in this thesis and there are some suggestions for future work in order to further improve the POFBG sensing technology.

2 Polymer Optical Fibres and Bragg Gratings

This chapter presents the state of the art of polymer optical fibre (POF) and Bragg grating devices. First, the historical development of POFs and their characteristics are mentioned. The types of Bragg gratings and their typical applications follow next, and at the end of the chapter, various fabrication techniques of the FBGs are comprehensively described.

2.1 Polymer Optical Fibres

This section presents the history of POF, its chemical, mechanical, and optical properties, and the current available handling and connectorisation techniques. At the end of this section, the photosensitivity mechanisms involved are comprehensively discussed.

2.1.1 Historical Development of Polymer Optical Fibres

The American chemical company DuPont introduced the first polymer optical fibre (POF) in 1967 at the same period when silica optical fibre (SOF) was suggested as a transmission medium for communication [40]. The first POF had a step index refractive index profile. The core and the cladding were made of poly(methyl methacrylate) (PMMA) and fluoropolymer, respectively. However, SOF prevailed over POF due to its much lower fibre loss and it has been widely used in

communication applications. POF received attention again after a few decades due to its different material properties. A Fabry-Pérot device in POF was first demonstrated in 1995 [41] and then other researchers followed by producing the first single-mode step-index POFs [42–44]. In the next years, the first microstructured POF was developed [45], which opened the route for easier POF customisation by giving the ability of simple production of different types of POFs for various applications. The most common material for POF fabrication is PMMA. However, materials such as polystyrene [46, 47], amorphous fluoropolymer (commercially known as CYTOP) [48, 49], various cyclic olefin copolymers (commercially known as TOPAS and ZEONEX) [30, 50, 51], and polycarbonate [52, 53] have been also used. In the work presented in this thesis, PMMA based POFs are mostly used and therefore the following discussion is mainly concentrated on this material type.

2.1.2 Characteristics of Polymer Optical Fibres

Chemical Properties

Polymer is an organic material with much longer molecules compared with the silica which is an inorganic material. Polymer is created when monomers are linked together by the help of the polymerisation initiator and the chain transfer agent. The initiator helps to start the polymerisation reaction and the chain transfer agent defines the length of the molecule chain [54]. The PMMA average molecular weight varies depending on the polymerisation process, but it is found that molecular weights between 60 000 and 100 000 are suitable for fibre drawing [44]. Other useful organic molecules can be incorporate in the host polymer or can be added as copolymers or dopants for non-linear properties enhancement [28], optical signal amplification [29], chemical species detection [30] and photosensitivity enhancement of the material [55]. The glass transition temperature of polymers is much lower than silica materials. For example, the glass transition temperature of PMMA is approximately 105 °C [56], while for silica is 1200 °C. Therefore, the drawing process of POFs requires much lower drawing temperatures than SOFs, which means cheaper fabrication procedures. The lower processing temperature of polymers can also enable new optical devices fabrication techniques, such as nanoimprint lithography [57]. However, having lower processing temperature limits the operational range of POF sensors when they are used in high temperature monitoring applications.

Mechanical Properties

PMMA belongs to the viscoelastic class of materials, with the Young modulus varying between 1.8 GPa and 3.3 GPa [58, 59], which is 22 to 40 times less than silica with Young modulus of

73 GPa [19]. Some tensile testing of single-mode PMMA POFs under different cycling loading conditions and strain rates is reported, with Young modulus being varying between 1.6 GPa to 5.0 GPa [60–62]. However, we need to note that the mechanical properties of POFs depend on their processing history, including the thermal history of performs [60, 63], fibre drawing conditions (drawing ratio, temperature, speed, tension, etc) [60, 64–66], and on the fibre post-treatment after the drawing [67]. POF made of PMMA is an anisotropic material because of its long molecules. However, the drawing process of the fibre causes molecules to become nearly aligned with the fibre axis and the material then is considered transverse isotropic [60]. Applying thermal treatment on POF, the stretched molecules relax and the mechanical properties of the material change. POF has much higher failure strain than its silica counterpart. The typical failure strain of SOF is reported to be 5-10% [68], whereas more than 100% strain has been reported for PMMA fibre [69], where the failure strain is affected by the drawing process of the POF. The PMMA yield point is reported to be approximately 6% where beyond that point the material stops having quasi-elastic behaviour and begins to deform plastically [60, 61]. However, the complex nature of the viscoelastic polymer material means that its tensile properties are not yet fully characterised. Researchers investigated the yield strain with respect to the rate of applied strain [60] and they made the conclusion that PMMA conforms better to the applied load at lower strain rates than at higher rates. However, hysteresis and creep effects are clearly visible at low strain values raising questions about how appropriate PMMA POF Bragg grating (POFBG) sensors are as strain sensors [15]. Hysteresis effect can be reduced by applying pre-tension or thermal annealing to POF [34, 70]. Another solution to that problem is to embed the POFBG sensor into the structure that needs to be monitored [71]. In this case, the POF will be forced by the structure back to its starting elasticity point when the strain value is zero, leading to a reduction of the hysteresis effect.

Degradation and aging of polymers is another challenge of POF technology, because the performance of the POFBG sensors can be different, due to the changes of the material properties over time [72]. The term ‘degradation’ usually describes the chain scission process where the chain bonds break to form oligomers and finally monomers. Consequently, the molecular changes can modify the properties of the material. Polymer ageing is referred to the process where the polymer is under degradation for extended period of time. There are different types of degradation in polymeric materials. It can be a chemical degradation, where there is a chemical reaction with the surroundings of the material [73]. This includes biodegradation and one example is the hydrolysis process, where the hydrolysable bonds break when the water is absorbed by the polymer [74]. A mechanical-degradation of polymers is also possible when the polymer is under high mechanical stresses [75]. A photo-degradation is referred to the influence of light absorption on the molecular structure of the material [76–78]. Finally, a thermal degradation is called the change of the

molecular structure due to the exposure of the material in relative high temperatures [79]. For temperatures above 150 °C, the PMMA material can be thermally degraded [80]. CYTOP is the most thermally stable material compare with the rest optical polymers [81]. The degradation factor in POFs is important, because the material structure can change, introducing different mechanical and optical properties to POF devices.

Optical Properties

The high optical attenuation of POF compared to SOF is one of the main drawbacks holding POF technology away from the market. The graph shown in Figure 2.1, which is similar with

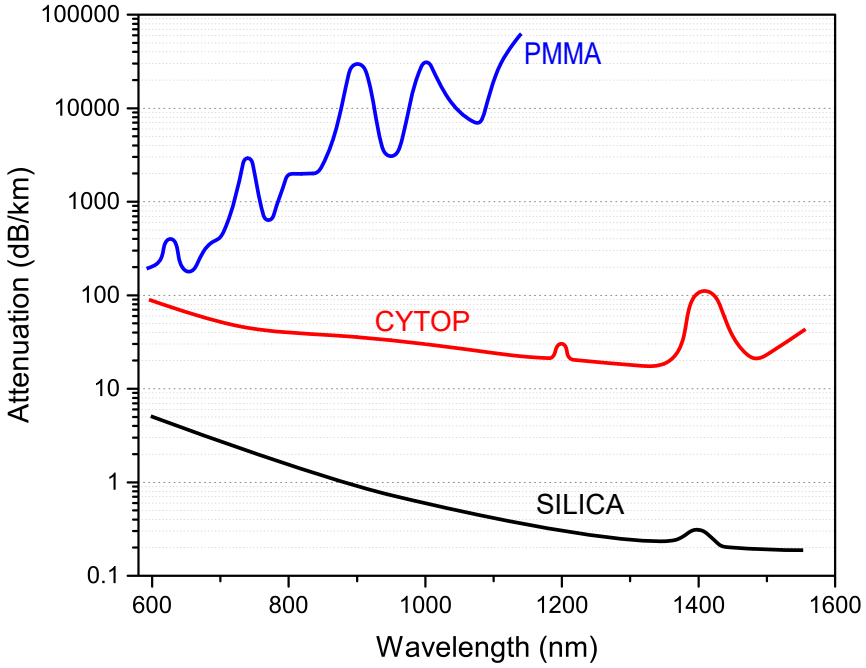

Figure 2.1: Attenuation of PMMA, CYTOP and silica.

the one reported in reference [31], shows the attenuation of PMMA, CYTOP and silica optical fibres. SOF usually has less than 0.2 dB/km loss at 1.55 μm spectral region. In contrast, PMMA POF has much higher loss - approximately 1 dB/cm in the 1.55 μm spectral region. Even though losses in gradient-index multi-mode PMMA optical fibres are less than 0.2 dB/m in the lower spectral region [82], they are still much higher than SOF. The main sources of absorption in POFs are vibrations and electronic transitions of molecular groups, which can vary depending on the material type. For example, carbon-hydrogen molecular groups have fundamental vibration absorption in 3.3-3.5 μm wavelength region, but the absorption harmonics extent up to visible wavelengths causing high optical attenuation in POFs [83]. By replacing the hydrogen atoms

with fluorine, chlorine, or bromine, the fundamental vibration absorption can be shifted to longer wavelength regions [84]. Therefore, the harmonics strength and the optical attenuation are reduced at shorter wavelengths regions, in which optical fibres are mostly operated. One of the examples is a gradient-index perfluorinated-POF [85], which has attenuation of 40 dB/km in the 0.8-1.2 μm wavelength range. This type of fibre is suggested also for local-area-network applications [31] due its low attenuation. Other researchers continued the work by demonstrating a perfluorinated polymer based graded-index POF with lower attenuation and material dispersion [86]. The material and optical properties of POF depend not only on the material type, but also on its history process; there are numerous reports showing that the fibre drawing conditions strongly influence the degree of birefringence in POFs [47, 87]. Optical properties can also change due to polymer degradation and other environmental disturbances. There is a report showing that exposing the POF in high temperature and humidity for extended period of time, the optical losses increase dramatically [88]. However, the same report shows that if the humidity is removed from the POF, the optical transmission returned to its initial condition.

2.1.3 Single-mode operation

Fabricating single-mode POFs is challenging. For single-mode operation of fibre is required that the normalised frequency is below the 2.405 value [89]. The normalised frequency depends on the refractive index difference between the core and cladding, and operational wavelength of optical fibre. Since the production of polymeric materials with very small refractive index difference is challenging, the step-index single-mode POFs are usually fabricated with small core sizes (3-6 μm) (see chapter 4) to satisfy the single-mode operation [90]. The small core sizes of POFs, leads to higher optical attenuation. In addition, connecting POFs with other types of POFs or SOFs becomes challenging, since the different core sizes increases the connection loss [71]. In the case of microstructured optical fibres, the effective refractive index of cladding depends on wavelength, while in step-index optical fibres it is almost constant [89]. The cladding structure in microstructured optical fibre is defined by the ratio of the hole diameter to the period of the lattice, which defines the normalised frequency. One characteristic of this type of fibre is that the normalised frequency tends to a constant value in shorter wavelengths. With a proper cladding design, the normalised frequency can be kept below the cut-off value and the fibre can be endlessly single-mode for any wavelength range [89]. For this reason, the single-mode POFs are preferred to be made as microstructured with higher core sizes. Another reason for choosing fabricating microstructured POFs is because it is much easier to drill holes in preforms compared with silica, or even 3D-print polymeric preforms for fibre drawing [91].

2.1.4 Handling and Connectorisation

POF needs a special handling treatment compared to SOF because of its ability to bend sharply without breaking, as a result the light transmission can be significantly reduced. In addition, cleaving single-mode POF the same way as SOF is not practical. Until recently it has been assumed that POF needs to be cut with a hot blade [92–94] on a hot plate. When POF and the cleaving blade are heated, the fibre material becomes ductile, and thus the fibre crazing is prevented. PMMA is reported to be ductile between 25 °C and 100 °C [94]. The authors concluded that the optimum cleaving conditions are: fibre temperature 70 °C to 80 °C, blade temperature 60 °C to 70 °C, and cutting speed 0.07 ms^{-1} to 0.5 ms^{-1}. The fibre should also be at least 90 seconds on the hot plate to equilibrate before cutting. There are also reports with different fibre and blade temperatures [92], which could indicate that each POF needs a different cleaving parameters, depending on its history process (material polymerisation process, fibre drawing conditions, and thermal history). It was recently demonstrated that fibre cleaving at room temperature is possible if the duration of the cleaving increases [95]. The authors cleaved the POFs with a sawing motion for a few seconds. The quality of the cleaving was similar with the more complicated heated systems. The POF can be also polished to create a smooth fibre end-face and solve problems associated with cracks or other defects [96]. Once the fibre is cleaved, the next step is to connect it to another single-mode POF or SOF. Connecting fibres or systems together is necessary for practical applications, but POF connectorisation technology is still at the first stages and more technological advancement is needed, such as commercially available automatic cleavers and splicers. The success of the connectorisation depends on the fibre core alignment, the gap distance between fibres, the quality of the fibre endfaces, and the degree of parallelism. The most common connectorisation method for single-mode POF is gluing two fibres together with the help of a UV lamp [97]. Recently, a new method of demountable connectorisation was demonstrated [98, 99], eliminating the difficulty of UV gluing and increasing the robustness of the connection. In the work presented in this thesis, a similar demountable connectorisation method is presented, but with lower connection loss.

2.1.5 Photosensitivity

Photosensitivity relates to the sensitivity of the polymer material to light. The intensity and the wavelength of the radiation exposure affect the photosensitive chemicals of the material and introduce chemical reactions. The main purpose of these chemical reactions is to introduce a change of the refractive index of the material and thereby change its optical properties. In the case of Bragg grating inscription, the refractive index changes periodically utilising the interference

pattern of two laser beams [2]. The first photosensitivity studies on polymer materials were done in 1970 by exposing a bulk PMMA material with 325 nm ultraviolet (UV) radiation [100]. A refractive index change of PMMA was observed by the authors, which required a few hundred hours after of UV radiation exposure for complete development [101]. In 1999, the first POFBGs inscribed in PMMA fibre were demonstrated by exposing the POF with laser wavelengths of 248 nm, and 325 nm transversely to the fibre [102]. It was shown that the 248 nm laser produced gratings by periodically ablating the surface of the fibre. This is mostly due to the large light absorption of the PMMA at this wavelength. The 325 nm laser produced a Bragg grating in the fibre core and since then this wavelength was the preferred option for the POFBG fabrication [103]. The authors reported that the induced refractive index change in the material is due to the photo-polymerisation of the 1% to 2% of non-reacted residual monomers. The photo-polymerisation as the main photo-inscription mechanism was confirmed later [104, 105], where monomers absorb energy from light (photons) and link with the macromolecule chains [106]. Even though, it was shown in 1993 that a refractive index change in PMMA bulk material is possible with a krypton fluoride (KrF) laser operating at 248 nm [107], scientists found it impossible to produce POFBGs with this laser due to fibre ablation issues.

Nowadays, the POFBG fabrication process usually requires tens of minutes [14]. However, the photo-inscription mechanisms are not yet fully understood and further inscription optimisation is possible. Investigations on photo-degradation of PMMA were also made at various wavelengths, where there was an observation of chain scission of the main polymer backbone [108, 109]. If the chromophores, which are the light-absorbing groups in polymers, absorb very high energy from photons, introduce backbone scission (split of chemical bonds), and consequently free radicals and monomers are produced [106]. In 2005, the photo-degradation mechanisms of PMMA were excessively studied under irradiation with a 248 nm wavelength light [110]. A crosslinking between the ester side chains of molecules was observed at low doses, which can densify the material and increase its refractive index. A photo-polymerisation was also observed at some degree at low irradiation dose. However, as the UV irradiation dose increases, large sections are detached from the molecular chain and eventually the whole molecule structure is gradually defragmented. The polymer chain scission in this case makes the material less dense and its refractive index lower [110].

In 2014, there was a further investigation of the main photosensitive mechanisms of PMMA POF at 325 nm wavelength [111]. It was found that increasing fibre strain during photo-inscription results in photosensitivity augmentation. This suggests that photo-degradation also takes place during the inscription process at 325 nm wavelength, because the stress can enhance photo-degradation [112]. In summary, the photo-polymerisation and photo-degradation

can be a competitive process. The photo-degradation rate depends on the intensity and wavelength of the light source [110]. In the case of PMMA material, the photo-degradation mechanism usually prevails at wavelengths below 250 nm. Changes on the molecular structure, such as photo-polymerisation and photo-crosslinking, mostly occur at longer wavelengths [113]. A thermal degradation of polymer (unzipping) is also possible at longer wavelengths. In general, the molecular structure of polymer can be altered either by photo-polymerisation (the residual monomers are polymerised), or by photo-crosslinking (molecules are linked together), or by photo-degradation (molecular bonds are split). All mechanisms possibly coexist under irradiation, but which one prevails is determined by the irradiation conditions, such as laser intensity, wavelength, pulse duration, fluence, and total time of exposure [110].

In 2015, the first POFBG fabrication using a KrF laser was demonstrated [33] and the authors showed that the photo-inscription is possible without damaging the fibre. The success of the authors relies on the low repetition rate of the pulsed laser and its low fluence [114, 115]. They produced POFBGs using a repetition rate of 1 Hz and fluence of 33 mJ/cm^2. The total inscription time was less than 30 seconds, which holds the record of the fastest inscription of POFBG until now. In this thesis, we demonstrate for the first time that a POFBG inscription is possible with only one KrF laser pulse. The pulse has duration of only 15 ns, which indicates the total exposure time required to fabricate a POFBG.

Therefore, the photosensitivity of the material depends on the chemical composition of the material (free radical and monomers, molecular weight distribution, branching degree, concentration of initiators, etc), the type of the laser source, and the irradiation conditions. Nevertheless, the photosensitivity of the material can be further enhanced by adding dopants or co-polymers into the fibre core. The first dopant added in POF is called p-benzoquinone and it was added to PMMA in order to enhance the photosensitivity of the material at 488 nm wavelength [116]. Fluorescein, which is a synthetic organic compound, has been also tried as a fibre dopant with great success [102]. Trans-4-stilbenemethanol was also used, which exhibits trans-cis photo-isomerisation when it is exposed to light with wavelength between 250 nm and 350 nm [55]. The isomerisation process occurs when one molecule changes its orientation. The reoriented molecule will have the same chemical formula, but different positioning of its atoms, which can modify the optical properties of the material, for example its refractive index. Therefore, when molecules develop isomerisation by irradiation (photo-isomerisation), they are called optical isomers because of their photosensitive nature [117]. The photo-initiator benzyl dimethyl ketal has been also used as dopant in POF with a great success [118, 119]. In this case, the photo-initiator triggers chemical reactions when the molecules are exposed to radiation. PMMA doped with benzyl dimethyl ketal was used in chapter 5 to inscribe a POFBG with only one laser pulse.

The aim of TRIPOD project, and for the scientific community in general, is to increase the photosensitivity of POFs in order to reduce the total photo-inscription time of POFBG sensors or any other optical device. That will reduce their production cost in industrial environments.

2.2 Bragg Gratings Inscribed in Polymer Optical Fibre

2.2.1 Historical Development

The first polymer Bragg grating was developed in a PMMA bulk material [120], but three decades passed before the first FBG in POF was produced in 1999 [102]. The authors used laser wavelengths of 248 nm and 325 nm to inscribe FBGs in PMMA optical fibres. The gratings produced with the 325 nm laser were inscribed in the fibre core. However, the high absorption coefficient of PMMA at 248 nm wavelength [121] caused an ablation on the fibre surface. The same research group continued the studies and demonstrated POFBGs in single-mode fibre with high reflectivity (28 dB transmission rejection) [122] and large tuning range (70 nm) [123]. Then, the first grating in microstructured POF was demonstrated [124]. The high attenuation of POF and the lack of high-quality connectorisation compared with the low loss SOF were the main reasons for POFBG technology to remain unused for several years. The total inscription time of POFBG sensors, which is several tens of minutes, also needs to be improved [14]. The 325 nm laser wavelength (or slightly longer wavelength) was the preferred option to produce gratings in POFs until today [103], due to ablation issues with shorter UV wavelengths. However, a refractive index modification in PMMA bulk material was demonstrated with a shorter UV wavelength back in 1993, when the authors used a laser fluence below the ablation threshold of the material [107]. The authors used a 248 nm pulsed krypton fluoride laser with energy density of 40 mJ/cm^2 and repetition rate of less than 5 Hz. In 2000, the refractive index of PMMA material was also modified when 193 nm and 248 nm lasers with energy densities of 15-25 mJ/cm^2 and repetition rate of 5 Hz were used for irradiation [110]. These examples show that inscribing a POFBG with a shorter than 325 nm wavelength could be possible, when a low laser fluence is used during irradiation. In 2015, the first POFBG with the 248 nm was produced in a POF [33]. The optical fibre was few-mode and microstructured made by pure PMMA. The authors used 33 mJ/cm^2 energy density and 1 Hz repetition rate to inscribe a POFBG in less than 30 seconds. Using shorter UV wavelengths for inscription may be the key to produce POFBG sensors effectively. The chapter 5 shows experimentally that fast POFBG inscription utilising a 248 nm laser system is feasible.

In general, the fabrication of a POFBG sensor has the same procedure as for silica based FBGs. POFBGs can be inscribed using the phase mask technique [125], or the ring interferometer arrangement [126]. In the latter reference, the authors investigated the temperature dependence

of a POFBG. However, the authors did not control the humidity during their experiments, which influences the behaviour of the sensor. The humidity influence was discovered afterwards [127], showing that the POF can absorb water and influence the Bragg grating structure. The Bragg wavelength shift due to humidity should be considered in the total shifting when the sensor is used to measure other quantities than humidity. As a solution to this issue, some researchers [128] developed a novel POF produced from a cyclic olefin copolymer (commercially known as TOPAS), which is humidity insensitive. Two years later it was found that TOPAS POF is actually 50 times less sensitive to humidity than PMMA optical fibre [129]. On the other hand, the ability of PMMA based sensors to absorb fluid can be useful when they are used as biochemical concentration sensors [130]. As it has been mentioned above, POFBGs can be highly efficient strain sensors because of the elastic properties of POF. Because of that, POFBG sensors can also have application in compliant structure monitoring. Non-linear behaviour of Bragg wavelength and fibre strain has been also studied [62]. POFBG sensors showed good performance for acoustic wave detection as well, because the low Young modulus of POF renders the sensors more sensitive to acoustic stress [131].

2.2.2 Types of Fibre Bragg Gratings and Applications

Uniform Bragg grating

The uniform FBG is a distributed Bragg reflector that is formed by sinusoidal modulation of the refractive index n along the fibre core axis z, as shown in Figure 2.2. This periodic structure can be imagined as a number of layers, where each one partially reflects back some of the incident light. The reflected waves that are in phase with each other create a constructive interference and the modes are coupled in the opposite direction (contradirectional coupling). The peak position of these wavelengths, which is called the Bragg wavelength, can be calculated by

$$\lambda_B = 2\, n\, \Lambda, \tag{2.1}$$

where λ_B is the Bragg wavelength, n is the effective refractive index of the guided mode and Λ is the period of the grating. A more detailed analysis is often required to obtain information about the characteristics of the reflected light. The most common approach is the coupled-wave theory [132], which gives an analytic solution of how the forward mode couples with the backward mode in the case of the Bragg grating. Using this theory, the reflectivity of a Bragg grating with constant amplitude of index modulation and grating length L_g is

$$R = \frac{\kappa^2\, sinh^2\, \psi\, L_g}{\Delta k^2\, sinh^2\, \psi\, L_g + \psi^2\, cosh^2\, \psi\, L_g}, \tag{2.2}$$

where $\Delta k = k - \pi/\lambda$ is the detuning wave vector which indicates the deviation from the Bragg

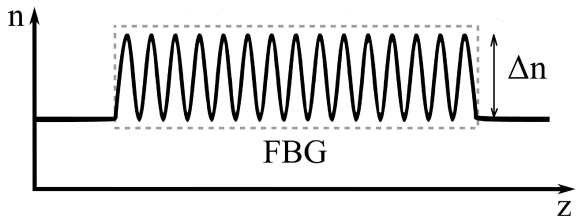

Figure 2.2: Uniform FBG - refractive index modulation along the fibre axis.

condition, $\psi = \sqrt{\kappa^2 - \Delta\kappa^2}$ is the off-Bragg vector and κ is the constant coupling coefficient given by

$$\kappa = \frac{\pi\, \Delta n\, \eta}{\lambda}, \tag{2.3}$$

where Δn is the amplitude of the index modulation, λ is the operated wavelength, and η is the grating efficiency representing how much of the guided light is overlapping the grating structure. Assuming the grating is fabricated only in the core of a step-index fibre, the grating efficiency is given by

$$\eta \approx 1 - \left(\frac{1}{n_1^2 - n_2^2}\right)\left(\frac{\lambda_0}{2\,\pi\, r}\right)^2, \tag{2.4}$$

where λ_0 is the free space wavelength, r is the radius of the fibre core, n_1 and n_2 are the core and cladding refractive indices respectively. If the incident light satisfies the Bragg condition, then $\Delta k = 0$ and the reflectivity simplifies to

$$R = tanh^2\left(\kappa\, L_g\right), \tag{2.5}$$

indicating that as the grating length L_g or the strength of refractive index modulation Δn is increasing, then the reflectivity of the grating increases towards unity. In the most of the cases, POFBG is not necessarily fabricated in the fibre core and the equation in (2.4) cannot be applied, especially in gratings fabricated in microstructured POFs. Equation (2.5) assumes the fiber is lossless, which is also not true in the case of POF. In chapter 3, the attenuation factor has been included in the coupled-mode equations, which are solved analytically to express the actual POFBG response. Besides the reflectivity factor of the grating, the bandwidth $\Delta\lambda$ of the grating has an important role as well and it is given by

$$\Delta\lambda = \lambda_B \left(\frac{2\,\eta\,\Delta n}{\pi}\right), \tag{2.6}$$

but this approximation does not apply to 'weak' gratings. The power reflection spectrum of a typical grating is depicted in Figure 2.3. The high reflectivity of the grating is an important factor for various applications. However, for sensing applications it is usually preferable to obtain weaker grating reflectivity (90%) in order to avoid the broadening (larger bandwidth) of the reflection peak. The reason is because the sharpness of the peak can increase the accuracy of the determination of the Bragg wavelength shift and improve the resolution of the sensor.

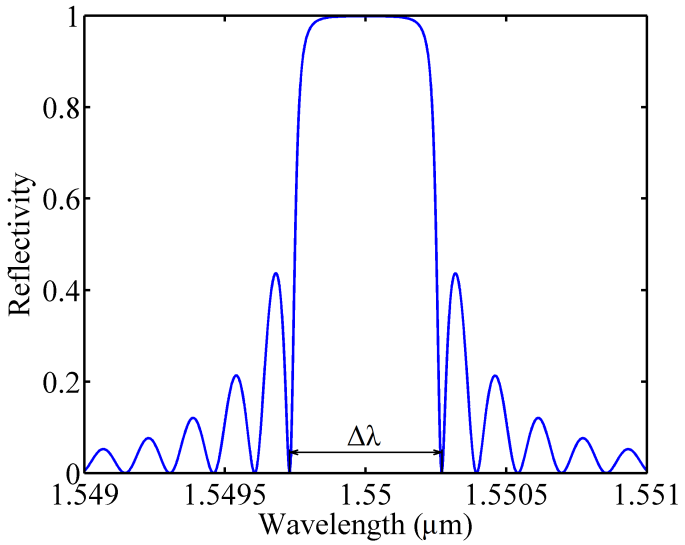

Figure 2.3: Uniform FBG of $\lambda_B = 1.55$ μm, $n = 1.45$, $\Delta n = 4 \times 10^{-4}$, and $L_g = 5$ mm.

Uniform POFBG sensors are usually used in applications to measure strain [133], force or stress [20], pressure [21], acoustic waves [22], temperature [24], and humidity [23]. The fibre strain is defined as the ratio of total deformation to the initial length of the fibre. The strain sensitivity can be expressed as the Bragg wavelength shift $\Delta\lambda_B$ due to the change of fibre strain $\Delta\varepsilon$:

$$\frac{\Delta\lambda_B}{\Delta\varepsilon} = \lambda_B (1-\rho), \tag{2.7}$$

where ρ is the effective photoelastic coefficient of the material and is equal to

$$\rho = \frac{n^2}{2}\left[P_{12} - \mu(P_{11} - P_{12})\right], \tag{2.8}$$

where P_{11} and P_{12} are the Pockels coefficients and μ is the Poisson's ratio of the fibre material. The Pockels coefficients represents the introduced refractive index change in the material due to fibre strain, and the Poisson ratio represents the transverse contraction of the fibre due to longitudinal extension strain. If the coefficients for PMMA and silica [19] are applied in the above equations, the given strain sensitivity of POFBG is only 14% higher than silica sensor [18]. This small difference is not enough to motivate the use of POFBG sensors as strain sensors, due to their other drawbacks. However, the much lower Young modulus of POF compared with SOF, renders the POFBG sensors much more sensitive to fibre stress, because the stress sensitivity equals the strain sensitivity divided by the Young modulus of the material. The temperature sensitivity can be defined as the Bragg wavelength shift $\Delta\lambda_B$ due to the change of temperature ΔT:

$$\frac{\Delta\lambda_B}{\Delta T} = \lambda_B (a + \xi), \tag{2.9}$$

where ξ is the thermo-optic coefficient and a is the thermal expansion coefficient of the material. For silica both coefficients are positive, the reason for the red shift of the Bragg wavelength. In

the case of POF, ξ is negative, and if its value is greater than a, then the Bragg wavelength blue shifts [134]. The humidity sensitivity, in the case of the hydrophilic POFs, can be described as the Bragg wavelength shift $\Delta\lambda_B$ due to the change of humidity ΔH:

$$\frac{\Delta\lambda_B}{\Delta H} = \lambda_B (n + \beta), \tag{2.10}$$

where β is the swelling coefficient which is related with the volumetric change due to humidity [135]. The refractive index n is normalised with the humidity.

Apodised Bragg grating

The most common FBG structure has a uniform index modulation, as it was described above, but there are other structures that offer different optical properties. The Bragg grating response is defined by the reflectivity, the bandwidth and the side-lobe strength. The grating length sets the peak reflectivity and the grating strength sets both the bandwidth and the peak reflectivity. The only way to control the side-lobe strength is to develop what is called an apodised Bragg grating with a refractive index profile approaching zero at the end of the grating structure. Typically, the Gaussian and raised-cosine refractive index profiles, as depicted in Figure 2.4 and Figure 2.5 respectively, can be used to suppress the side-lobes while maintaining the reflectivity and the narrow bandwidth.

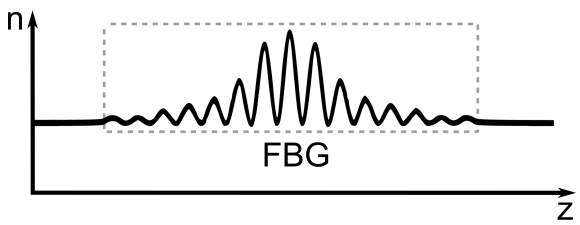

Figure 2.4: Apodised FBG with a Gaussian refractive index profile.

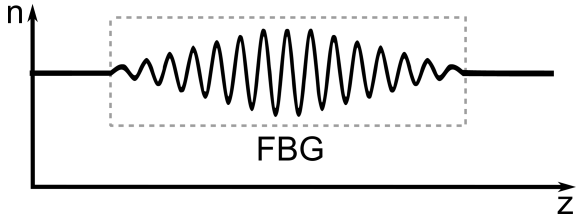

Figure 2.5: Apodised FBG with a raised-cosine refractive index profile.

Apodised Bragg gratings can find one of their applications in dense wavelength division multiplexing [136], because by suppressing the side lobes of the grating response, the cross talk between information channel is eliminated. In the case of an apodised grating, the refractive index

change is not constant and it can be described as

$$\Delta n(z) = \Delta n\, f(z), \tag{2.11}$$

where the $f(z)$ is the apodisation profile of the grating structure along its length z. For a uniform grating (no apodisation) $f(z) = 1$ and for Gaussian apodisation profile $f(z)$ becomes:

$$f(z) = exp\left\{-4\, log(2)\left[\frac{(z - L_g/2)}{s\, L_g}\right]^2\right\}, \tag{2.12}$$

where s is the taper parameter of the profile. Figure 2.6 shows the apodisation effect for different values of s.

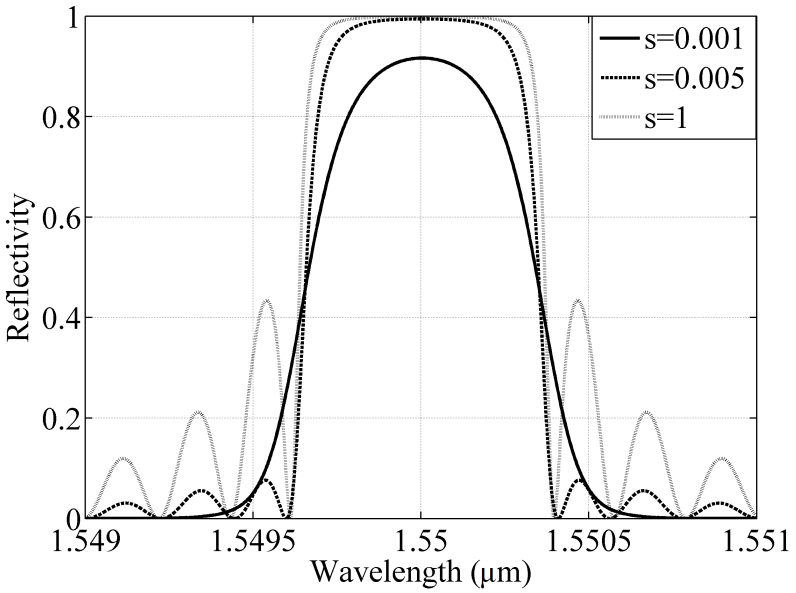

Figure 2.6: Apodised FBG of $\lambda_B = 1.55$ μm, $n = 1.45$, $\Delta n = 4 \times 10^{-4}$, and $L_g = 5$ mm with different tapering values.

Phase-shifted Bragg grating

Another type of grating structure is the π phase-shifted Bragg grating. It has the common periodic refractive index structure but usually one of the central 'mirrors' in the periodic structure is absent splitting the grating into two sub-gratings with a half-period phase difference. The refractive index profile along the grating in this case is shown in Figure 2.7. By locking a laser on the steepest part of the resonant peak, the π phase-shift FBG sensors can have higher sensitivity than the typical uniform FBGs. This π phase-shift in the refractive index periodicity introduces interference between the two sub-gratings and creates a resonant peak at the centre of the stop-band as depicted in Figure 2.8.

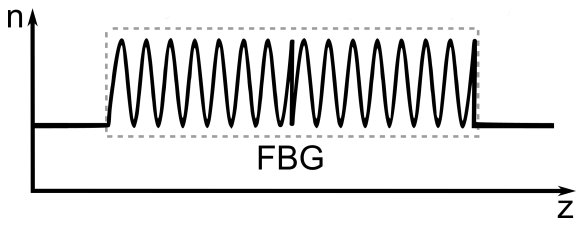

Figure 2.7: FBG with a π phase-shift refractive index profile.

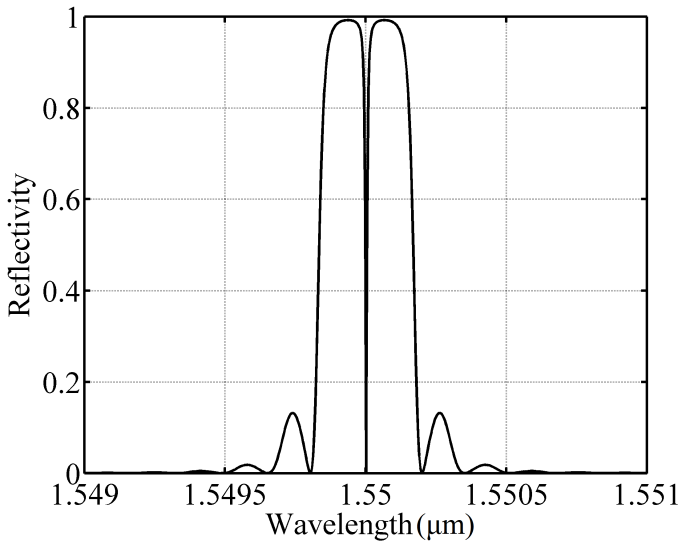

Figure 2.8: Reflection spectrum of a typical π phase-shift FBG.

Chirped Bragg grating

The chirped Bragg grating is another complex structure in which the periodicity and consequently the Bragg wavelength varies with the position along the grating structure, as shown in Figure 2.9. This aperiodic index modulation provides interesting properties such as reflectivity without side-lobes and a broad-band spectrum. One of the applications of chirped gratings is the possibility to achieve large group delay dispersion in a short length of fibre and compensate the dispersion occurring in a long transmission fibre in an optical communication system [137, 138].

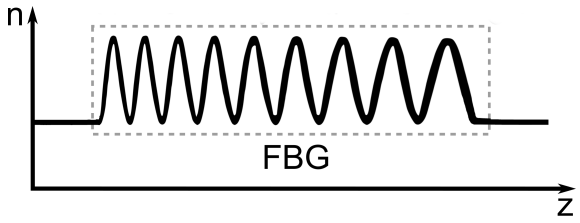

Figure 2.9: FBG with a chirped refractive index profile.

Long period Bragg grating

The first long period Bragg grating (LPG) in POF was reported in 2005 [139]. The LPG has the same periodic structure as the uniform grating but with a much larger period (few hundred

microns) than the operating wavelength [140]. This type of grating can be readily operated only in transmission, because this is codirectional and not contradirectional coupling. In this case, the guided modes are coupled into the copropagating cladding modes. The resonances from various cladding modes at these wavelengths appear as dips in the transmission spectrum. Long period Bragg gratings have various applications, such as band-rejection filters, gain flattering filters and sensors. Similar to long period gratings are the superstructure Bragg gratings that have a number of uniform Bragg gratings placed periodically in large distances along the fibre core. Each one acts like a single reflection layer and if they are placed to some distance from each other will have the same properties as the long period Bragg gratings.

The dips appeared in the transmission spectrum of the LPG depend on the period of the grating, the length of the LPG, the composition of the fibre, and the order of the cladding mode that is coupled to the cladding. By changing these parameters, the phase matching conditions for cladding coupling can change, and the attenuation bands in the transmission spectrum can shift. Therefore, LPGs can be used as sensors and they are normally used to detect strain, temperature, fibre bending, and refractive index changes in the external environment (including chemical concentration and humidity changes) [141]. Phase matching between the propagating core mode and cladding mode is achieved at the wavelength λ_m, when the expression

$$m\,\lambda_m = \Lambda\,(n_{co} - n_{clad}^m) \tag{2.13}$$

is satisfied, where m is a positive integer indicating the number of the cladding mode, n_{co} is the effective refractive index of the core more, and n_{clad}^m is the effective refractive index of the m^{th} cladding mode. The temperature sensitivity of a LPG sensor can be determined by:

$$\frac{d\lambda}{dT} = \frac{d\lambda}{d(\delta n_{eff})}\left(\frac{dn_{eff}}{dT} - \frac{dn_{clad}}{dT}\right) + \Lambda\frac{d\lambda}{d\Lambda}\frac{1}{L_g}\frac{dL_g}{dT}, \tag{2.14}$$

where T is the temperature, and $\Delta n = n_{eff} - n_{clad}$. The first on the right-hand side of equation (2.14) shows the contribution of the material composition, which is related to the differential refractive index changes of the core and cladding due to thermo-optic effect. Thus, altering the composition of the fibre, an enhanced sensitivity is possible. This term is also strongly related upon the order of the cladding mode. The material effect dominates in lower order cladding modes and it is negligible for higher order cladding modes. Note that cladding modes are determined by the LPG period Λ, as shown in equation (2.13). The second term shows the contribution of the waveguide design, which is determined by the LPG period. The sign and the magnitude of the second term also depend on the order of the cladding mode. Therefore, by an appropriate choice of grating period, the LPG sensor can have a positive or negative temperature

sensitivity, or it can be temperature insensitive. The strain sensitivity of a LPG sensor is given by:

$$\frac{d\lambda}{d\varepsilon} = \frac{d\lambda}{d(\delta n_{eff})}\left(\frac{dn_{eff}}{d\varepsilon} - \frac{dn_{clad}}{d\varepsilon}\right) + \Lambda\frac{d\lambda}{d\Lambda}, \tag{2.15}$$

where ε is the strain applied on the fibre. Similar with equation (2.14), the first term depends on the material composition and the second term on the waveguide design. With the appropriate choice of LPG period, the strain sensitivity can be positive, negative, or zero. The LPG sensors can also detect refractive index changes of the medium surrounding the fibre. The refractive index difference between the cladding and medium defines the effective index of the cladding mode. Consequently, the wavelength λ_m shifts as shown in equation (2.13). The LPG devices can be also used to sense fibre bending. In this case, the resonance occurred at the wavelength λ_m shifts or splits in two separate resonant dips. The splitting of the resonances is attributed to the asymmetry introduced in the system, as a result the cladding modes are not spatially degenerated. The wavelength shifting and the splitting depend on the orientation of the fibre bending with respect to the LPG planes. Considering the LPG characteristics above, the advantage of the LPG sensors compared with the uniform FBGs is the ability to use only one sensor for multi-parameter sensing. This can be achieved, by wisely choosing the fibre composition, the appropriate fibre designs and the LPG characteristics. LPG sensors independently measuring strain and temperature, or being insensitive to both is possible [142]. In general, the sensitivity of a LPG sensor can be altered analogous with the application needs.

Tilted Bragg grating

The first tilted Bragg grating in POF is reported in 2014 [143]. Tilted Bragg gratings have the typical periodical index variation in the axial direction but the grating boundary surfaces are not perpendicular to the light propagation but have a certain angle. This leads the guided-modes to be coupled to the counterpropagating core and cladding modes. The Bragg wavelength of the core mode λ_B and the resonance of the cladding mode λ_{clad} are determined by the phase-matching condition and can be expressed as

$$\lambda_B = \frac{2\,\Lambda\,n_{co}}{cos\vartheta}, \tag{2.16}$$

$$\lambda_{clad} = \frac{\Lambda(n_{co} + n_{clad})}{cos\vartheta}, \tag{2.17}$$

where n_{co} and n_{clad} are the effective refractive indices of the core and cladding respectively and ϑ is the tilted angle of the grating layers with respect to the light propagation. Tilted gratings have applications in communication systems where they can be used as add-drop filters [7], for modal power distribution measurement [144], as optical chemical sensors [145] and as refractometers [146] due to the ability of the cladding modes to be disturbed by the surrounding environment of the fibre.

2.2.3 Fabrication Techniques

The one-dimensional periodic variation of the refractive index along the optical fibre core can be achieved by creating an optical interference pattern using a specific laser source. If the material is photosensitive to the laser wavelength, the light from the interference fringes can be absorbed and a refractive index change can be introduced. One option to create the optical interference is by launching light into the core from both sides of the fibre and create a standing wave pattern [147]. The high intensity point fringes occurring from this pattern can change the refractive index of the material, generating the refractive index modulation along the core. However, the grating period is determined only by the laser wavelength and in the case of POF the absorption at the 325 nm (common laser inscription wavelength) is huge, resulting in this being an impractical way of POFBG inscription. Therefore, the FBGs are written externally by penetrating the interference pattern through the cladding into the core. One method is the holographic technique that uses the principle of amplitude splitting interferometry [2], as shown in Figure 2.10. In this case, the laser

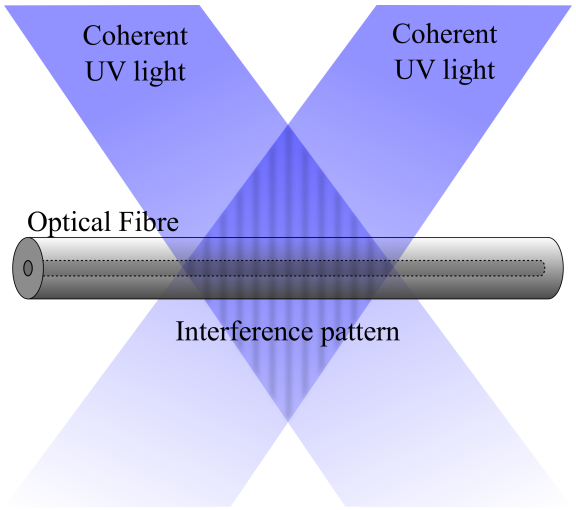

Figure 2.10: Fabrication with holography technique.

beam is divided into two identical ones with the same power, which are separated and recombined at some point producing an interference pattern. This pattern is focused to the fibre core and the grating is formed. The period of the photo-inscribed grating structure is given by

$$\Lambda = \frac{\lambda_{UV}}{2\ sin\theta}, \tag{2.18}$$

where the λ_{UV} is the operating wavelength of the UV laser and θ is the angle between the two divided beams. The advantage of this method is the ability to control the angle between the two interfering beams, providing the flexibility to produce a Bragg grating structure with the desired period. However, vibrations or any other disturbances (e.g. air flow) to the optical components (mirrors, beam splitter, etc.) and the slight deviations of the laser beams from their optical path,

could result in the deformation of the interference pattern, affecting the refractive index modulation and consequently reducing the quality of the Bragg grating response. This fabrication method was used in the work described in chapter 8 to inscribe volume Bragg grating devices. The reasons for choosing this method are discussed in chapter 8.

Wavefront splitting interferometric techniques are more stable approaches because fewer optical components are required to produce the interference pattern. An example is the Lloyd's mirror interferometer. The laser beam comes to a dielectric mirror with some angle and part of the wavefront light is reflected back interfering with the other part that follows the initial optical path, as shown Figure 2.11. This method is still not widely used because of some drawbacks. The FBG length is limited to the half width of the UV laser beam, the grating period is limited by the system geometry and the laser beam should have high spatial coherence because the interference occurs between different parts of the beam.

The most widely used fabrication technique is the usage of a phase mask. The reason is because this method is relatively simple and reliable to produce FBGs. The phase mask technique was first demonstrated in 1993 [148]. The phase mask, which has a periodic structure, is a diffractive element that splits the incident beam to some diffraction orders. Typically, a phase mask is designed for a specific inscription wavelength in order to split the incident laser beam to only two diffraction orders (usually the ± 1 orders). The two beams create an interference pattern the same way as the other techniques and if the fibre is placed in the interference region, the grating structure can be formed, as shown in Figure 2.12. The other diffraction orders, besides the two main ones, are required to be suppressed in order to prevent any other interference because it will negatively affect the quality of the grating structure [149]. The phase mask is placed parallel and very close to the fibre providing good photo-inscription stability.

The interference pattern produced from the phase mask creates a Bragg grating with period half of the phase mask period. The Bragg wavelength λ_B can be calculated by

$$\lambda_B = n_{eff}\, \Lambda_{PM}, \tag{2.19}$$

where Λ_{PM} is the period of the phase mask structure which is doubled than the grating period. The phase mask technique can be used to fabricate either uniform or tilted Bragg gratings by just placing the mask at the desired angle with respect to the fibre axis [150]. The disadvantage of this technique is that there is no flexibility to fabricate any desired Bragg wavelength structure because the grating period depends exclusively on the period of the phase mask. The physical dimensions of the phase mask should be carefully designed, in order to obtain exactly the Bragg wavelength that the producer desires. However, by applying axial strain to the POF when it is placed for photo-inscription [151] or annealing it after the recording to shrink the fibre, the Bragg wavelength

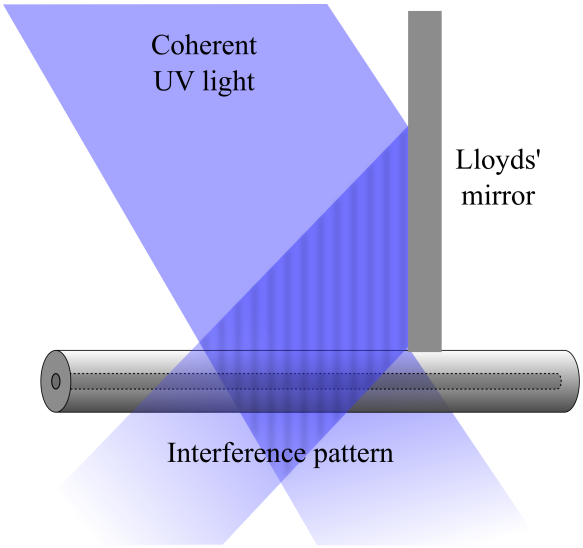

Figure 2.11: Fabrication with Lloyd's mirror technique.

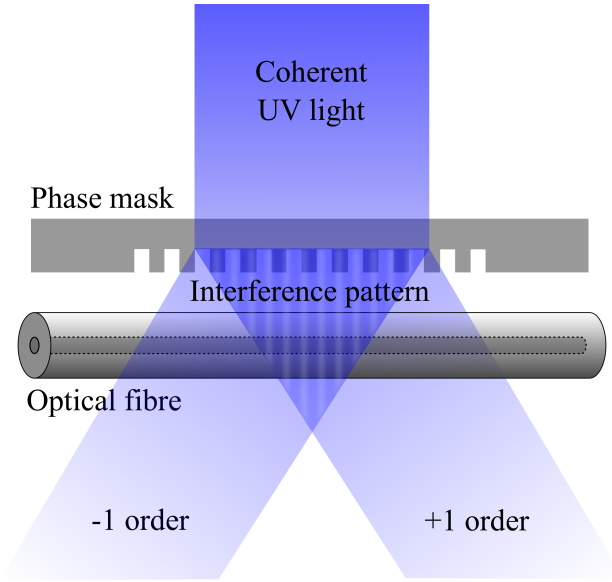

Figure 2.12: Fabrication with phase mask technique.

can be permanently tuned to a shorter wavelength position. The phase-mask inscription method was used in the work described in chapters 4-6.

The refractive index modulation can be also done by the point-by-point inscription method, which is a quite different one [152]. In this method, the Bragg grating structures are not fabricated by creating an interference pattern like the other techniques, but a high-power femtosecond laser beam is tightly focused to the fibre core and directly modifies the material. The ultra-short (femtosecond) intense pulses with low repetition rate can rapidly transfer energy above the threshold of the material and change its refractive index, without creating any thermal diffusion [153]. These femtosecond pulses create a nonlinear process such as multi-photon absorption and the refractive index of a material can be directly modified. This is an advantage because the material does not have to be necessary photosensitive to the inscription

wavelength [154]. Besides the point-by-point method, there is also a line-by-line [155] and plane-by-plane method [156]. The advantage of these methods is the ability to fabricate any grating structure and period. There is a flexibility to fabricate not only uniform, chirped or tilted Bragg gratings, but also more complex structures such as superstructure Bragg gratings [157], or any other complex 2D [158] and 3D [159] structures, where with the other techniques it seems impossible. The main challenge of the femtosecond laser systems is to align precisely the fibre core with the tiny focused laser beam. Thus, the precise positioning of the laser beam with this method requires using a high-precision air-bearing stage. Moreover, vibrations to the inscription system or temperature changes in the environment can negatively affect the quality of the grating structure.

3 Modelling of Bragg Gratings and Fabry-Pérot Sensors

This chapter investigates the attenuation effects on Bragg gratings and Fabry-Pérot devices used for stress sensing. The rationale of this work is the fabrication of Bragg grating based Fabry-Pérot sensors and their distribution to TRIPOD consortium for ultrasonic wave detection tests. These sensors can be great candidates in the future in endoscopic biomedical applications.

3.1 Introduction

As described previously, fibre Bragg grating (FBG) sensors can have various applications involving the monitoring of strain, stress, temperature, humidity, acoustic waves, specific chemical concentrations, etc. Interferometric sensors can be used in applications where higher sensitivity levels are required. One example showing extreme levels of sensitivity is the recent observation of gravitational waves, where a modified Michelson laser interferometer with 4 km long arms was used [160]. In the case of optical fibre-based interferometric sensors, geophone [161] and hydrophone [162] applications have been reported. In the absence of loss, the sensitivity of the Fabry-Pérot (FP) interferometric sensor is proportional to its cavity length. However, practically this is not the case, especially when interferometers are constructed from polymer optical fibre (POF). By increasing the cavity length of the interferometer, sensitivity reduction can occur at

some point due to the attenuation along the optical path. In other words, there is an optimum cavity length where the interferometer can have maximum sensitivity. The loss leads to a reduction in the signal level obtained from two-beam interferometers, while in the case of FP interferometers the finesse can be also significantly reduced. Therefore, there is a need to investigate the attenuation effects on the interferometric sensitivity and find the right conditions to optimise the performance of a POF based interferometric sensor.

In this chapter, a system model has been developed in MATLAB to investigate the effects of the optical attenuation on the performance of FBGs and Bragg grating based FP stress sensors [163]. The reason for studying stress rather than strain sensors is because the given strain sensitivity of POF sensors is only 14% higher than silica optical fibre (SOF) sensors [18] and this small difference is not sufficient to motivate the use of POF devices as strain sensors, due to their other drawbacks. However, the much lower Young modulus of POF compared with SOF, renders the POF sensors much more sensitive to stress or equivalently more sensitive to force acting on the fibre. For example, POF sensors can be used to monitor the deformation of a pressure sensitive highly compliant diaphragm [21] or they can be used to detect the pressure waves of acoustic signals [22]. In the case of acoustic wave detection, interferometric sensors are preferred, since long interferometric cavity lengths will provide enhanced sensitivity. In addition, the temperature cross-sensitivity would not be an issue, given that the temperature shifts and the phase modulation induced by acoustic waves do not lie in same frequency ranges.

In the system model presented in this chapter, three different fibre materials have been investigated: poly(methyl methacrylate) (PMMA), cyclic transparent optical polymer (CYTOP), and fused silica. The FP interferometric devices have been characterised in three different spectral regions (650 nm, 850 nm, and 1550 nm), where commercially components and detectors are readily available. Note that each fibre material operating in specific wavelength region has different optical attenuation. The material properties, such as Young modulus, Pockels coefficients, and Poisson ratio have been also used to calculate the stress sensitivity of the FP interferometer. The dependence of Pockels coefficients on wavelength is considered to have negligible impact in the results presented in this chapter. Young modulus is the major factor influencing the stress sensitivity of the FP devices. The common arrangement of a FP cavity is a pair of partially reflective, optical flat and parallel mirrors placed at some distance. The input light is reflected multiple times between the mirrors and constructive interference occurs when the transmitted beams are in phase. FP interferometers can be used for stress sensing by monitoring the sharpest slope region of these resonant peaks, which shifts in wavelength when stress is applied to the fibre axis and the cavity length is changed. One practical method to fabricate partially reflective mirrors into the optical fibre is to photo-inscribe two FBGs some

distance apart, which act as mirrors. The physical length and the refractive index change in the periodic structure of each Bragg grating, specify the reflection and transmission coefficients of the FP interferometric mirrors. These coefficients can be also affected by the fibre loss when Bragg gratings are fabricated in POF. Therefore, the coupled-mode equations have been modified in order to include the loss factor along the physical length of the grating structure. The Bragg grating effective length is also an important parameter to consider; when the light is propagating in the fibre, it can penetrate the Bragg grating structure at some depth before it is effectively reflected back. The effective penetration depth or simply the effective length of the propagating light depends on the characteristics of the grating structure and it should be taken into account in order to assess the actual cavity length of the interferometer. The system model presented in this chapter can be used to evaluate the performance of the FP stress sensor and identify which fibre material can offer the highest sensitivity when the physical dimensions of the device have been already decided.

3.2 System Model

3.2.1 Reflection and transmission coefficients of Bragg grating

The Bragg grating is a periodic structure and it can act as a reflection hologram as depicted in Figure 3.1. In this case, a contra-directional mode-coupling occurs between the reference R and the signal S amplitude waves, as the light propagates along the grating axis z. The coupling between S and R waves can be expressed analytically by using the coupled-mode equations [164–166]. Considering the loss along the grating structure, the attenuation term has been added in the coupled-mode equations:

$$\frac{dR}{dz} = -j\,\kappa^{*}\,S\,e^{j\psi z} - \frac{\alpha}{2}\,R, \tag{3.1}$$

$$\frac{dS}{dz} = j\,\kappa\,R\,e^{-j\psi z} + \frac{\alpha}{2}\,R, \tag{3.2}$$

where α is the intensity attenuation, and ψ is the off-Bragg vector which can be expressed as

$$\psi = 4\,n\,\pi\,\left(\frac{1}{\lambda} - \frac{1}{\lambda_B}\right), \tag{3.3}$$

where λ_B is the Bragg wavelength, λ is the free-space wavelength of the input light, and n is the refractive index. The term κ is the coupling coefficient between the modes which is equal to

$$\kappa = \frac{\pi\,\Delta n}{\lambda_B}, \tag{3.4}$$

where Δn is the refractive index change in the medium to form the periodicity of the Bragg grating. In this model, the Bragg grating structure is uniform and the parameters Δn and λ_B are considered

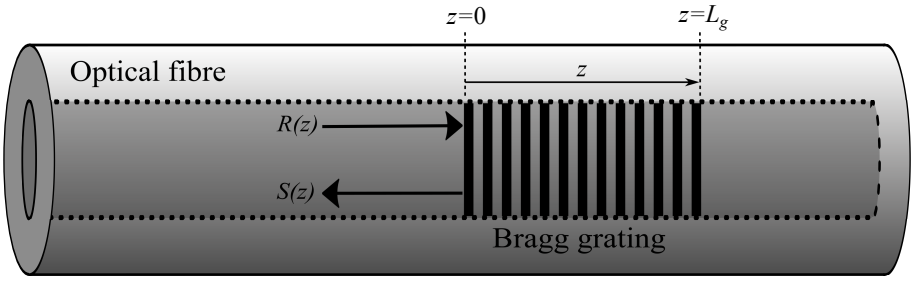

Figure 3.1: Fiber Bragg grating structure.

constants. The diffraction efficiency η at any point across the grating axis z is

$$\eta(z) = \frac{S(z)}{R(z)}. \tag{3.5}$$

By differentiating equation (3.5) becomes

$$\frac{d\eta}{dz} = \frac{1}{R}\frac{dS}{dz} - \frac{S}{R^2}\frac{dR}{dz}, \tag{3.6}$$

Substituting equations (3.1) and (3.2) to equation (3.6) leads to

$$\frac{d\eta}{dz} = j\,\kappa\, e^{-j\psi z} + \alpha\,\eta + j\,\kappa^*\, e^{j\psi z}\,\eta^2, \tag{3.7}$$

which is a non-linear Riccati equation (first-order, ordinary differential equation). The diffraction efficiency η can be calculated by knowing the boundary conditions. In most applications, only one wave is incident to the FBG and there is no signal wave at the other end of the grating. Considering that the reference wave R is incident on the near end of the grating ($z = 0$) with unity amplitude, and the signal wave at the far end ($z = L_g$) is zero, the boundary conditions become

$$R(0) = 1, \quad S(L_g) = 0, \tag{3.8}$$

where L_g is the total grating length as depicted in Figure 3.1. Equation (3.7) can now be solved numerically to obtain the diffraction efficiency at the near end of the grating ($z = 0$). The reflection coefficient of the FBG equals:

$$r = \eta\,\eta^*. \tag{3.9}$$

The amplitude of the FBG transmission coefficient equals the amplitude of the transmission wave R at the far end of the grating ($z = L_g$). Therefore, using equations (3.1) and (3.2) to eliminate the signal wave S, the transmission wave R is given by

$$\frac{dR^2}{dz^2} = R\left(\kappa^2 + \frac{\alpha^2}{4}\right), \tag{3.10}$$

with boundary conditions:

$$R(0) = 1, \quad \frac{dR}{dz}\Big|_{z=L_g} = -\frac{\alpha}{2}\,R\,(L_g). \tag{3.11}$$

The power transmission coefficient of the FBG is

$$t = R\,R^*. \tag{3.12}$$

3.2.2 Effective Length of Bragg Grating

The effective length L_{eff} of each FBG shows the penetration depth of the propagating light in the grating structure before it is effectively reflected back. This is important to calculate the total cavity length L of the interferometer which is

$$L = L_{eff_1} + L_d + L_{eff_2}, \tag{3.13}$$

where L_{eff_1} and L_{eff_2}, are the effective lengths for the FBG_1 and FBG_2 respectively as depicted in Figure 3.2. The term L_d is the distance between the cavity ends of the two FBGs. When the reflection coefficient of the grating is small, the propagating light can be considered to be reflected from the middle of the FBG [167]; i.e. the effective length equals the half of the total FBG physical length. As the reflectivity of the grating increases, the effective length becomes shorter because a greater proportion of the light is reflected from the first optical planes of the grating. The effective length corresponds to the group length of light [167]:

$$L_{eff} = \frac{v_g \, \tau}{2}, \tag{3.14}$$

where $v_g = c/n_g$ is the group velocity, n_g is the group refractive index and it is assumed equal to n, c is the free-space velocity, and τ is the group delay of the light reflected by the grating which can be expressed as

$$\tau = -\frac{\lambda^2}{2\,\pi\,c}\,\frac{d\varphi}{d\lambda}, \tag{3.15}$$

where φ is the phase of the reflection coefficient.

3.2.3 Structure of Fabry-Pérot Interferometer

The FP interferometric cavity can be formed by two uniform gratings as shown in Figure 3.2. The electric field on each interface boundary as depicted in Figure 3.2 can be described as

$$E_1 = E_0 \sqrt{t_1} + E_4 \sqrt{r_1}, \tag{3.16}$$

$$E_2 = E_1 \, e^{jkL} \, e^{-\frac{a}{2}L}, \tag{3.17}$$

$$E_3 = E_2 \sqrt{r_2}, \tag{3.18}$$

$$E_4 = E_3 \, e^{jkL} \, e^{-\frac{a}{2}L}, \tag{3.19}$$

$$E_t = E_2 \sqrt{t_2}, \tag{3.20}$$

where $t_{1,2}$ and $r_{1,2}$ are the transmission and reflection coefficients respectively for the corresponding FBG, α is the attenuation along the interferometric cavity L, and k is the wavenumber which is equal to

$$k = \frac{2\,\pi\,n}{\lambda}. \tag{3.21}$$

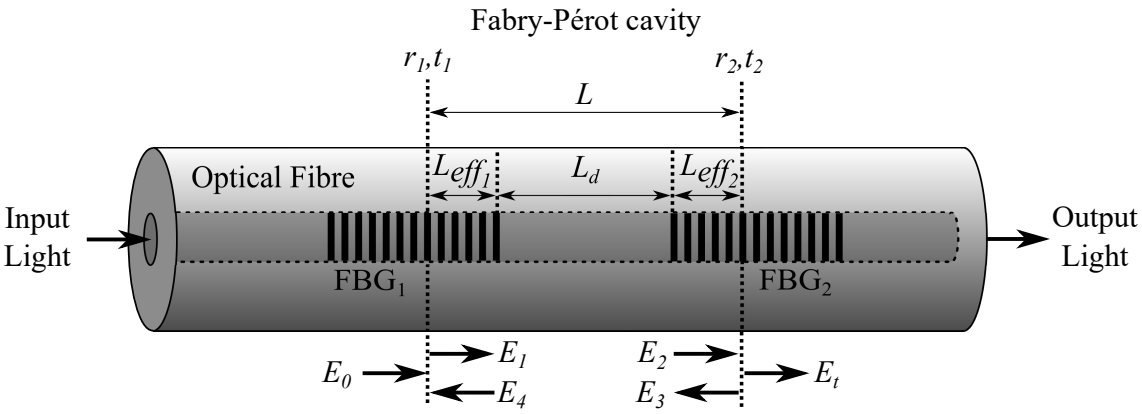

Figure 3.2: FP cavity formed by two uniform FBGs.

Combining equations (3.16)-(3.20), the transmitted electric field E_t can be calculated as

$$E_t = \frac{E_0 \sqrt{t_1}\ \sqrt{t_2}\ e^{jkL}\ e^{-0.5\alpha L}}{1 - \sqrt{r_1}\ \sqrt{r_2}\ e^{2jkL}\ e^{-\alpha L}} \tag{3.22}$$

Considering a unity input of electric field ($E_0 = 1$), the intensity in transmission ($I_t = E_t\ E_t^*$) becomes

$$I_t = \frac{t_1\ t_2\ e^{-\alpha L}}{1 - \left(2\ cos\left(2\ k\ L\right)\ \sqrt{r_1}\ \sqrt{r_2}\ e^{-\alpha L}\right) + r_1\ r_2\ e^{-2\alpha L}}. \tag{3.23}$$

If the operating wavelength or the cavity length is appropriately tuned, the transmitted beams of the interferometer are in phase and constructive interference occurs; i.e. the intensity exhibits narrow peaks in the transmission spectrum corresponding to FP interferometric resonances. The sharpness of these resonant peaks increase analogously with the cavity length or the reflectivity of the mirrors. As an illustration, Figure 3.3 depicts the sharpness difference between the transmitted peaks with 60% and 80% reflectivity mirrors. When stress – or equivalently force – is applied to the device, the interferometric cavity changes in length and these resonant peaks shift in wavelength. In this case, the FP interferometers can be used as stress sensors if the steepest part of the slope region of these resonant peaks can be monitored. Figure 3.4 shows the sensitivity – the slope of the transfer function – of a FP when it is formed with 60% or 80% reflectivity mirrors. This illustration shows that the maximum sensitivity of the FP sensor is analogous with the mirrors' reflectivity of the interferometer. In the model presented in this chapter, it is assumed that a monochromatic light source is tuned to the steepest part of the transmitted peaks of the interferometer and in the following text always the maximum sensitivity of each resonant peak is presented.

As an illustration, Figure 3.5 shows the reflected power from a FP device, in which the tunable laser can be locked at the point 1 of the spectral position. The blue solid-line represent the reflection spectrum without any stress applied on the fibre. A small degree of fibre stress will shift the Bragg wavelength to longer wavelengths (red dot-line). In that case, the reflected power

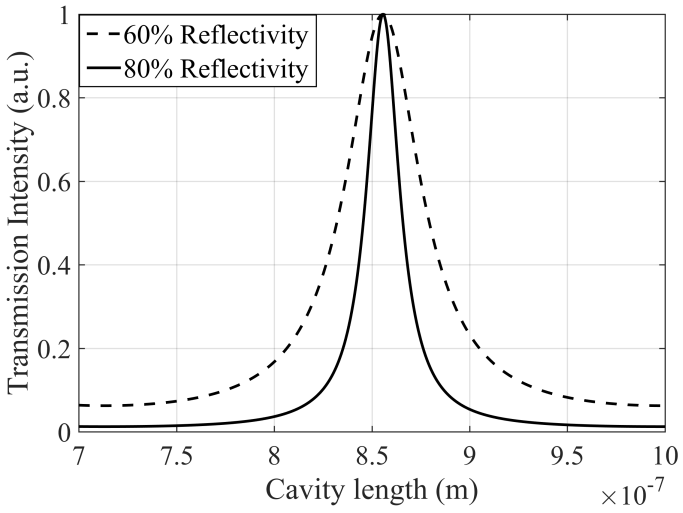

Figure 3.3: Transmission intensity of a FP with 60% or 80% reflectivity mirrors.

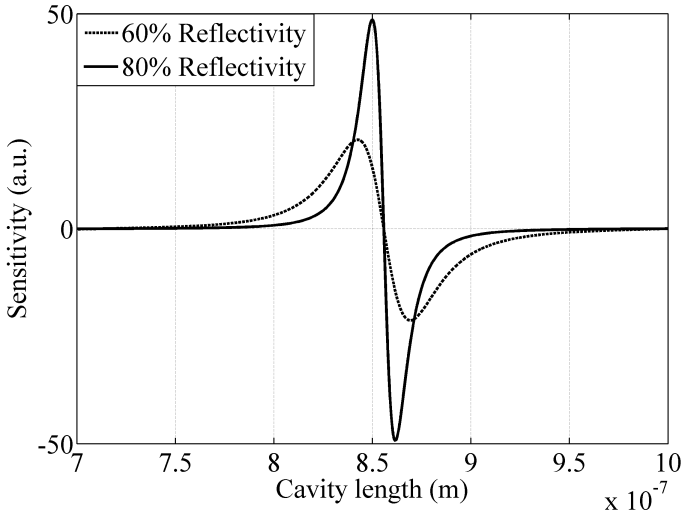

Figure 3.4: Sensitivity of a FP with 60% or 80% mirrors reflectivity.

from the FP device will be much less because the laser (at a fix wavelength position) will be in a different position at the resonant peak (see point 2). Therefore, detecting intensity changes (e.g. using a photodetector) the fibre stress can be assessed.

3.2.4 Modelling Methodology

Equation (3.7) can be solved numerically in MATLAB using the ODE-45 function in order to calculate the reflection r and transmission t coefficients for each grating. It is assumed that the interferometer is always operating at the Bragg wavelength, and then the maximum FBG reflectivity is used to describe the reflection coefficient of the interferometric mirror. The strain

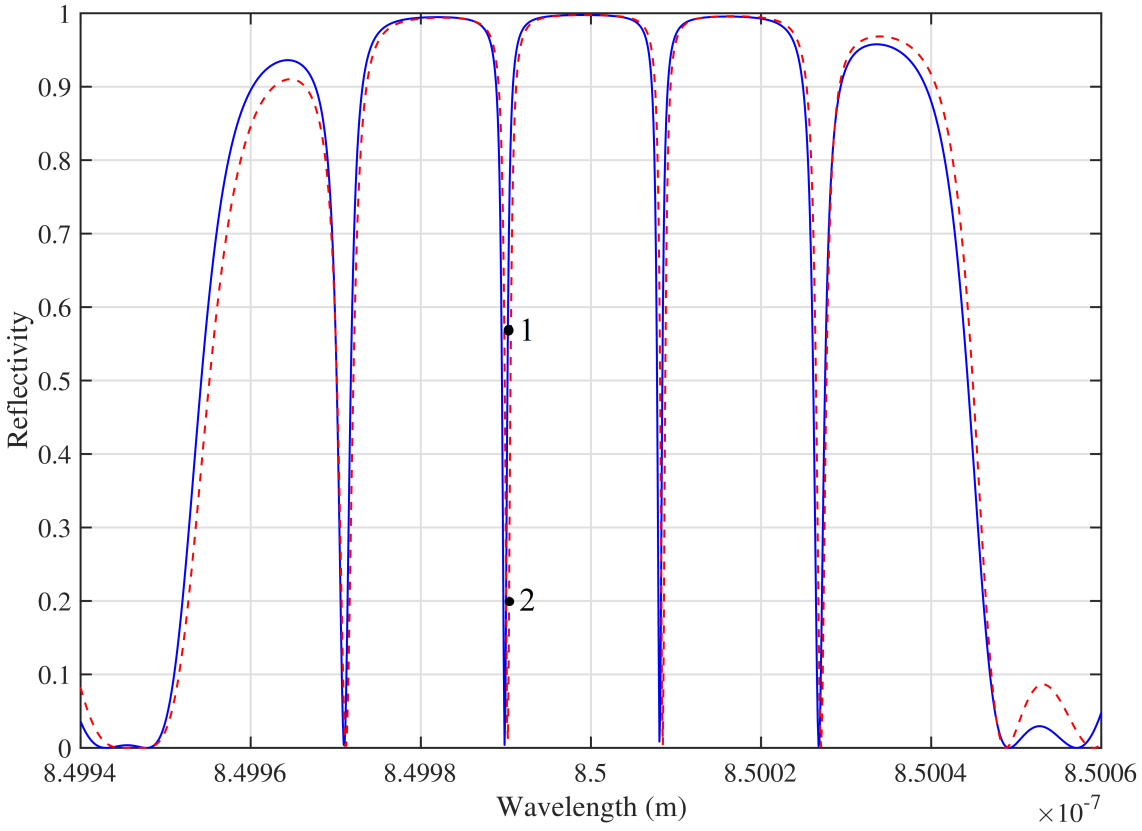

Figure 3.5: FP reflected power explaining the operation principle of a stress sensor.

sensitivity of FP sensor can be calculated by differentiating (3.23) with respect to strain:

$$\frac{dI_t}{d\varepsilon} = \frac{\partial I_t}{\partial n}\frac{\partial n}{\partial \varepsilon} + \frac{\partial I_t}{\partial L}\frac{\partial L}{\partial \varepsilon}, \tag{3.24}$$

where $\partial L/\partial\varepsilon$ is equal to the cavity length L, and the terms $\partial I_t/\partial n$ and $\partial I_t/\partial L$ can be calculated by differentiating equation (3.23) with respect to n and L, respectively. If a homogeneous and isotropic elastic material is assumed [168], the refractive index change due to strain is

$$\frac{\partial n}{\partial \varepsilon} = \frac{n^3\ (\mu\, P_{11} + (\mu - 1)\, P_{12})}{2}, \tag{3.25}$$

where P_{11} and P_{12} are the Pockels coefficients and μ is the Poisson's ratio of the fibre material. The stress sensitivity of the FP sensor can be expressed as

$$\frac{dI_t}{d\sigma} = \frac{1}{Y}\frac{dI_t}{d\varepsilon}, \tag{3.26}$$

where Y is the Young modulus of the fibre material defined as

$$Y = \frac{\sigma}{\varepsilon}, \tag{3.27}$$

where ε is the strain and σ is the stress of the material under stress. The relevant optical and material properties of PMMA, CYTOP, and fused silica based fibres are listed in

Table 3.1 [18, 19, 31, 49, 169–173]. Due to the fact that Pockels coefficients of CYTOP material are not yet known, the PMMA Pockels coefficients are used as an alternative solution. These coefficients have been changed more than 50% in value during the characterisation of CYTOP based FP sensor, indicating negligible impact on its overall stress sensitivity. We should also mention that as yet there are no examples of single-mode CYTOP fibre available, however may be available in the near future. The model system presented in this thesis is quite generic and it can be used for any type of optical fiber and attenuation values. The values used for simulation are of course not absolute; they are used only as examples to show the effects of attenuation on the sensitivity of the sensor. This model can be implemented by researchers accordingly with their needs. It is not even necessary to have optical fibre; any one-dimensional optical medium with a known mechanical and optical properties and a single-mode operation is sufficient for the simulation. The model can be also used in the asymmetry case using the equation (3.23). However, the aim in this work is to show mostly the effects of attenuation (when the interferometer is operated at different wavelength or different optical medium). It is out of scope of this work to introduce asymmetry in the system, to avoid unnecessary confusion and complicated cases. However, if this scenario or any other possible combination of refractive index change, grating length, attenuation, operational wavelength, cavity length, or even different optical medium should be explored, then it is easily implemented in MATLAB by using the presented model system.

3.3 Results and Discussion

The reflection and transmission coefficients will be decreased in value when the Bragg grating is fabricated in a fibre with high loss. Figures 3.6, 3.7, and 3.8 illustrate how the FBG reflectivity can be reduced when the attenuation is 1 dB/cm which is the case for PMMA fibre operating at $\lambda = 1550$ nm. Figure 3.6 shows the reflection spectrum of a grating with physical length $L_g = 4$ mm and refractive index $\Delta n = 10^{-4}$, without loss (dashed line) and with attenuation of 1 dB/cm (solid line). Figure 3.7 shows the reflectivity of a longer grating ($L_g = 20$ mm), but with the same refractive index change ($\Delta n = 10^{-4}$). In this case, the reflectivity is higher than the reflectivity shown in Figure 3.6, because the longer physical length of FBG means more grating periods; i.e. more light is reflected back from the grating structure. On the other hand, it also means that the reflection coefficient is affected to a higher degree by the fibre loss. Figure 3.8 depicts the reflection spectrum of a grating with $L_g = 4$ mm and $\Delta n = 5 \times 10^{-4}$. In this case, by increasing the refractive index change, instead of the grating length, the impact of the fibre loss on the reflection coefficient is less, but the bandwidth of the grating is larger, which may not be desirable for applications where the Bragg wavelength peak position is used as a reference

Table 3.1: Material properties of PMMA, CYTOP, and fused silica.

Symbol	PMMA	CYTOP	Fused Silica
Y	2.8 GPa	6.5 GPa	73 GPa
P_{11}	0.300	0.300	0.113
P_{12}	0.297	0.297	0.252
μ	0.345	0.420	0.170
n_1	1.47	1.33	1.44
n_2	1.48	1.34	1.45
n_3	1.49	1.34	1.46
α_1	100000 dB/km	20 dB/km	0.2 dB/km
α_2	2000 dB/km	40 dB/km	1 dB/km
α_3	200 dB/km	70 dB/km	4 dB/km

n_1: Refractive index at $\lambda = 1550$ *nm* α_1: Attenuation at $\lambda = 1550$ *nm*

n_2: Refractive index at $\lambda = 850$ *nm* α_2: Attenuation at $\lambda = 850$ *nm*

n_3: Refractive index at $\lambda = 650$ *nm* α_3: Attenuation at $\lambda = 650$ *nm*

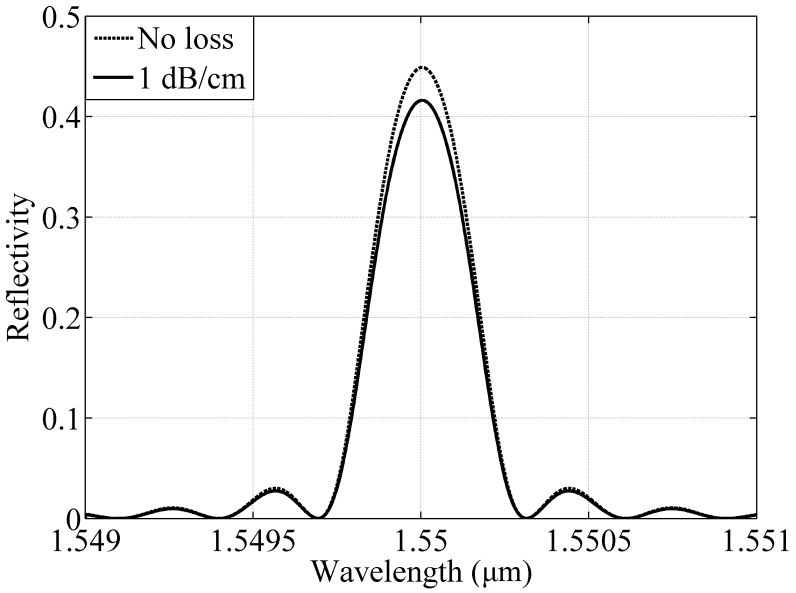

Figure 3.6: Reflectivity of FBG with $L_g = 4$ mm and $\Delta n = 10^{-4}$.

point for sensing. However, by using FBGs as interferometric mirrors, their large bandwidth could be practically helpful. For example, there are cases where obtaining exactly the same Bragg wavelength response from both FBGs is practically difficult and this results in situations where the interference between the two grating reflected beams is reduced. The large bandwidths of the two FBGs will provide higher tolerance to their mismatched Bragg wavelengths. Another benefit is

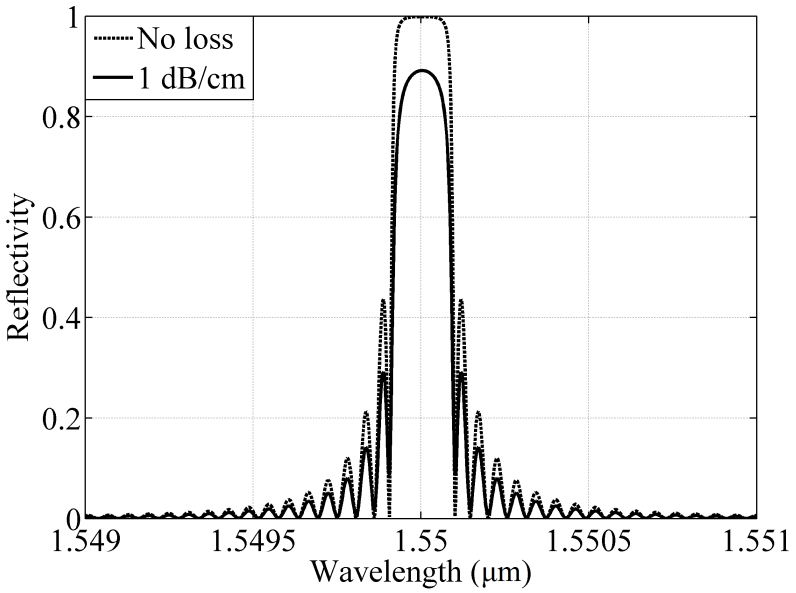

Figure 3.7: Reflectivity of FBG with $L_g = 2$ cm and $\Delta n = 10^{-4}$.

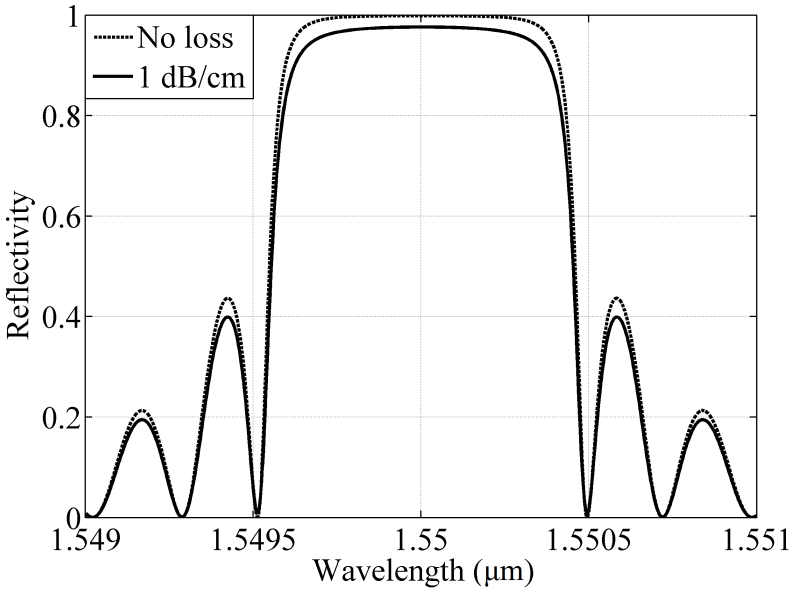

Figure 3.8: Reflectivity of FBG with $L_g = 4$ mm and $\Delta n = 5 \times 10^{-4}$.

that the reflection coefficient can remain relatively constant when the grating is under the influence of any environmental disturbances and slightly shifts its Bragg wavelength.

The fibre loss can affect not only the reflection and transmission coefficients of the grating, but also the penetration depth of the propagating light in the grating structure. As is mentioned above, the effective length is important because it determines the total cavity length of the interferometer. Figure 3.9 illustrates the dependence of the relative effective length L_{eff}/L_g on the reflectivity R of the grating and it shows the attenuation effects on the effective length. The attenuation effect on the relative effective length is higher as the reflectivity of the grating increases. The Figure 3.9

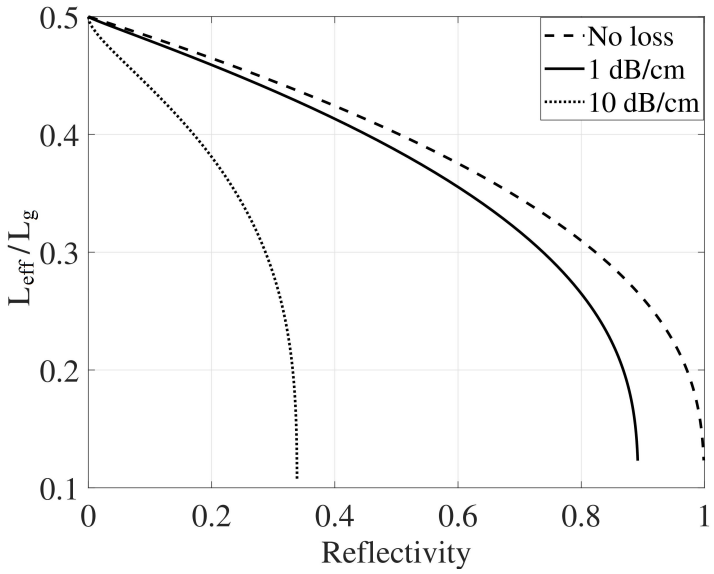

Figure 3.9: Relative effective length L_{eff}/L_g of a uniform FBG with $L_g = 4$ mm and $\Delta n = 10^{-4}$, without loss and with attenuation of 1 dB/cm and 10 dB/cm.

shows three different cases: without loss, 1 dB/cm, and 10 dB/cm, of a FBG with $\Delta n = 10^{-4}$. Table 3.2 shows the reflection r and the transmission t coefficients, and the effective length L_{eff} of a FBG with grating length $L_g = 4$ mm and refractive index change $\Delta n = 10^{-4}$. Note that the FBG reflection coefficient increases as the operating wavelength decreases, because in the same physical grating length there are more Bragg grating periods (because they are shorter in period). For example, the grating period difference between $\lambda = 1550$ nm and $\lambda = 850$ nm is 1550/850=1.83. Figure 3.10 illustrates the stress sensitivity of a FP sensor fabricated with two uniform FBGs with the same characteristics as Table 3.2. The plot shows that the same FP sensor operating at $\lambda = 1550$ nm can exhibit different stress sensitivity when it is constructed in a different type of fibre. The stress sensitivity of the PMMA FP sensor is affected dramatically by the fibre loss ($\alpha = 1$ dB/cm) at this wavelength, and reaches a maximum value when the interferometric cavity is only 15 mm. By increasing the cavity length beyond that point, the sensitivity starts to drop as the attenuation factor affects the finesse value to a higher degree. The silica FP sensor, which has higher Young modulus, can obtain the same stress sensitivity levels as PMMA sensor when its cavity length is 100 mm. However, the optimum cavity length for maximum stress sensitivity of SOF FP is 7 km due to the very low attenuation of silica at this wavelength. The CYTOP FP sensor offers higher stress sensitivity than PMMA FP when the cavity length is longer than 6 mm and it has an optimum cavity length at 72 m. In general, PMMA FP is better for short cavity lengths because of its low Young modulus, the sensitivity of SOF FP dominates for long cavities because of its low attenuation and CYTOP FP can be the best choice for medium cavity

Table 3.2: Characteristics of FBG.

Wavelength (nm)	Parameter	Fused Silica	PMMA	CYTOP
1550	r	0.4489	0.4162	0.4489
	t	0.5511	0.5106	0.5511
	L_{eff} (mm)	1.6528	1.6363	1.6528
850	r	0.8121	0.8112	0.8121
	t	0.1879	0.1877	0.1879
	L_{eff} (mm)	1.2191	1.2190	1.2191
650	r	0.9197	0.9196	0.9196
	t	0.0803	0.0803	0.0803
	L_{eff} (mm)	0.9921	0.9921	0.9921

FBG with $L_g = 4$ mm and $\Delta n = 10^{-4}$

Table 3.3: Characteristics of FBG with doubled refractive index change.

Wavelength (nm)	Parameter	Fused Silica	PMMA	CYTOP
1550	r	0.8553	0.8116	0.8553
	t	0.1447	0.1372	0.1447
	L_{eff} (mm)	1.1407	1.1367	1.1407

FBG with $L_g = 4$ mm and $\Delta n = 2 \times 10^{-4}$

lengths. The boundaries between these cavity length regimes are determined by the reflectivity of the interferometric mirrors and the operating wavelength influencing the fibre loss. If the refractive index change of the FBG from Table 3.2 is doubled, the reflection coefficient of the FBG can be improved as shown in Table 3.3, which will also improve the performance of the FP as shown in Figure 3.11. However, in this case the attenuation affects the PMMA sensor's performance more dramatically, and in this case the CYTOP FP sensor exhibits higher stress sensitivity compared with both PMMA and silica FP for all cavity lengths up to 45 m.

Figure 3.12 shows the same FP device as Figure 3.10, but this time operating at $\lambda = 850$ nm. The lower attenuation of PMMA in this wavelength region allows to PMMA FP sensors to have longer cavities whilst still maintaining high finesse. In this case, PMMA FPs have higher stress sensitivity than CYTOP and silica for cavity lengths up to 15.5 cm. CYTOP FP sensors are best with lengths between 15.5 cm and 31 m, but their optimum length is at 11 m. Fabricating cavities in CYTOP fibre longer than 11 m will result not only in a bigger size of the sensor, but also to a

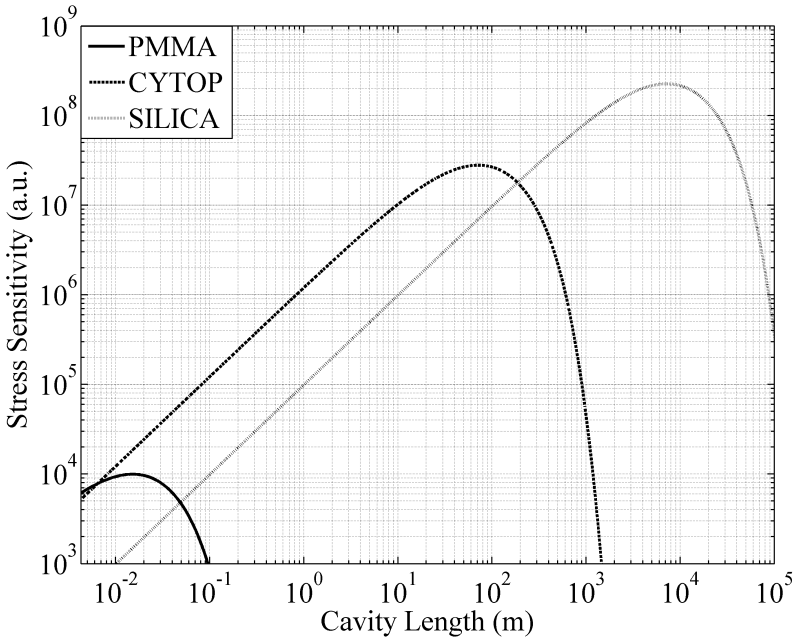

Figure 3.10: FP stress sensitivity with $L_g = 4$ mm, $\Delta n = 10^{-4}$, and $\lambda = 1550$ nm.

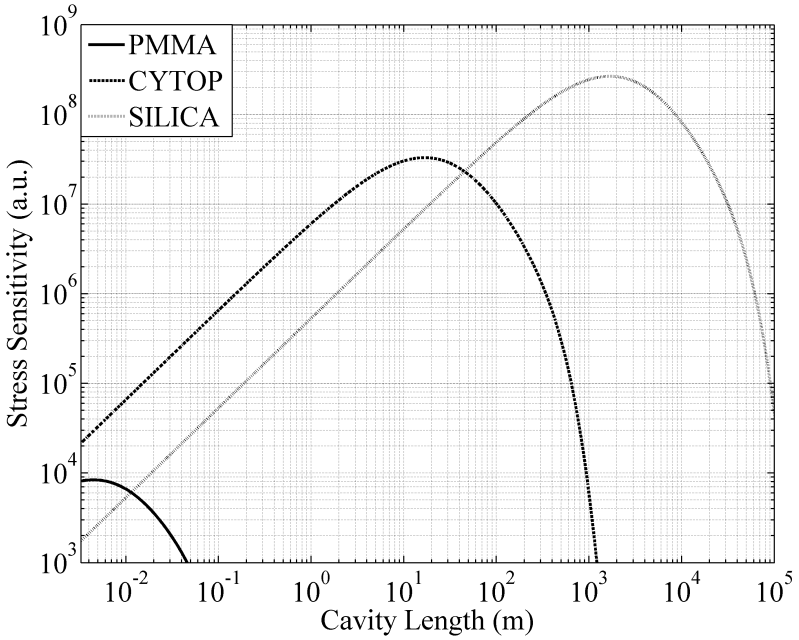

Figure 3.11: FP stress sensitivity with $L_g = 4$ mm, $\Delta n = 2 \times 10^{-4}$, and $\lambda = 1550$ nm.

significant reduction of its stress sensitivity, even if the cavity lengths between 11 m and 31 m offer higher sensitivity than the other materials. Figure 3.13 shows the same FP device as Figure 3.10, but it operates at $\lambda = 650$ nm. The PMMA FP sensor in the visible range has even less attenuation and its optimum cavity length is at 92 cm. CYTOP FP is the best with cavities between 1.2 m and 7.8 m, with the optimum length being at 2.6 m. Silica FP has optimum cavity length at 45 m. Note that the optimum cavity lengths for CYTOP and silica FPs become shorter as the operating wavelength decreases, due to the fact that the attenuation increases in these materials (Table 3.1).

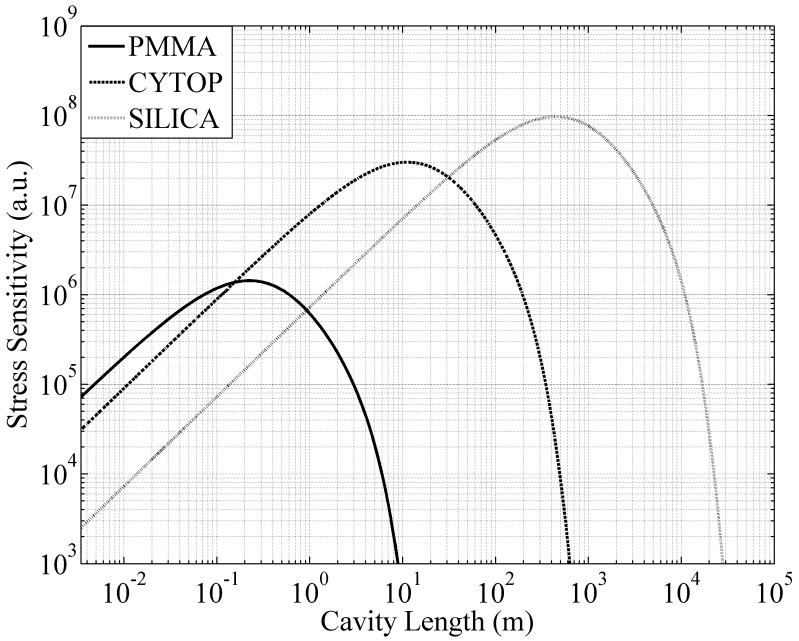

Figure 3.12: FP stress sensitivity with $L_g = 4$ mm, $\Delta n = 10^{-4}$, and $\lambda = 850$ nm.

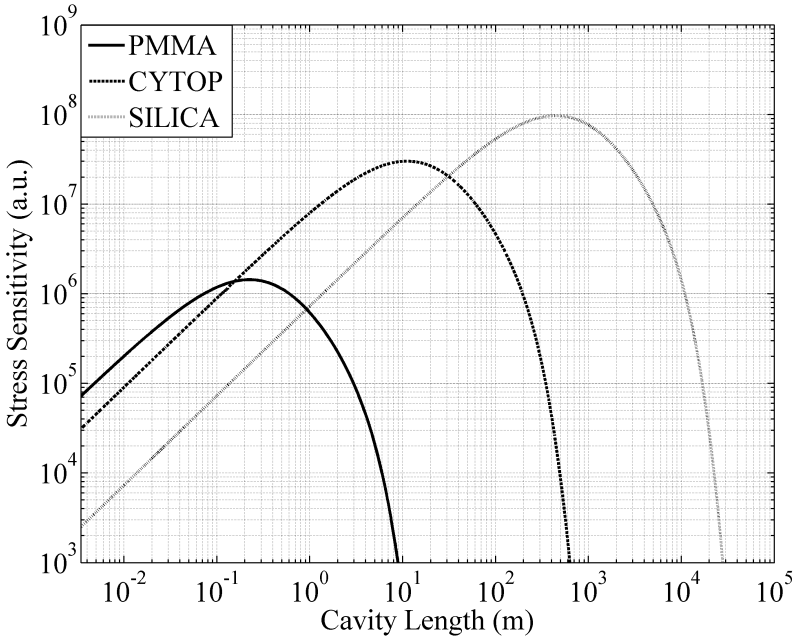

Figure 3.13: FP stress sensitivity with $L_g = 4$ mm, $\Delta n = 10^{-4}$, and $\lambda = 650$ nm.

The above results show that each FP sensor has a maximum stress sensitivity at its optimum cavity length. This optimum length depends on the fibre loss and the characteristics of its mirrors. As it is already mentioned, the reflection and transmission coefficients of the FBGs used to form the FP cavity define the sensitivity of the device. As the grating becomes larger, the reflectivity increases. Nevertheless, the reflection coefficient r of the grating cannot exceed unity and eventually saturates as the grating length continues to increase. In a lossless medium, the transmission coefficient t equals $1 - r$. However, this is not the case when the attenuation is

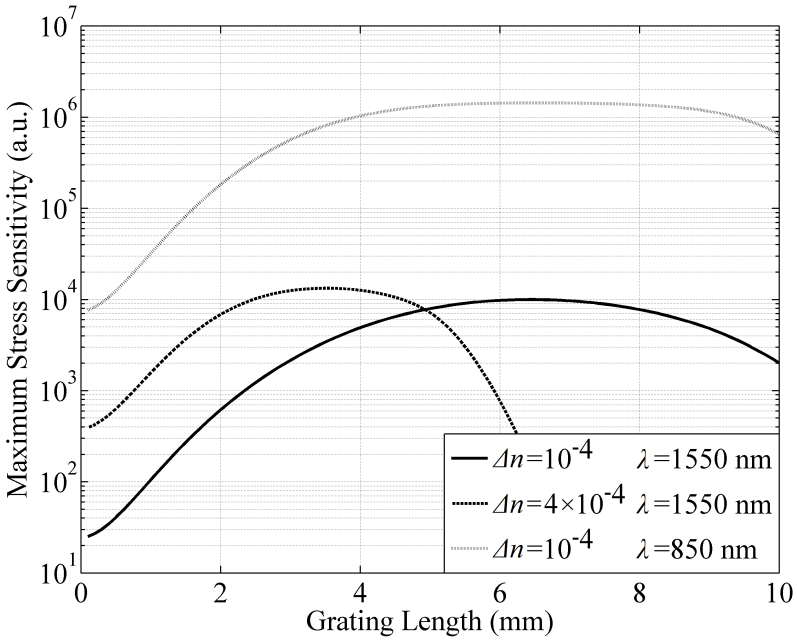

Figure 3.14: Maximum stress sensitivity of a PMMA FP sensor at its optimum cavity length for various grating lengths.

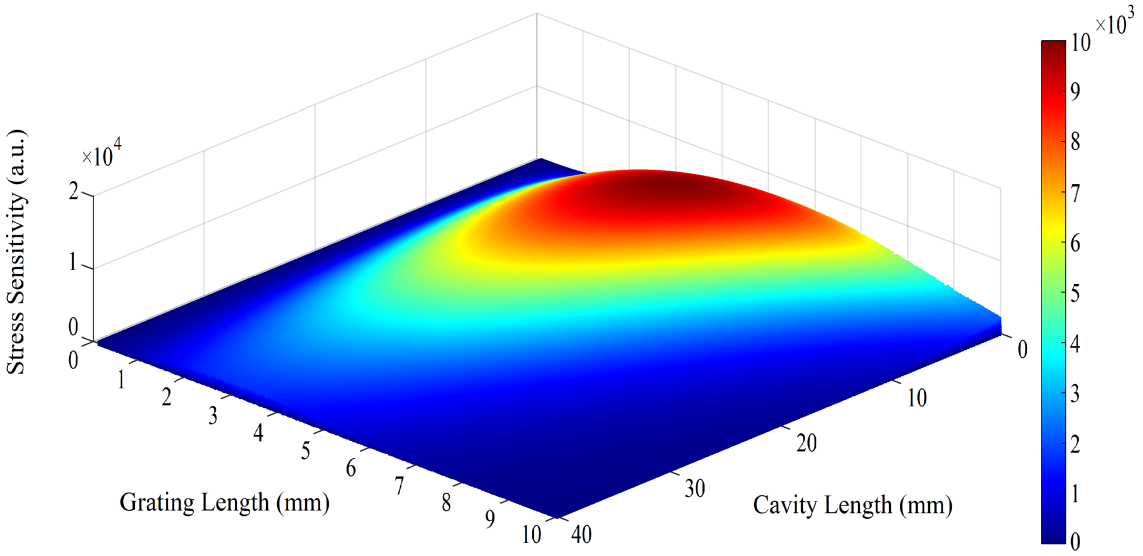

Figure 3.15: Stress sensitivity for various cavity lengths and grating lengths of a FP with $\Delta n = 10^{-4}$ and $\lambda = 1550$ nm.

significantly high; the coefficient t starts to drop as the grating length increases, which results in a sensitivity reduction of the interferometer after a certain point. Therefore, there is not only an optimum cavity length for maximum stress sensitivity, but there is also an optimum grating length. For each grating length, the maximum stress sensitivity of the FP at the optimum cavity length can have different value. Figure 3.14 shows the maximum stress sensitivity that a PMMA FP device can have at its optimum cavity length for different grating lengths. As illustrated in the plot, the

grating has also an optimum length to maximise the stress sensitivity. The optimum FBG length depends on the fibre loss (strongly depended by the operational wavelength), and on the refractive index change of the grating structure. To visualise this, Figure 3.15 shows in a 3D graph how the stress sensitivity of a PMMA FP with $\Delta n = 10^{-4}$ operating at at $\lambda = 1550$ nm varies with the grating length and the cavity length.

3.4 Conclusion

POF has a lower Young modulus compared with SOF, which renders POF based sensors more sensitive to fibre stress. However, when FP sensors are fabricated in POF, such as PMMA and CYTOP, the attenuation factor can influence their sensitivity. The model described in this chapter was developed to investigate the impact of the fibre loss on the system's performance. As the interferometric cavity length increases, the stress sensitivity of a FP sensor can reach a maximum value at a certain point – called here the optimum cavity length, but then starts to drop because the attenuation along the cavity becomes significantly important. The optimum cavity length changes accordingly with the fibre loss and the characteristics of the mirrors forming the interferometer. In the case where FBGs are used to form the interferometric cavity, there is also an optimum grating length that can provide even higher stress sensitivity at the optimum cavity length. The optimum grating length depends on the fibre loss and the refractive index change of the FBG.

Three different fibre materials are used in this model for illustration: PMMA, CYTOP and fused silica. The FP sensors have been also characterised in three different wavelength regions, where commercial components and detectors are readily available: 650 nm, 850 nm, and 1550 nm. However, the presented model is not limited to these materials or wavelengths, and it can be also used to characterise any FP interferometric device with the right adjustments. Comparing the three fibre materials the general conclusion is as follows. The PMMA FP sensors are the best for short cavity lengths because of their lower Young modulus, the silica FPs dominates for long cavities because of their lower attenuation and CYTOP FPs fit between the two materials and it preferable for medium length cavities. The boundaries of these cavity length regimes change accordingly with the operating wavelength which influence the fibre loss and the characteristics of the FBGs. In-fibre based FP interferometers are usually fabricated up to few centimeters and PMMA FP sensors can be the best candidate in most of the cases, especially in wavelength regions between 850 nm and 650 nm where PMMA fibre exhibits less attenuation than at 1550 nm. For larger FP devices or longer operating wavelengths, the CYTOP and then the silica can become preferable materials. Altogether, the model described in this chapter can be used to evaluate the performance of the FP stress sensor and identify which optical medium can offer the highest sensitivity when

the physical dimensions of the device have been already decided. On the other hand, it can be also used to calculate the physical dimensions of the FP device when the type of optical medium and the operational wavelength have been predefined.

4 Polymer Optical Fibre Bragg Grating Inscription with a He-Cd Laser System

One of the objectives was the fabrication of polymer optical fibre Bragg grating (POFBG) sensors for partners in order to develop novel applications. This chapter experimentally demonstrates various POFBG inscriptions utilising the helium cadmium (He-Cd) laser system. The applications that have been developed with these sensors are presented in chapter 7. The next section of this chapter shows the experimental setup that was used for the POFBG inscription, while section 4.3 shows the POFBG inscription results.

4.1 Introduction

The He-Cd laser used for the POFBG production emits at 325 nm, which is the most common inscription wavelength [14]. The typical POFBG inscription time in pure poly(methyl methacrylate) (PMMA) optical fibres is several tens of minutes. However, dopants can be added in POFs to enhance their photosensitivity and decrease the required inscription time to a few minutes. Section 4.4 demonstrates how the polymer optical fibre (POF) can be connectorised to facilitate easier POFBG interrogation compared with the butt-coupling method. As described in section 2.1.5, POF connectorisation technology is still in its infancy and more technological

advancement is needed such as commercially available automatic cleavers and splicers. The most common connectorisation method for single-mode POF is gluing two fibres together with the help of a UV lamp [97]. Recently, a new method of demountable connectorisation was demonstrated [98, 99], eliminating the difficulty of UV gluing and increasing the robustness of the connection. Improvements made to this approach are demonstrated in section 4.4. Section 4.5 demonstrates a novel method of POFBG multiplexing. Until now, it was only possible to tune the Bragg wavelength permanently to shorter wavelengths when utilizing thermal annealing, due to the tendency of POF to shrink when exposed above a certain temperature [35]. In this thesis, it is demonstrated for the first time that the Bragg wavelength can be also tuned to longer wavelengths permanently, when the POF is stretched and simultaneously exposed to heat.

4.2 Inscription Setup

A 30 mW continuous-wave He-Cd laser (Kimmon IK3301R-G), which emits monochromatic light at 325 nm, is used for the POFBG inscription, as illustrated in Figure 4.1. The beam from the He-Cd laser has a Gaussian profile and its $1/e^2$ diameter is 1.2 mm. The beam is focused into POF utilising a plano-convex lens, which has an effective focal length of 10 mm. In this case, the beam becomes elliptical with major axis diameter of 1.2 mm and minor axis diameter of 34 μm. The power density D at the focal point (considering a Gaussian beam) is equal to 187 W/cm^2 as calculated by:

$$D = \frac{2\,P}{\pi\, r_1\, r_2}, \tag{4.1}$$

which P is the power of the laser, and r_1 and r_2 are the radii of the elliptical beam. The POFBG inscriptions were made with the phase mask technique, which effectively splits the laser beam in two and creates an interference pattern (see Figure 2.12). The periodic interference pattern modifies the refractive index of the material periodically and the POFBG structure can be developed. The phase mask technique was chosen for the POFBG inscription, because it has a good long term stability and it is relatively easier to use, compared with the other techniques mentioned in section 2.2.3. The laser beam, which has a diameter of 1.2 mm, defines the physical length of the grating structure. However, the mirror 1 shown in Figure 4.1 is mounted on a high precision translation stage, thus the laser beam can be moved with a pre-defined constant velocity along the POF axis. Using the translation stage, longer grating structures can be inscribed. However, the area of the available phase masks is 10×10 mm^2, which limits the length to 10 mm. The process for the POFBG inscription is as follows. First, the POF is cut on a hot plate using a hot blade, because there are no commercial POF cleavers available yet. Both POF and blade are heated between 70 °C and 90 °C. The quality of the cleaving should be checked with the microscope, due

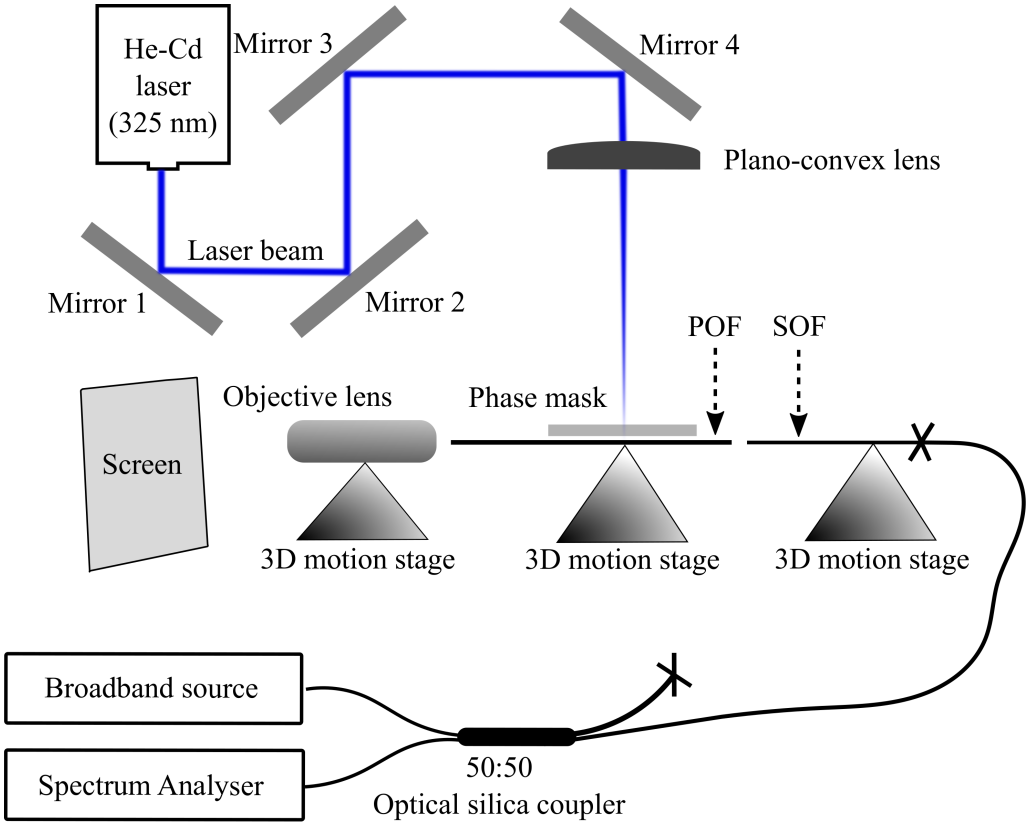

Figure 4.1: Fabrication setup of polymer optical fibre Bragg grating sensors.

to the uncertainty of the cleaving result. For illustration, Figure 4.2 shows the cross-section of a cut 3-ring hexagonal microstructured POF. After the cleaving, the POF is placed on the V-groove, which is aligned with the laser beam. The tip of the POF should protrude approximately no more than 1 mm from the V-groove to avoid any kind of fibre bending during the butt-coupling process. This value has been estimated empirically. At the next step, an angled silica patch cord is placed on a 3-axis movable stage in order to butt-couple it with the protruding POF. The reason of choosing an angled patch cord is to reduce the Fresnel reflections between silica optical fibre (SOF) and POF. A small amount of an index matching gel with refractive index of 1.49 can be also added at the tip of the silica patch cord to fill any possible air gaps during the butt-coupling and avoid any Fabry-Pérot cavity effects. Thereafter, a visible red laser (wavelength of 633 nm) is launched into the patch cord and the light is coupled into the POF. A magnifying 20X lens is placed at the other end of the POF to project an image of the illuminated fibre end on a screen. When the POF is aligned with the silica patch cord, the projected image shows a light present in the POF core, as illustrated in Figure 4.3. The brighter is the light in the centre, the better is the alignment. After the butt-coupling, the phase mask is placed on the V-groove plate. The periods of the phase masks that are used for the inscriptions described in this chapter are 558 nm, 580 nm, 1034 nm and 1061 nm. Before the exposure, the silica patch cord, which previously was connected with the red laser,

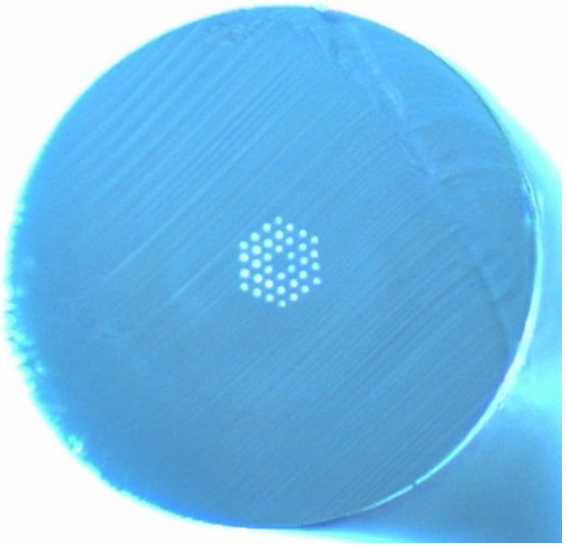

Figure 4.2: Cross-section of a cut POF.

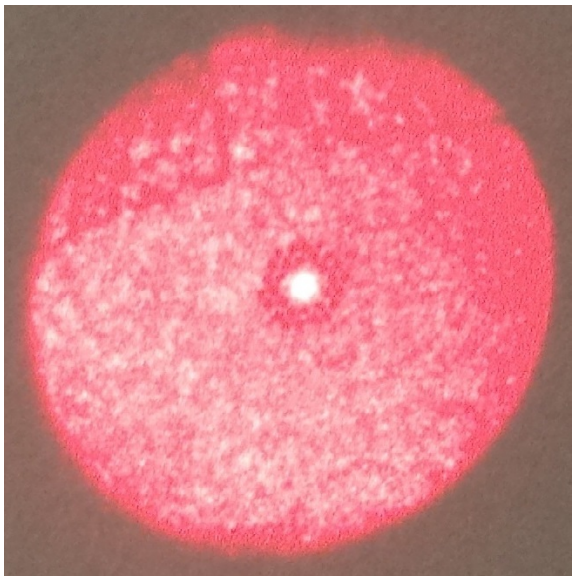

Figure 4.3: Projected image of POF during alignment.

can be now connected with the 50:50 single-mode silica coupler. The coupler is connected with a broadband light source and an optical spectrum analyser (HP 86142A), as shown in Figure 4.1. Two different super–luminescent light sources were used in this work: Superlum SLD-371 centred at 830 nm and Thorlabs ASE-FL7002-C4 centered at 1560 nm. This interrogation setup allows the monitoring of the Bragg grating spectrum in reflection.

4.3 Inscription Results

Various POFBG inscriptions have been conducted in different types of POFs: multi-mode (MM) and single-mode (SM), undoped and doped, step-index (SI) and microstructured optical fibres

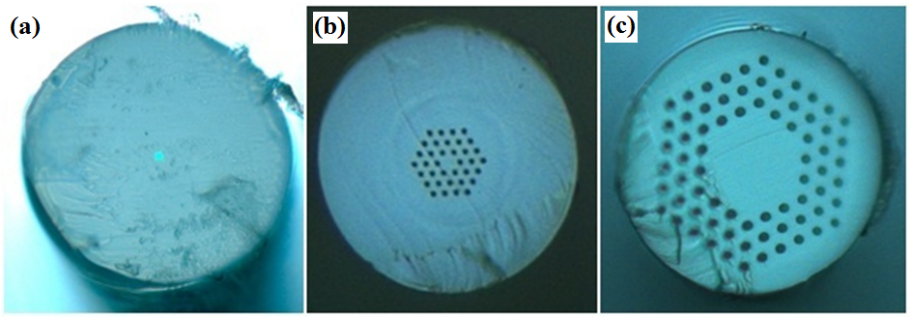

Figure 4.4: POF cross-section of (a) SM SI, (b) SM MOF, and (c) MM MOF.

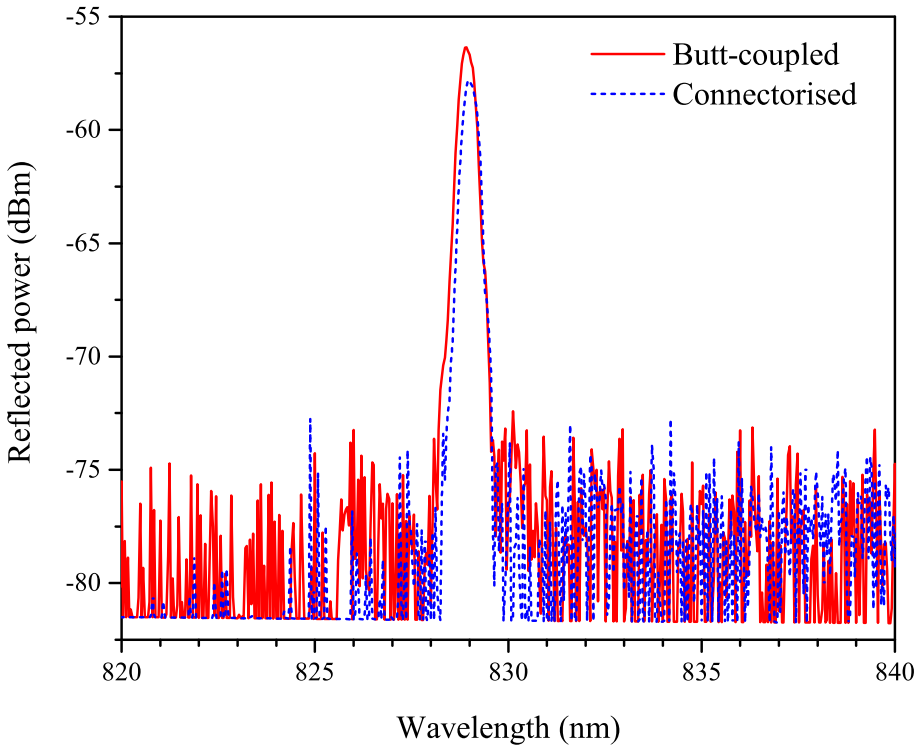

Figure 4.5: Reflection spectrum of butt-coupled and connectorised POFBG.

(MOF). Figure 4.4 illustrate three different types of POF structures: (a) SM SI, (b) SM MOF, and (c) MM MOF. These fibres are listed in Table 4.1 as POF 7, POF 14, and POF 15, respectively. The typical spectrum of a POFBG as observed in reflection (connectorised or butt-coupled) is depicted in Figure 4.5. The POFBG shown in this graph was inscribed in POF 1 (see Table 4.1) in 2 minutes using a phase mask with pitch 558 nm. Table 4.1 shows the characteristics of all POFs that have been used for inscription. The POFBG inscription time refers to the exposure duration until the saturation of refractive index change introduced in the material (considering that the laser beam is kept on the same position on the fibre). To define the inscription time, multiple POFBG

Table 4.1: Different types of POFs used for POFBG inscription.

POF	Type	Cladding Diameter (μm)	Core Diameter (μm)	Chemical Composition		Produced by	FBG Inscription Time (min)
				Cladding	Core		
1	SM MOF	130	8	PMMA	PMMA + BDK	A	1-17
2	MM SI	260	20	PMMA/PEMA (60/40 v%)	PMMA/PEMA/ PBzMA (50/45/3 v%) + BDK (2 v%)	B	3-5
3	SM SI	125	6	PMMA/PEMA (60/40 v%)	PMMA/PEMA/ PBzMA (50/45/3 v%) + BDK (2 v%)	B	8
4	SM MOF	200	6.3	PMMA	PMMA	C	45
5	SM MOF	250	7.8	PMMA	PMMA	C	45
6	SM MOF	200	4	PMMA	PMMA + Cumarine	C	45
7	SM SI	200	3	PMMA	PMMA + 2,4,6-trichlorophenyl methacrylate	C	45
8	SM SI	250	3.8	PMMA	PMMA + 2,4,6-trichlorophenyl methacrylate	C	45
9	SM MOF	200	9	TOPAS	TOPAS	D	45
10	SM MOF	180	10	TOPAS	TOPAS	D	45
11	MM SI	170	20	Zeonex 480R	TOPAS	D	45
12	SM MOF	140	9	PMMA	PMMA	D	89
13	SM MOF	130	8	PMMA	PMMA	A	89
14	SM MOF	125	8	PMMA	PMMA	E	89
15	MM MOF	150	50	PMMA	PMMA	E	89

A: D. Sáez-Rodríguez, et al. – Technical University of Denmark

B: B. G. D. Peng, et al. – University of New South Wales

C: O. Cetinkaya, et al. – Maria Curie-Skłodowska University

D: G. Woyessa, et al. – Technical University of Denmark

E: Kiriama Pty Ltd.

inscriptions were performed for each fibre type using full power (30 mW) of the laser. If different energy densities are going to be used, the inscription times listed in Table 4.1 will be different. To start a comparison between different fibre types, let us first take the POF 1 and POF 13, which are drawn with the same conditions using the same PMMA material. In this case, the core of POF 13 is undoped, but the core of POF 1 is doped with benzyl dimethyl ketal (BDK), which increases the photosensitivity of the material and reduces the POFBG inscription time from 89 minutes to less than 17 minutes. Note that the BDK dopant in POF 1 was not distributed evenly along the POF and consequently the inscription time varies between 1 and 17 minutes. POF 2 and POF 3 are also doped with BDK and the POFBG inscription time is a couple of minutes. Even though the POFBG inscription time in the undoped POF 12-15 is approximately 89 minutes, in the case of the undoped POF 4-8, it is 45 minutes. The reason could be the different polymerisation process that was used to link together the methyl methacrylate monomers. The quality of POF cleaving was also observed to be different between the two types of POFs; e.g. the average cleaving quality of POF 4 (see Figure 4.2) was higher than of POF 13 (see Figure 4.6). Note that the dopants used in POF 6-8 are not for photosensitivity enhancement, but for reduction of the fibre attenuation. Looking the results in Table 4.1, the chemical composition and the polymerisation process strongly affect the photosensitivity of the material. The photosensitivity of POF can be also dramatically enhanced when it is doped with BDK, which shows promising results regarding the POFBG inscription time (see POF 1 in Table 4.1).

4.4 Connectorisation of Polymer Optical Fibre Bragg Gratings

After the POFBG inscription, some POFs have been placed in demountable connectors to facilitate easier POFBG interrogation compared with the butt-coupling method described above. For the connectorisation method described in this section, a microstructured (3-ring) PMMA optical fibre was used. It has a diameter of 130 ± 20 μm and its core is doped with BDK for photo-sensitivity enhancement (see POF 1 in Table 4.1); for further details of the fibre fabrication, see reference [119]. The end of the fibre (approximately 4-7 cm) was chemically etched down to 125 μm utilising pure acetone in order to fit it into the 125 μm FC/PC connector. After etching, the fibre was placed into the connector and it was pulled until the non-etched part became stuck in the connector. Then, the protruding fibre from the connector was cut with a blade. Finally, a UV curing glue was added from the back of the connector to adhere the fibre into the connector. Figure 4.6 shows the cross-section of the POF placed into the FC/PC connector. It is empirically observed that the reflected POFBG spectrum can be dramatically enhanced when a gel with refractive index of 1.49 is added between the connectors, as shown in Figure 4.7. Perhaps the gel can fill any

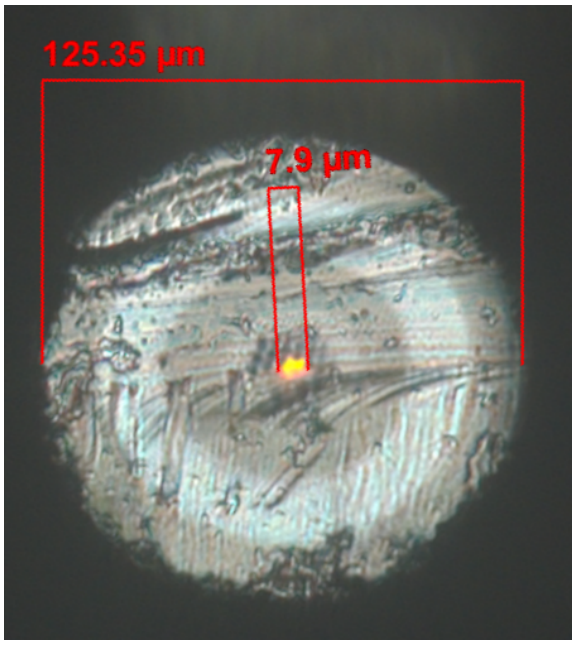

Figure 4.6: POF in the FC/PC connector.

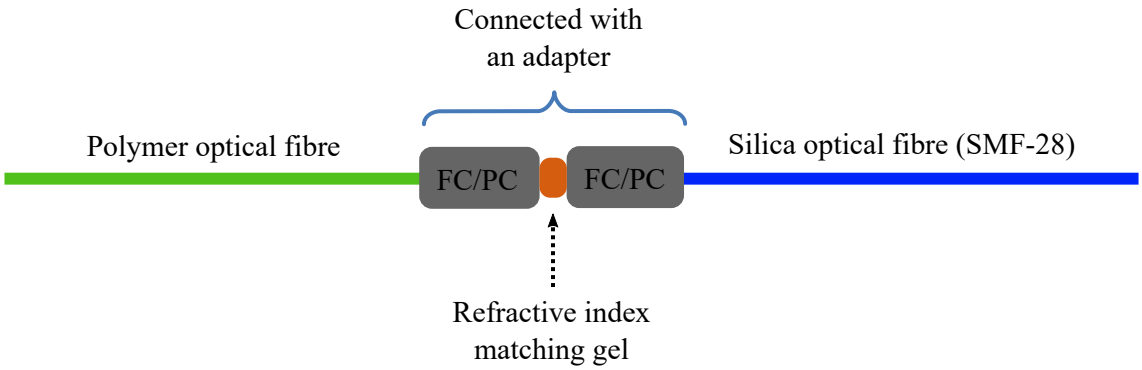

Figure 4.7: Scheme of POF connected with SMF-28.

gaps or defects occurring as a result of the cleaving process. Sometimes, the POFBG spectrum is not observable without the gel, especially when the strength of the grating is relatively low. The specifications for the POF placed into the FC/PC connector are listed in Table 4.2 and the specifications for the SMF-28 are listed in Table 4.3.

After connectorising both ends of the POF, the experimental scheme shown in Figure 4.8 was used to measure the POF connection loss. First, the two SOFs (typical commercial SMF-28 FC/PC patch cords) were connected between the broadband source and the optical spectrum analyser, as shown in Figure 4.8 (a), to obtain the transmitted spectrum of the source as a reference. Then, the POF was placed between the two SMF-28 patch cords, as illustrated in Figure 4.8 (b), and the new transmitted spectrum (with loss) was compared with the reference spectrum (without loss). Figure 4.9 shows an example of the spectrum with and without the POF, which indicates a total loss of 8.8 dB after the POF being connected into the system. The length of the fibre was 39.8 cm

Table 4.2: POF specifications obtained from [110] when it is placed in the FC/PC connector.

Core size (μm)	8
Diameter (μm)	125
Average pitch Λ (μm)	3.7
Hole diameter d (μm)	1.74
Relative hole diameter Λ/d (μm)	0.47
Refractive index at 850 nm wavelength	1.4840

Table 4.3: Specifications of SMF-28 FC/PC patchcord.

Core size (μm)	8.2
Diameter (μm)	125
Effective refractive index of cladding at 850 nm wavelength	1.4525
Effective refractive index of core at 850 nm wavelength	1.4577
Numerical aperture	0.14

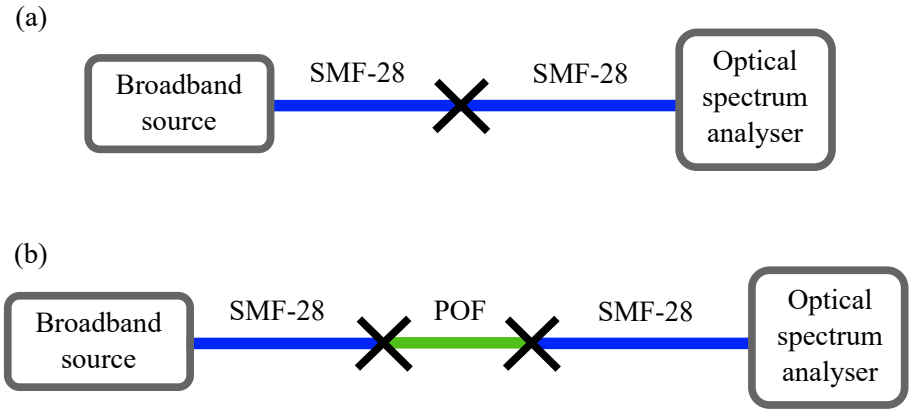

Figure 4.8: Experimental scheme to measure the POF connectorisation loss. The scheme shown in (a) is the reference system (without loss) and the scheme in (b) is the system with loss.

in this case, which implies 0.8 dB loss due to POF attenuation in the 830 nm wavelength region (approximately 2 dB/m) [31]. Therefore, the loss occurring from the two connectors was 8.0 dB, which implies an average loss of 4.0 dB for each connector.

The connectorisation technique described above can be further optimised by polishing the POF's end-face. The polishing sheets are similar to sandpapers, which have tiny particles glued to a polyester substrate. These particles can remove material from surfaces to make them smoother. The sheets used to polish the connectors have particles with size of 5 μm, 3 μm, 1 μm and 0.3 μm (Thorlabs LF5P, LF3P, LF1P, and LF03P). The polishing process starts by first using sheets with

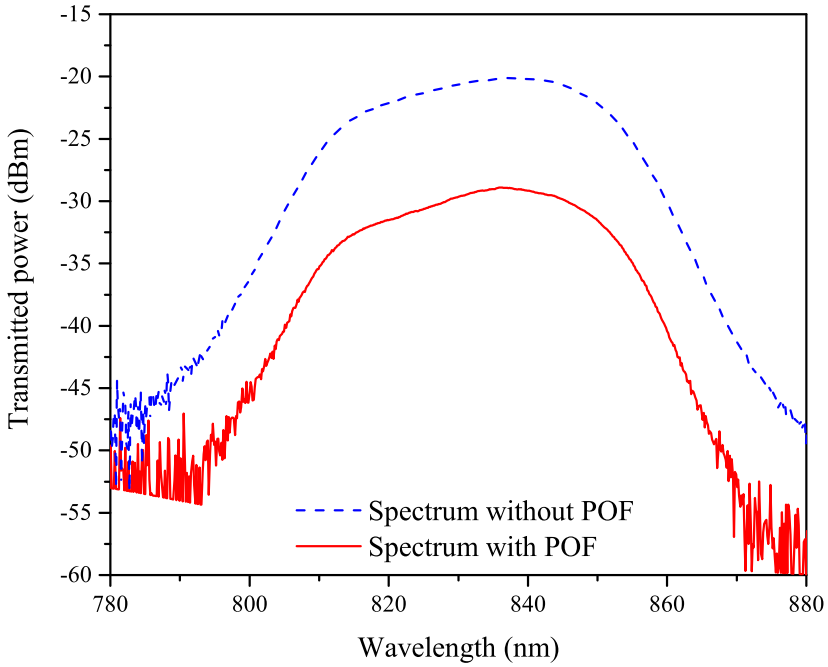

Figure 4.9: Transmitted spectrum with and without the POF.

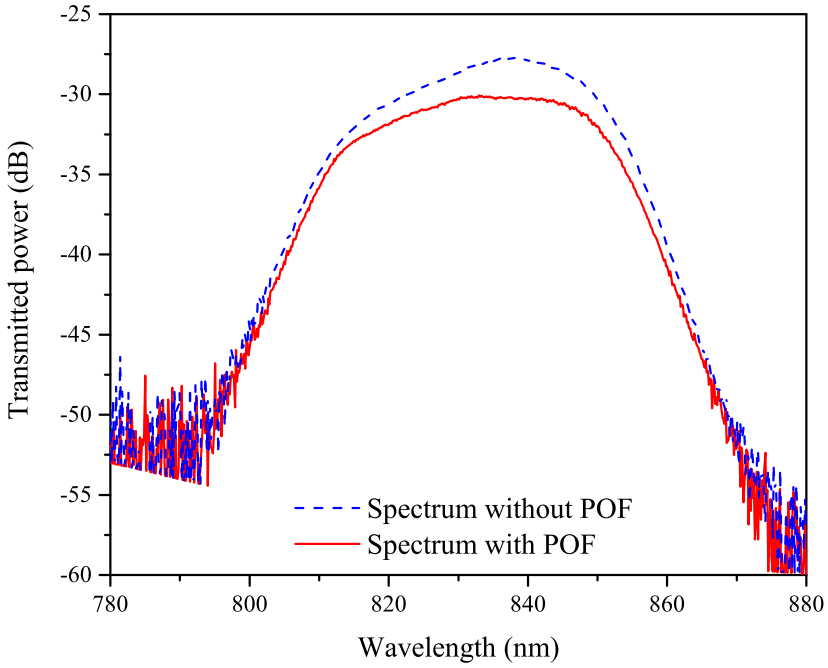

Figure 4.10: Transmitted spectrum with and without the polished POF.

5 μm grid, and then using 3 μm, 1 μm and 0.3 μm grits respectively. This is to first remove the large sections from the fibre surface and then the smaller ones for optimising the effectiveness of the polishing process. Figure 4.10 shows the spectrum of the source with and without the connectorised and polished POF being connected with the system. In this case, results indicate a total loss of 2.3 dB, which includes the loss from the two connections and the fibre attenuation

at 830 nm wavelength region. As the optical attenuation of PMMA at 830 nm wavelength is 2 dB/m [31], the 30 cm long fibre exhibits 0.6 dB loss. Therefore, the average loss per connector in this case is 0.85 dB, which is considerably lower compared with the recently reported connection loss of 8.45 dB in reference [98]. Furthermore, we should also consider that there is an additional loss when light passes through different refractive indices, core sizes and fibre types (step-index to microstructured), which is true in the case described above. Therefore, the connectorisation loss for single-mode POF can be further reduced with appropriate design of the fibre structure to enable an optimised matching of the mode fields.

4.5 Novel Methodology for POFBG Multiplexing

As is widely known, fibre thermal annealing can be used to permanently shift the Bragg wavelength of the grating [35]. Exposing the POF above the β-transition temperature, the molecules start to relax and the fibre shrinks. The fibre shrinkage causes the grating period to become shorter, as a result the Bragg wavelength blue shifts permanently. The degree of Bragg wavelength tuning depends on the annealing conditions (e.g. temperature, humidity, and annealing duration) [174]. This provides the feasibility to develop multiple POFBGs with different Bragg wavelengths in one fibre piece by utilising only one phase mask. For illustration, two POFBGs were inscribed in the same fibre (see POF 1 in Table 4.1) at 829 nm and 862 nm Bragg wavelengths using phase masks with period of 558 nm and 580 nm respectively. Following the inscription, the POF was placed on a hot plate that was heated at 60 °C. After 15 minutes, the temperature was increased to 75 °C for additional 45 minutes. Figure 4.11 shows the reflected spectrum of the two POFBGs during the annealing process, as they shift to shorter wavelengths. The reflected power of both POFBGs is affected by the thermal annealing. In this case, we believe the fluctuation of the reflected power is strongly affected by the non-uniform heat distribution on the hot plate. To have uniform temperature along the POF and relative constant ambient humidity, the thermal annealing process has been improved as demonstrated in chapter 6. Figure 4.12 shows the Bragg wavelength shift of the two POFBGs with annealing time. Note that the first point, shows the Bragg wavelength position before the POF is placed on the hot plate. Due to the negative thermo-optic coefficient of PMMA, the Bragg wavelength blue shifts when the POF is exposed at higher temperatures. However, the Bragg shifting due to temperature change occurs instantly; the following shifting is due to fibre shrinkage. Increasing the temperature after 15 minutes, the fibre annealing rate increases. Further investigation on fibre annealing rate with temperature is presented in chapter 6.

Until now, it was only possible to tune the Bragg wavelength to shorter wavelengths [35]. In

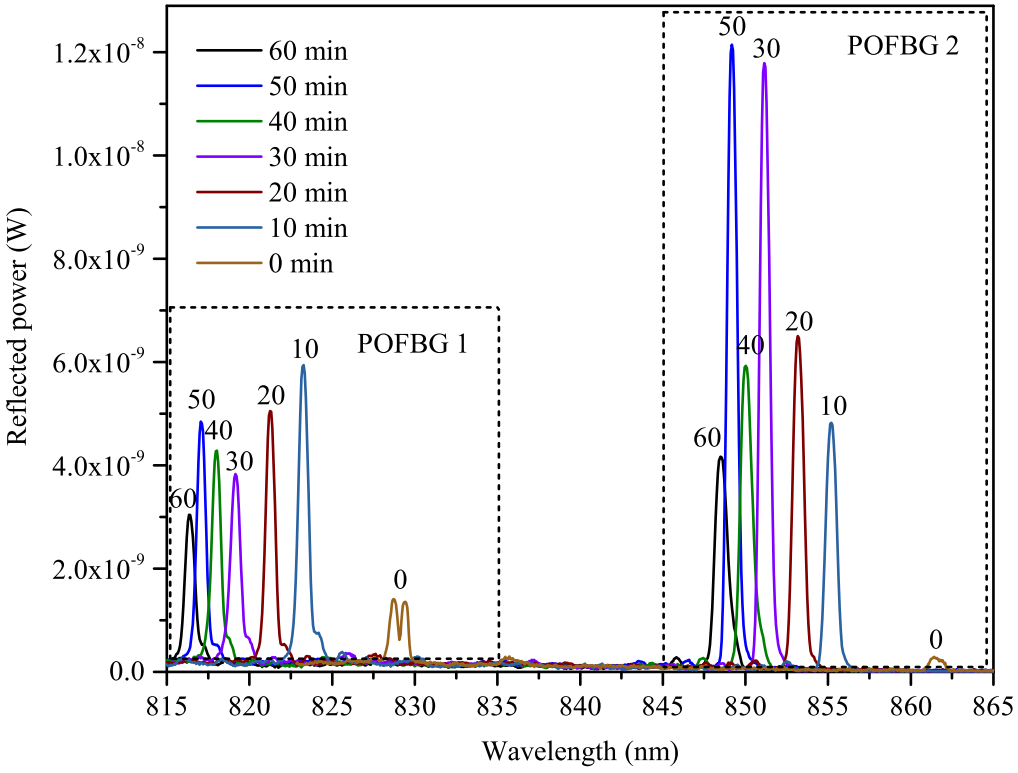

Figure 4.11: Reflected spectrum of two POFBGs during the annealing process.

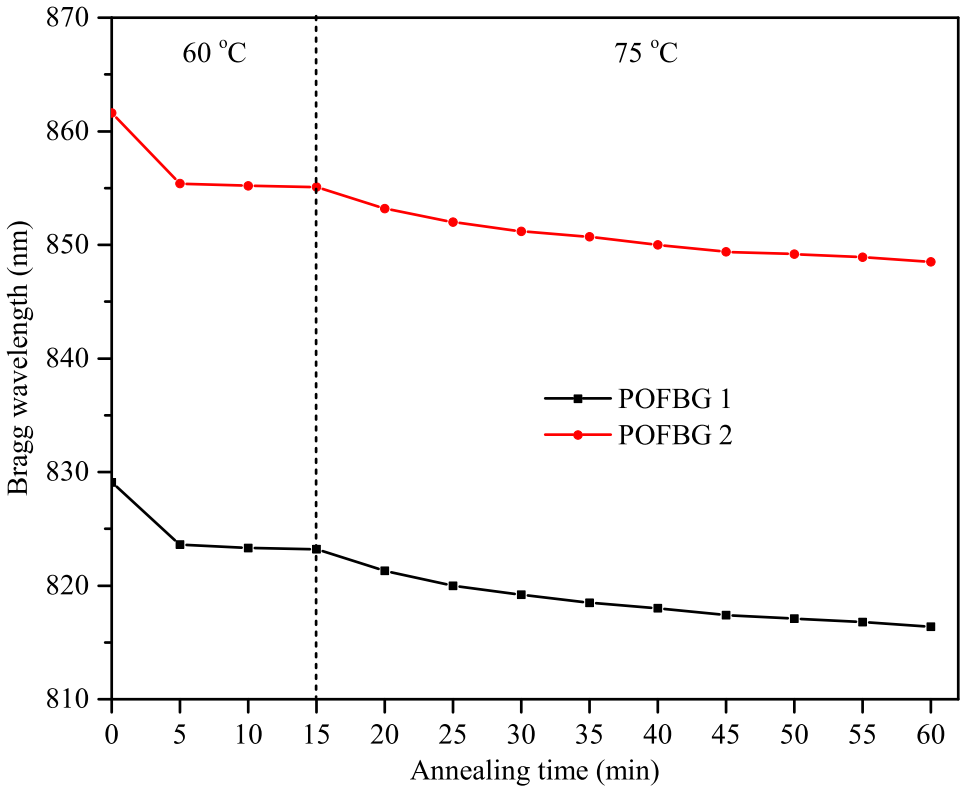

Figure 4.12: Bragg wavelength shift of two POFBGs during the annealing process.

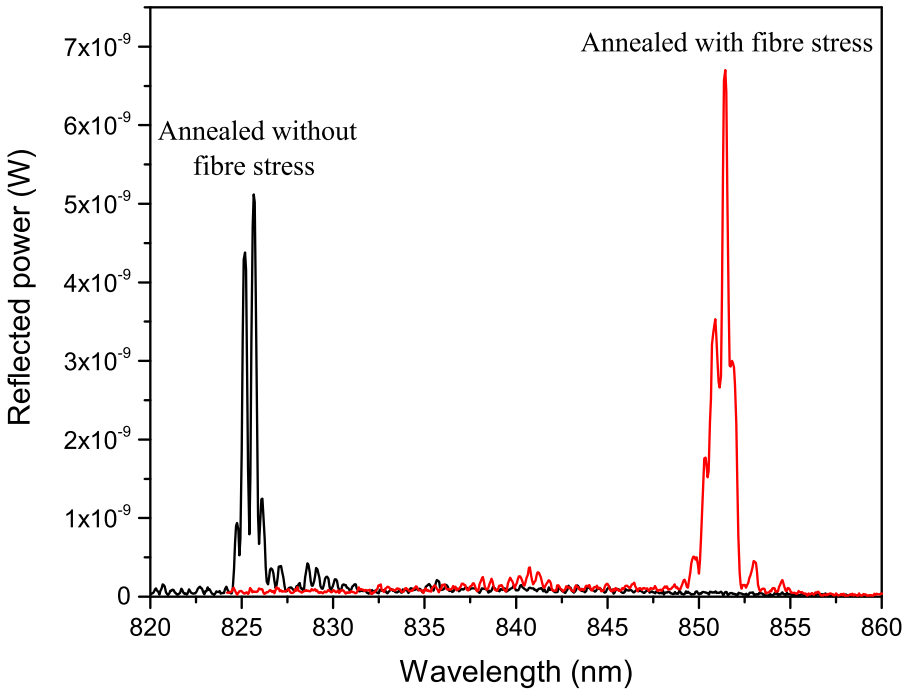

Figure 4.13: POFBG spectrum before and after the annealing process with fibre stress.

this thesis, tuning the Bragg wavelength permanently to longer wavelengths is demonstrated for the first time. To achieve that, the fibre should be kept stretched while it is heated up above the β-transition temperature of PMMA, which is 50 °C [36], and then it should rapidly be cooled down (while being stretched). In the first attempt, a POFBG was inscribed in POF 1 (see Table 4.1) with a Bragg wavelength at 829 nm. At the beginning, it was placed on a hot plate for 1-2 seconds without being stretched and the Bragg wavelength was tuned to 826 nm. Then, the fibre was stretched by hand for additional 1-2 seconds and suddenly was removed from the hot plate. In this case, it is observed that the Bragg wavelength was tuned permanently to a longer wavelength. The process was repeated 5 times and the Bragg wavelength was tuned from 826 nm to 856 nm (30 nm tuning). Then, the fibre was placed again on the hot plate without any fibre stress and the Bragg wavelength blue shifted back to 850 nm, which was the targeted wavelength. The spectrum before and after the thermal annealing process is shown in Figure 4.13.

An additional experiment was conducted, but this time the humidity, the fibre strain and the temperature were controlled. First, the fibre was strained 1% in order to have a constant stress applied on the fibre. Then, the fibre, while being stretched, was placed in a container filled with tap water (at room temperature) in order to have a constant humidity (100%) during the annealing process. The fibre was absorbing the water and the Bragg wavelength was shifting to longer wavelengths, as shown in Figure 4.14. After 40 minutes, the Bragg wavelength stopped

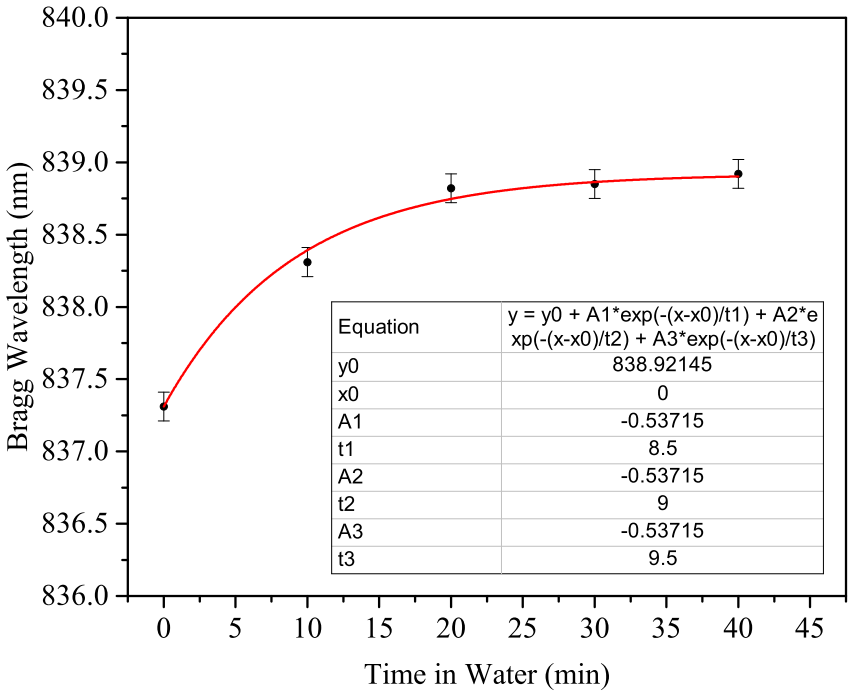

Figure 4.14: Bragg wavelength shift due to water absorption.

shifting, and the annealing process was started by heating the container utilising a hot plate. The temperature was monitored using a mercury thermometer (FISONS THL-290-050J). The Bragg wavelength shift with time and temperature is shown in Figure 4.15. After 45 minutes, the hot water was removed instantly from the container and the POF was cooled down (in an ambient room temperature) while being stretched. Then, the fibre was removed from the strain setup and the Bragg wavelength was read 1 hour later in order to allow the absorbed water to be released out of the POF. Figure 4.16 depicts that the Bragg wavelength has been permanently shifted from 828.7 nm to 832.9 nm.

The same experiment described above has been repeated with the same POFBG, but this time a 2% strain was used. Figure 4.17 shows the Bragg wavelength shift with temperature during the annealing process and Figure 4.18 shows the permanent Bragg wavelength position after each annealing process. The results show that the degree of wavelength tuning is directly related with the degree of strain (which defines the fibre stress). This process can be also applied in cases where it is desired to keep the Bragg wavelength at the same spectral position after the annealing process. This can be done by appropriately selecting the strain percentage. The strain sensitivity of the POFBG before and after the annealing process remained constant. However, the effects of this process on stress and temperature sensitivities of POFBG sensors are yet to be investigated.

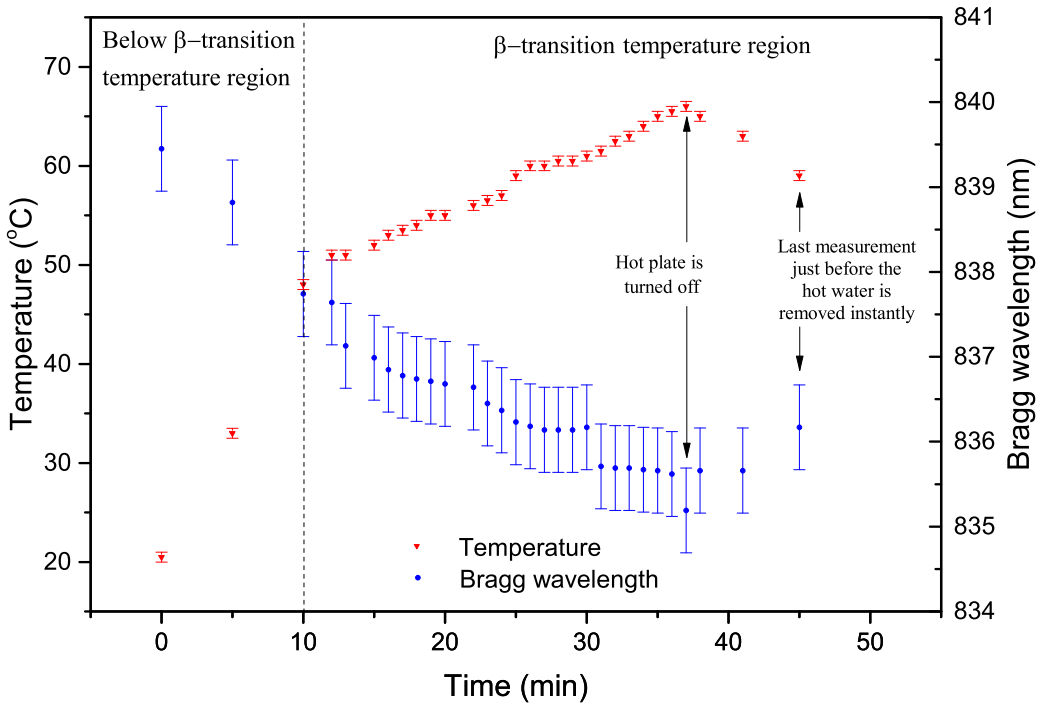

Figure 4.15: Bragg wavelength shift during the annealing process while the fibre is kept strained at 1%.

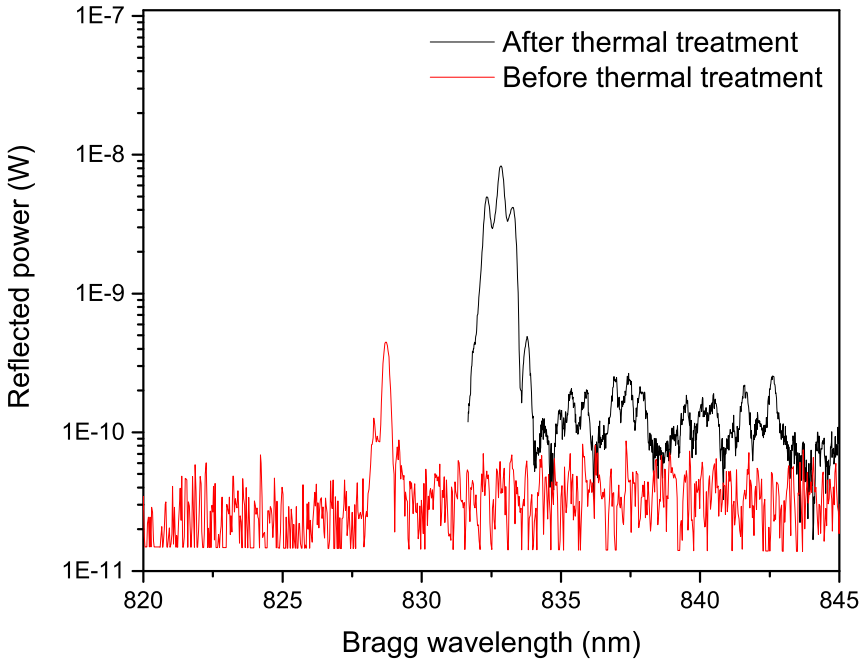

Figure 4.16: Bragg wavelength before and after the annealing process with constant fibre strain.

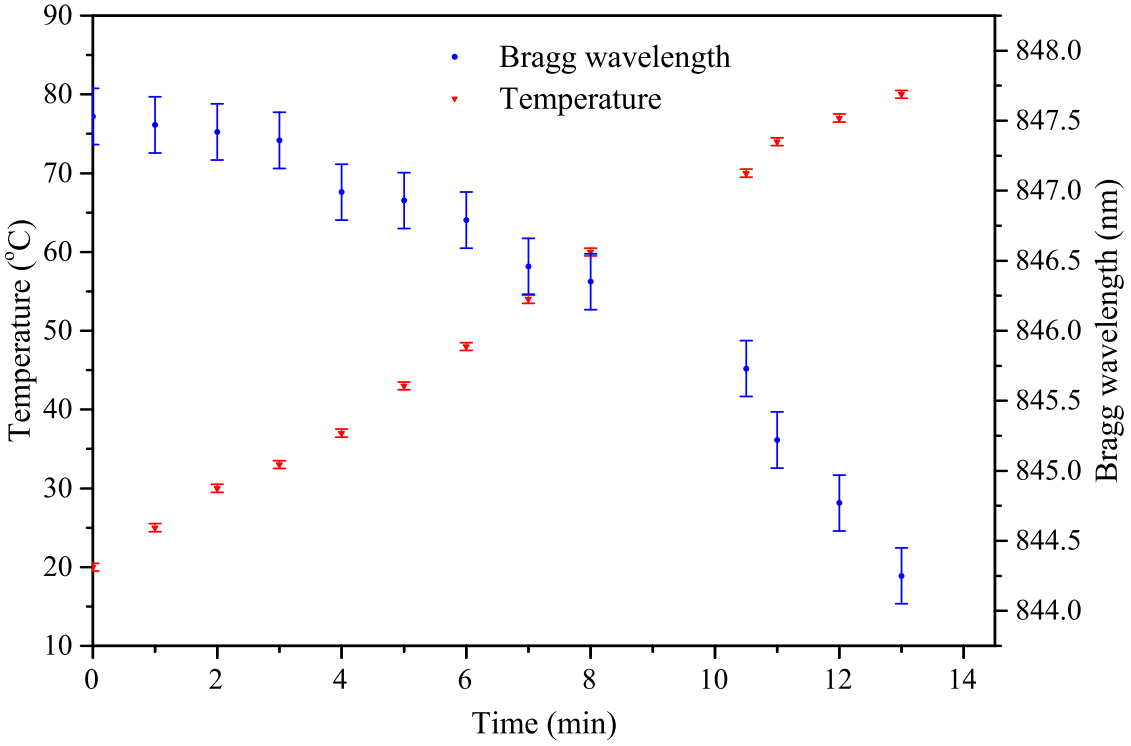

Figure 4.17: Bragg wavelength shift during the annealing process while the fibre is kept strained at 2%.

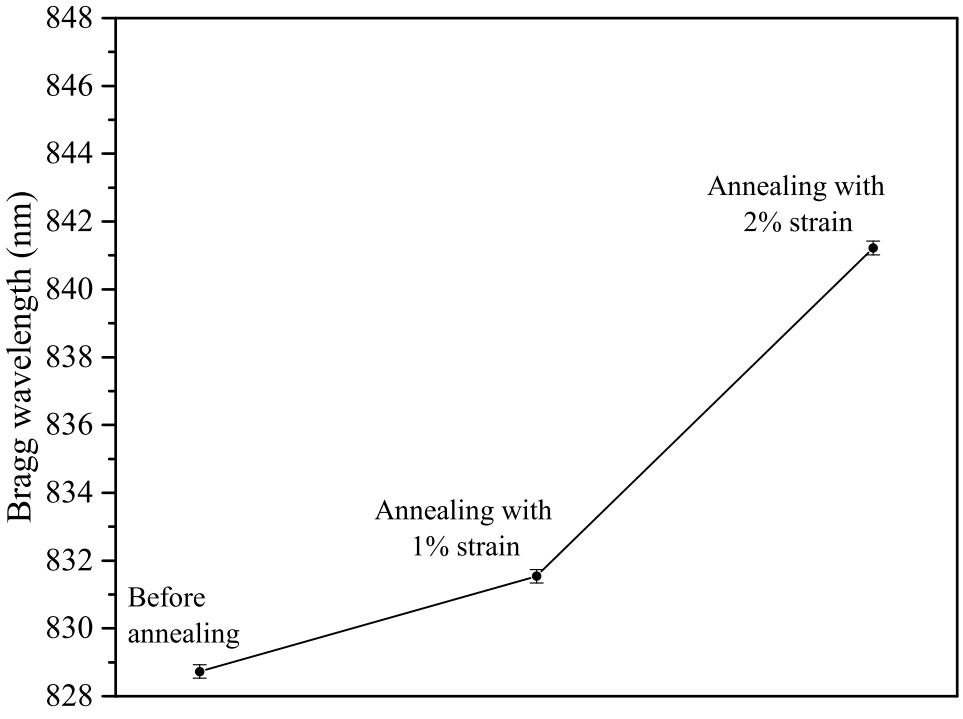

Figure 4.18: Bragg wavelength shift after annealing with 1% and 2% fibre strain.

4.6 Conclusion

In this chapter, POFBG inscription utilising the He-Cd laser system is demonstrated. The laser emits at 325 nm, which is the most common inscription wavelength in POFs. The typical POFBG inscription time in pure PMMA optical fibres is several tens of minutes. However, dopants (e.g. BDK) can be added in POFs to enhance their photosensitivity and decrease the required inscription time to a couple of minutes. A demountable connectorisation method is presented in this chapter, which exhibits less than 0.85 dB connection loss. At the end of the chapter, a novel methodology for POFBG multiplexing is also presented. A permanent Bragg wavelength tuning at longer wavelengths is experimentally demonstrated for the first time, by stretching the POF during the thermal annealing process. The work presented in this chapter can be used to effectively inscribe POFBG sensors at any desired Bragg wavelength utilising only one phase mask.

5 Polymer Optical Fibre Bragg Grating Inscription with a KrF Laser System

This chapter presents a novel methodology for POFBG inscription utilising a krypton fluoride (KrF) laser system. The KrF laser emits at 248 nm, and it was until recently impossible to inscribe Bragg gratings in polymer optical fibres (POFs) with this wavelength [33].

5.1 Introduction

When the first gratings in PMMA fibres were reported in 1999, the authors tried to inscribe with the 325 nm and 248 nm lasers [102]. However, the authors observed gratings in the fibre core only with the 325 nm laser. In the case of the 248 nm laser, there was a periodic ablation on the surface of the POF, because the PMMA absorption coefficient increases at shorter ultraviolet (UV) wavelengths [121]. For this reason, lasers emitting around the 325 nm wavelength became the preferred option for POFBG inscription until now. As described in section 2.1.5, the complex photosensitivity mechanisms involved in POFBG inscription are not fully understood yet. The photo-polymerisation, photo-crosslinking, and photo-degradation mechanisms likely coexist under irradiation, but which one prevails is possibly determined by the irradiation conditions, such as laser intensity, wavelength, pulse duration, fluence, and total exposure time[110]. In

1993, it was demonstrated a refractive index change in PMMA bulk materials [107], when then authors utilised a KrF laser with fluence of 40 mJ/cm^2 and repetition rate of less than 5 Hz. The success of the authors relied on the relative low energy density (i.e. fluence) and repetition rate. A material with a low effective absorption coefficient requires numerous laser pulses to exceed its ablation threshold, if the energy density during irradiation is relatively low [114]. Each laser pulse, which has an energy below the ablation threshold, modifies the molecular structure, and as a result the refractive index of the material can change. However, the effective absorption coefficient increases, due to chemical changes introduced in the material, and the ablation threshold becomes lower [175]. If the delivered energy density is higher than the ablation threshold, then the refractive index modification is not possible. The effective absorption coefficient of the material, the laser wavelength, and the laser pulse duration define the depth over which the laser energy can be effectively absorbed [176]. Therefore, a refractive index modification in PMMA is possible at shorter UV wavelengths, if the energy density and repetition rate of the laser is low enough.

The first POFBG inscribed with a laser wavelength below the 325 nm wavelength was reported in 2015 [33]. The authors used a 248 nm KrF laser system with a low fluence (33 mJ/cm^2) and repetition rate (1 Hz) to inscribe a uniform Bragg grating in the undoped core of a few-mode PMMA optical fibre. We should note that the reported fluence is without the laser beam being focused, and the authors used a plano-convex cylindrical lens with effective focal length of 20 cm for the inscription. Therefore, the energy density on the fibre was presumably much higher (approximately 480 mJ/cm^2). The inscription time until the POFBG became 'saturated' was less than 30 seconds (i.e. less than 30 laser pulses were adequate for the POFBG inscription). This is the fastest Bragg grating inscription reported until now using a UV laser system.

In this chapter, the first POFBG inscribed with a single laser pulse is demonstrated, which is much faster than any grating inscription method reported until now. A KrF laser system was used for the inscription, which has a pulse duration of 15 ns. The reflectivity of the grating is 98.4% and the introduced refractive index change is 0.74×10^{-4}, which is more than satisfactory for most sensing applications. The grating was inscribed in a single-mode PMMA optical fibre, the core of which is doped with BDK (see POF 1 in Table 4.1). The BDK dopant is a photo-initiator that triggers photo-polymerisation and possibly photo-crosslinking under irradiation. In addition, the BDK has a high absorption coefficient at 250 nm wavelength [118]. For this reason, a single 248 nm laser pulse was adequate to trigger a chemical process and change the refractive index of the material. The refractive index change possibly follows a second order exponential saturation over a period of a few minutes, as is shown below.

5.2 Inscription Setup

The POF 1 listed in Table 4.1 and Table 4.2 was used for the inscriptions in this chapter. This PMMA optical fibre is single-mode, 3-ring microstructured as shown in Figure 4.6, and its core is doped with BDK. Note that sometimes more than one peaks were observed in POF 1 with the He-Cd laser inscription (chapter 4). This is because the fibre is custom-made and the fluctuation of the diameter is more than 20 μm, which is perhaps the reason why some parts of the fibre are single-mode and some other parts are few-mode. As reported in chapter 4, the dopant in POF 1 reduced the required POFBG inscription time from 89 minutes to less than 17 minutes, when using the He-Cd laser system. For this reason, it was chosen to inscribe POFBGs with the KrF laser system. Before the POFBG fabrication, the fibre was cut in pieces of length between 15 cm and 35 cm, which were connectorised with the same method as shown in section 4.4; i.e. each fibre piece was glued into a FC/PC connector. After the connectorisation, each fibre was mounted on the setup to inscribe a POFBG utilising a KrF excimer laser (Coherent Bragg Star Industrial-LN), which emits light at 248 nm. The pulse duration of the KrF laser is 15 ns and the pulse energies used for the inscriptions were between 3.1 mJ and 6.3 mJ. The beam profile of the laser is a rectangular Tophat with dimensions 6.0×1.5 mm^2 and divergence 2×1 mrad^2. A cylindrical plano-convex lens (Newport CSX200AR.10) with focal length of 200.0 mm was used to focus the laser beam in the POF. The focal spot size on the POF is 32.4 μm in height and 20.0 mm in width. To inscribe the POFBGs, the experimental setup was used as illustrated in Figure 5.1, where the phase mask fabrication technique was used to form the interference pattern (see Figure 2.12). The period of the phase mask is 567.8 nm and its width is 10.0 mm. The PMMA optical fibres have an effective refractive index of 1.487 in the 850 nm wavelength region. Therefore, the Bragg wavelength is approximately centred at 844.4 nm (see equation 2.19). Occasionally, a slit was placed on the inscription setup (see Figure 5.1) to reduce the dimensions of the laser beam to a few millimetres. This would allow us to strain the fibre while being on the inscription setup (in order to shift the Bragg wavelength to longer wavelengths), move the laser beam to a different position on the phase mask, and inscribe a new Bragg grating structure. The above method is used for pure practical reasons in order to effectively inscribe multiple Bragg gratings in the same fibre. The POFBG spectrum was observed in reflection by utilising a 50:50 ratio single-mode optical coupler, similar with Figure 4.1. The transmission spectrum was obtained by connecting the POF between the optical spectrum analyzer (Yokogawa AQ6373B) and the super-luminescent diode (Superlum SLD-371-HP1).

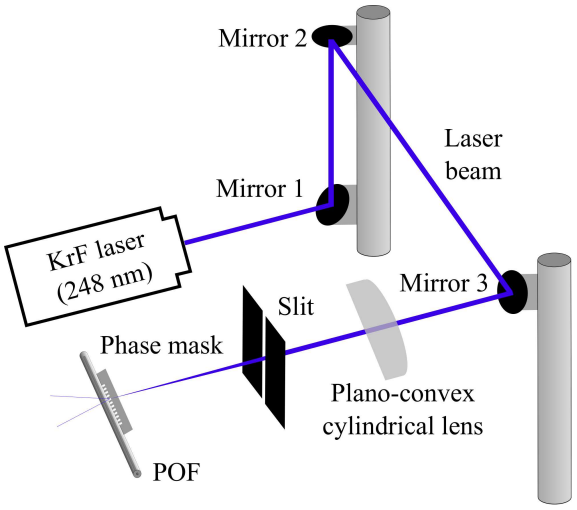

Figure 5.1: Apparatus for the gratings inscription.

5.3 Inscription Results

At the beginning, it was thought that more than one laser pulse would be required to inscribe a POFBG. Consequently, the POF was exposed with multiple pulses with the time between them being 10-20 seconds. The reflected power of the grating was monitored during the exposure process, in order to investigate how many laser pulses are required until the grating is 'saturated'. Figure 5.2 shows how the reflected power of grating varied with each laser pulse. First, laser pulses with energy of 3.1 mJ each were investigated. The energy density at the output of the laser was 35 mJ/cm^2, but when the laser beam passes through the 3.4 mm slit and plano-convex lens, its energy density on the surface of the fibre becomes approximately 482 mJ/cm^2. We should note that the calculation of the energy density present in the microstructured POF core area is complicated and it is out of the scope of this work. However, it is assumed that the energy density in the fibre core will be much less, considering the presence of the highly scattering 3-ring microstructured cladding and the high absorption coefficient of PMMA. The reflected power of grating inscribed with multiple 3.1 mJ laser pulses is depicted in Figure 5.2 (a). The second and third pulse reduced the power and above the forth pulse the power was increased. This shows the complex mechanisms involved during the photo-inscription. After the tenth pulse, the grating's reflected power reaches a saturation level, which is dropped on the following laser pulses. The same experiment was repeated, but this time each laser pulses had an energy of 5.5 mJ, which means an energy density of 61 mJ/cm^2 at the output of the laser. After the slit and the plano-convex lens, the energy density on the surface of POF was 855 mJ/cm^2. The reflected power of the grating varied with each laser pulse, as shown in Figure 5.2 (b). In this case, due to the higher energy density, the reflected power of the grating saturates on the eighth pulse. Note that these and the following plots show

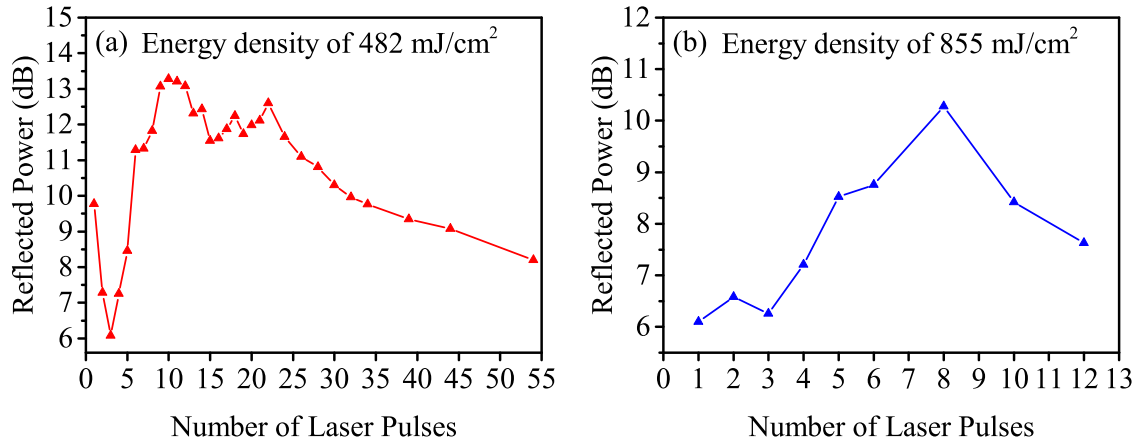

Figure 5.2: Reflection of POFBG after a number of laser pulses with energy density of (a) 482 mJ/cm^2 and (b) 855 mJ/cm^2.

the reflected power of the grating as measured from the background noise level. Therefore, these plots provide only a qualitative comparison between the different inscriptions, and they do not represent the true reflection coefficient value of the grating. The reflected power of the POFBG could be different in each case due to high insertion losses introduced by the custom-made fibre connectorisation. These plots represent only the effect of each pulse on the reflected power and investigate when the saturation level of the grating occurs. In the following results, a transmission spectrum is shown and a quantitative measurement of the grating's reflectivity is presented.

The pulse energy was increased to 6.3 mJ in the following experiment, which provided an energy density of 974 J/cm^2 on the POF's surface. In this case, the grating saturation occurred on the fifth laser pulse as shown in Figure 5.3 (a). Then, the same experiment was repeated with the same energy density, to see if the same results can be repeated. In this case, it was noticed that the reflected power was changing from 15 dB to 22 dB for approximately 4 minutes. Therefore, it was decided to increase the time interval between the laser pulses to 4 minutes, in order to allow any chemical reactions of the material to be completed. The results are shown in Figure 5.3 (b). Following the second laser pulse, the reflected power of the grating decreases. This graph clearly shows that the time interval between the laser pulses is an important parameter to consider during the POFBG inscription. To further explore the above phenomenon, an additional experiment was performed with the same inscription parameters (energy density of 974 J/cm^2), but this time the reflected power was monitored following irradiation with just one laser pulse. Figure 5.4 depicts the reflected power growth rate over time after a single laser pulse with energy density of 974 J/cm^2. The reflected power follows a second order exponential saturation for 4 minutes. Similar exponential saturation behaviour during POFBG inscription was reported in the literature in 2004 [177]. The authors produced Bragg gratings in a dye-doped PMMA optical fibre

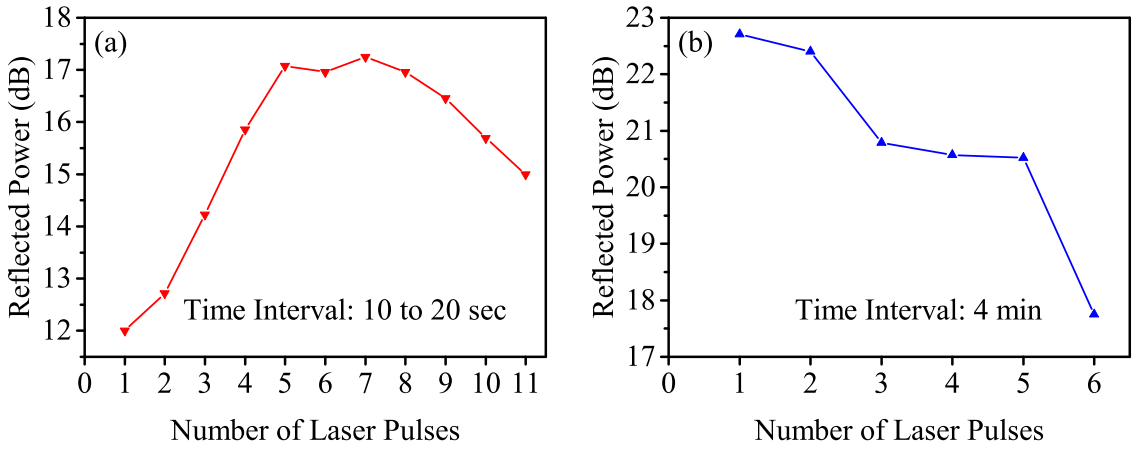

Figure 5.3: Reflection of POFBG after a number of laser pulses with energy density of 974 J/cm^2 and time interval of (a) 10 to 20 sec and (b) 4 min.

using a pulsed 325 nm neodymium-doped yttrium aluminium garnet (Nd: YAG) laser. Each laser pulse of 5 ns duration was delivering 4.5 mJ energy with a repetition rate of 10 Hz. The total inscription time was 88 minutes. After the illumination, the reflectivity of the Bragg wavelength was increasing from zero to more than 60% for 8 hours. The growth rate observed by the authors had a similar dynamic as in the case shown in Figure 5.4. However, the reflectivity of the grating saturated much faster in our case (less than 4 minutes), while in the case with the Nd: YAG laser, the chemical changes in PMMA were made at a slower rate (8 hours).

In the meantime, various POFBGs were produced with single and multiple laser pulses with energy density of 974 J/cm^2. However, their reflected power was greatly decreased the following day, as illustrated in Figure 5.5. We should note that all the above grating inscriptions were made in non-annealed fibres. Recently, a decay of POFBGs' reflectivity after their inscription process was reported in non-annealed PMMA optical fibres [178]. The authors experimentally showed that the reflectivity of the grating can be recovered and improved, when a post-annealing is applied on the fibre. Therefore, to test if the reflectivity can be recovered, the non-annealed Bragg grating shown in Figure 5.3 (a) was thermally annealed the next day after its inscription. To perform the thermal annealing, the POF was placed in container filled with hot water for 2 minutes. The water was heated with a hot plate at 55$\pm$1 °C. More details about the annealing process can be found in chapter 6. The reflected power of the grating before and after the fibre annealing is shown in Figure 5.6. As illustrated, the reflectivity of the grating was recovered by the annealing process. To further explore the impact of the thermal treatment on the POFBG's lifetime, an additional fibre was pre-annealed for 10 minutes with the same annealing conditions as previously and a grating was inscribed with energy density of 974 J/cm^2. At the same time, an additional grating was inscribed with the same energy density in a non-annealed POF and then it was post-annealed

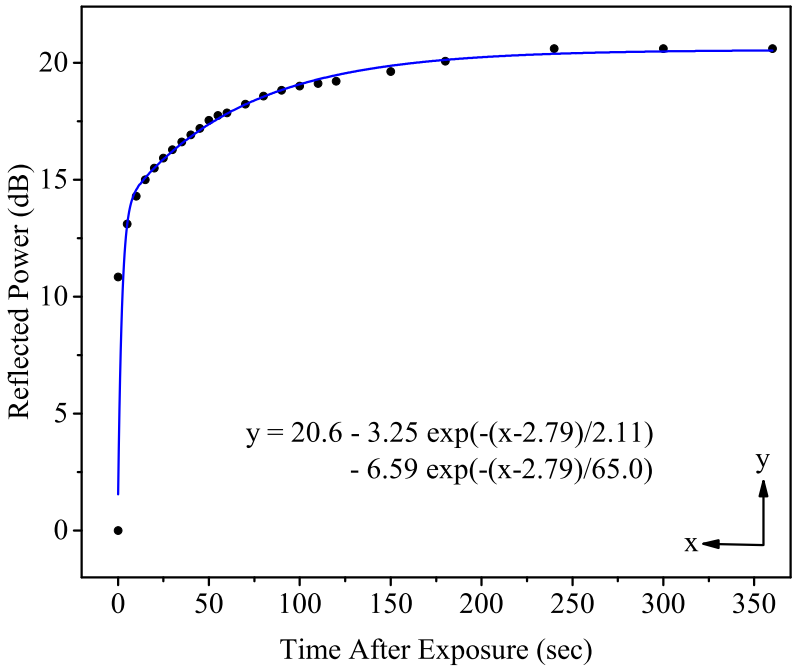

Figure 5.4: Reflected power growth rate over time after a single laser pulse with energy density of 974 J/cm^2.

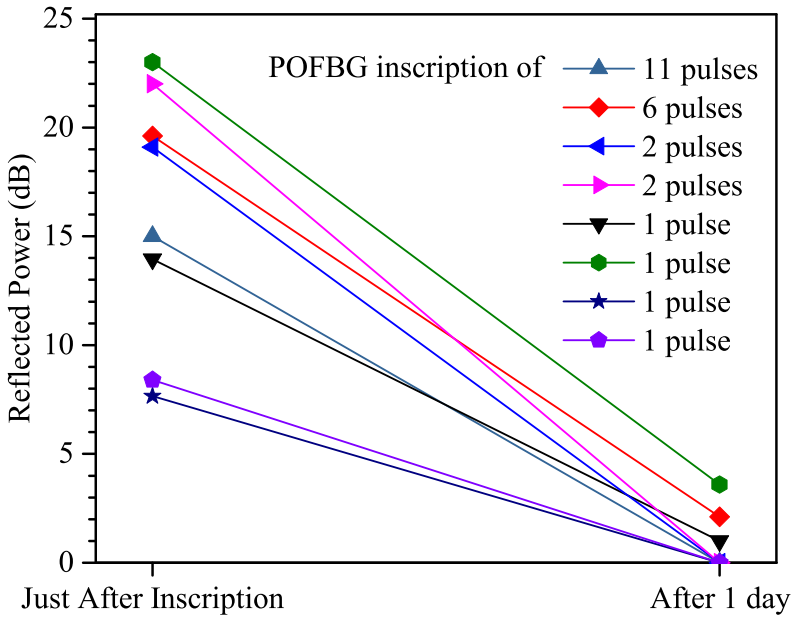

Figure 5.5: Reflected power of non-annealed POFBGs just after inscription and after 1 day.

with the same annealing conditions for 2 minutes. Figure 5.7 shows the importance of both pre- and post-annealing on the lifetime of POFBGs.

Taking into account the above results, one laser pulse on a pre-annealed fibre should be adequate to inscribe a grating. To obtain quantitative data as to the grating's reflectivity, the

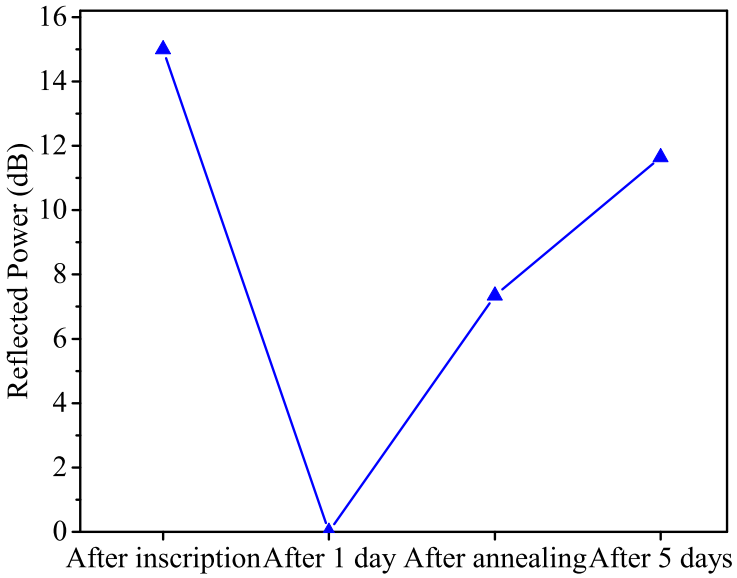

Figure 5.6: Reflected power before and after the thermal annealing process.

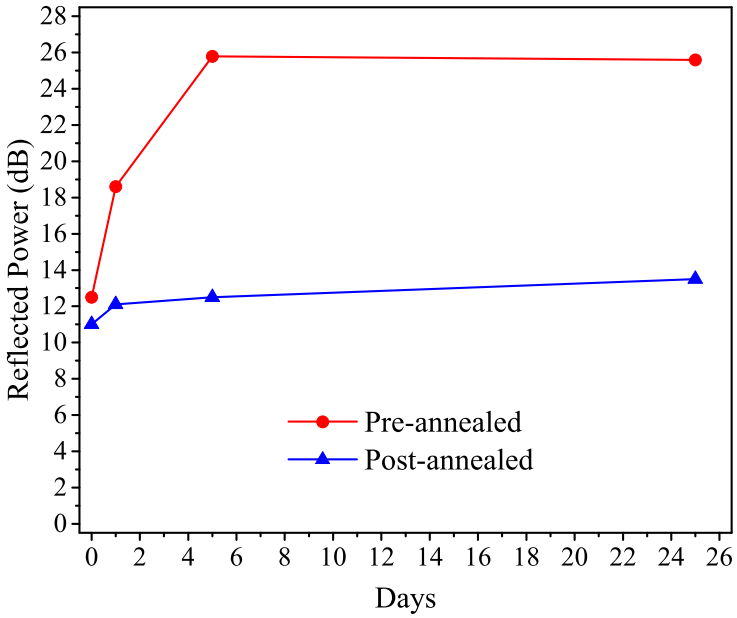

Figure 5.7: Lifetime of pre-annealed and post-annealed POFBGs.

spectrum of the grating should be also checked in transmission. To perform this experiment, a 30 cm long fibre piece was first pre-annealed for 30 minutes in a container that was filled with water heated at 55±1 °C. After the annealing, the POF was connectorised on both sides by gluing it in FC/PC connectors. The spectrum as seen in transmission before and after the connectorisation is depicted in Figure 4.10. The total loss is 1.7 dB, with the average loss per connection being 0.85 dB. After the connectorisation, the fibre was placed on the inscription setup shown in Figure 5.1. However, the slit was detached from the inscription system, in order to

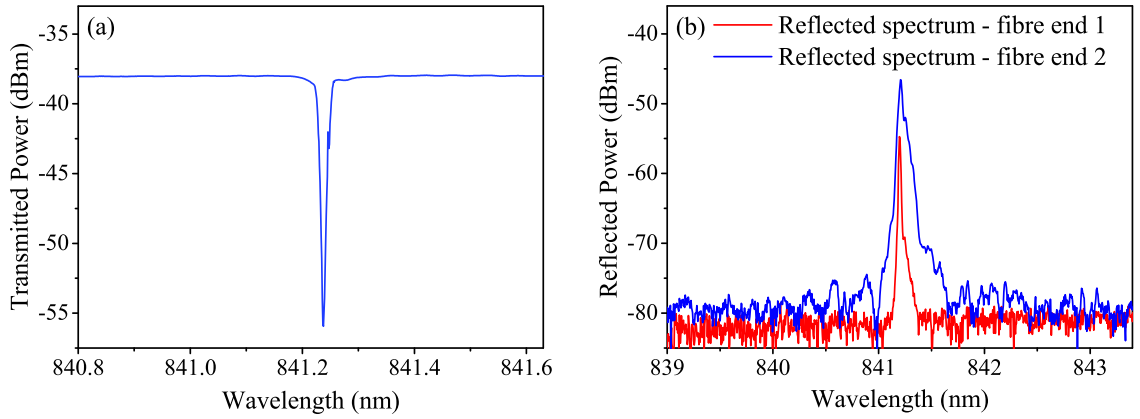

Figure 5.8: (a) Transmitted and (b) reflected spectra of the POFBG inscribed with one UV laser pulse.

increase the width of the laser beam that illuminates the POF. The maximum width of the laser beam at the location of the fibre is 20 mm (due to beam divergence), but the maximum grating length that can be produced is limited by the phase mask width, which is 10 mm. To inscribe the POFBG, a pulse energy of 6.3 mJ was used, which provides an energy density of 974 mJ/cm^2 on the fibre surface. The POFBG structure was produced with a single laser pulse exposure; its transmitted and reflected spectra are shown in Figure 5.8, which were obtained 7 days after the exposure. Figure 5.8 (a) shows the transmitted spectrum of the grating, which indicates a 17.9 dB transmission rejection, and Figure 5.8 (b) shows the reflected spectrum from each fibre end. The grating reflection is not identical from each fibre side, because it strongly depends on the insertion loss introduced by the fibre connectorisation. The reflected power is 27.3 dB from noise level at one end and 31.5 dB at the other end. The Bragg wavelength depicted in Figure 5.8 (b) is centred at 841.2 nm, but the phase mask inscribed a Bragg wavelength centred at 844.4 nm. The Bragg wavelength shift is due to fibre strain release when it was removed from the inscription setup. The POF is usually placed with some tension on the inscription setup to avoid the fibre bending or any other movement during the POFBG inscription. The transmission rejection of 17.9 dB indicates a reflectivity of $R = 98.4\%$. Taking into consideration the Bragg wavelength $\lambda_B = 841.2$ nm and the length of the POFBG ($L = 10$ mm), the maximum change of refractive index introduced in the POF is Δn=0.74$\times 10^{-4}$ since

$$R = tanh^2\left(\frac{\pi\,\Delta n\,L}{\lambda_B}\right). \tag{5.1}$$

5.4 Conclusion

In this chapter, the first POFBG inscribed with a single UV laser pulse is presented. The inscription was made in a single-mode PMMA optical fibre, with a core doped with BDK in order to enhance its photosensitivity in the UV wavelength region. The KrF laser used for the inscription emits light at 248 nm. Until recently, it was impossible to inscribe with this wavelength, due to ablation issues. A single laser pulse with 974 mJ/cm^2 energy density was adequate to introduce 0.74×10^{-4} refractive index change in the fibre core. The 10 mm long POFBG rejects 17.9 dB in transmission, which is translated to 98.4% grating reflectivity, which is more than enough for most sensing applications. The results show that the reflected power from the grating structure increases after the laser pulse for few minutes. This could indicate that the BDK photo-initator triggered a photo-polymerisation, and perhaps a photo-crosslinking process. The reflected power of the grating decreases after exposing the polymer material with a certain number of laser pulses. In this case, a possibly photo-degradation occurs in the polymer, in which the molecular bonds start to split. Investigating different energy densities for the inscription is still needed to optimise the inscription conditions. Finally, the importance of pre- or post-annealing process on the lifetime of POFBG devices is emphasised.

In conclusion, the ability to effectively inscribe Bragg gratings is demonstrated. This work will have a potential impact in industry, where a lower production cost of Bragg gratings is needed. The fast POFBG inscription can also open a route to simultaneous fabrication of the POF and Bragg grating sensors during the fibre drawing process.

6 Annealing and Etching Effects on Polymer Optical Fibre Bragg Grating Sensors

One of the objectives was to optimise the performance of polymer optical fibre Bragg grating (POFBG) sensors. The motivation of this work arose when the POFBG sensors used for liquid level monitoring described in chapter 7 were annealed for multiplexing purposes and they showed enhanced pressure sensitivity. In this chapter, thermal annealing and chemical etching were used to enhance the strain, stress, and force sensitivity of POFBG sensors. Strain sensitivity enhancement after annealing has been previously reported [37], but the influence of thermal annealing on stress sensitivity has not been investigated until now. Therefore, a comprehensive study has been conducted to investigate the annealing effects not only on strain, but also on the stress and force sensitivities of POFBG sensors.

6.1 Introduction

Fibre annealing was first used in order to shrink the fibre for POFBG sensor multiplexing purposes [35]. The polymer optical fibre (POF) physically shrinks in length when it is heated above its β-transition temperature, due to the relief of the residual internal stresses that were introduced during the fibre drawing process. The induced fibre shrinkage decreases the Bragg grating period

and consequently the Bragg wavelength permanently blue-shifts. Therefore, multiple Bragg grating inscriptions combined with different annealing rates allows for Bragg grating multiplexing by utilising only one phase mask.

Surprisingly, it was found later that POF annealing can be used for other purposes too. As mentioned in section 2.1.2, the polymers are viscoelastic materials, which means creep and hysteresis effects (strain and stress phase mismatch) are introduced during cyclic loading tests [15]. For this reason, POFBG sensors become less preferable in strain applications, even though having 14% higher strain sensitivity than silica sensors [18] and higher failure strain [15]. Thermal annealing appears as an intermediate solution that can be used to reduce the hysteresis effects on POFBG sensors [34]. Furthermore, the POFBG annealing can also enhance the strain [37] and humidity [38] sensitivity, and increase the useful operational range in temperature monitoring [179]. In addition, a recent publication shows that thermal annealing influences the photoelastic coefficient of POFs [63]. The work also indicates the effect of preform annealing on the stability of POF opto-mechanical characteristics.

In the literature it was reported that fibre etching can also influence the performance of POFBG sensors [180, 181]. Initially, etching was used to reduce the diameter of the fibre for particular purposes. The reduction of the cross-sectional area where the force is applied can stress the fibre to a higher degree and therefore offer enhanced force sensitivity to POF sensors (considering that the force is applied along the fibre axis) [180]. In addition, the reduction of the diameter of PMMA based POF improves the response time of the humidity detection sensor, because the distance between the Bragg grating located in the fibre core and the external environment becomes less [181]. Recently, it was demonstrated that chemical etching with acetone can also influence the Young modulus of the POF [182].

In this chapter, we investigate the effects of thermal annealing and chemical etching on the strain, stress and force sensitivities of POFBG sensors [67]. First, various POFBGs have been inscribed with a He-Cd laser in a single-mode poly(methyl methacrylate) (PMMA) optical fibre and their strain, stress and force sensitivities have been characterised. Then, the thermal annealing was performed by placing some sensors in a container filled with water that was heated above the β-transition temperature of PMMA. This represents the first report of a simple, well-controlled and cost-effective annealing process. After the annealing, the strain, stress and force sensitivity of each POFBG sensor was characterised again in order to be compared with the previous measurement. The results obtained show that the thermal annealing treatment can enhance not only the strain sensitivity as previously reported [37], but also the stress and force sensitivities. In the mean time, the chemical etching effects were also investigated by placing the non-annealed sensors in a container filled with acetone. Chemical etching POFBGs can dramatically enhance the force

sensitivity, as was expected due to the reduction of the cross-sectional area of the fibre. However, we show that the etching treatment can also influence the strain and stress sensitivities. The possible reasons for the changes in sensitivities are discussed in this chapter. To investigate if a further sensitivity improvement is possible, the annealed sensors were etched and the etched sensors were annealed. The results presented in this chapter show the benefits of annealing and etching on POFBG sensors when are used in strain, stress, force or pressure monitoring applications.

6.2 Experimental Details

6.2.1 Fabrication of Sensors

POFBGs were inscribed in a single-mode microstructured PMMA optical fibre (see POF 1 in Table 4.1). The POFBG inscriptions were made with the typical phase mask technique utilising a 325 nm continuous-wave He-Cd laser (Kimmon IK3301R-G), as illustrated in Figure 4.1. The periods of the phase masks that were used for the inscriptions are 558 nm and 580 nm. The inscribed gratings have Bragg wavelengths at 829 nm and 862 nm, respectively, considering that the effective refractive index of the PMMA in this wavelength region is approximately 1.49 (see equation 2.19). Both phase masks are 10 mm in width, which limits the maximum physical grating length that can be inscribed. In this work, POFBGs were produced with various lengths between 1.2 mm and 10 mm and their inscription time was between 1 and 17 minutes. However, the physical length defines only the strength of the grating's spectrum and it does not have any influence on the experimental results described in this chapter. A super-luminescent diode (Superlum SLD-371) and an optical spectrum analyser (HP 86142A) were used during the inscription process to monitor the spectrum changes of each POFBG. To monitor the reflected spectrum, a 50:50 single-mode silica coupler was utilised. After the inscription process, each POFBG has been placed into demountable FC/PC connectors to facilitate easier interrogation compared with the butt-coupling technique (see section 4.4).

6.2.2 Characterisation of Sensors

Strain sensitivity is defined as the Bragg wavelength shift $\Delta\lambda_B$ divided by the strain ε applied on the POF ($\Delta\lambda_B/\varepsilon$). For straining, each POF was placed between a fixed support and a translation stage, and it was held by fibre clamps (Thorlabs HFF01) as shown in Figure 6.1. Although these clamps have 125 μm V-grooves, they were designed for silica optical fibres and not for POF. Occasionally, the POF was slipping through the clamp during the straining process, especially in the cases in which its diameter was much less than 125 μm. To tackle this issue, a polymeric

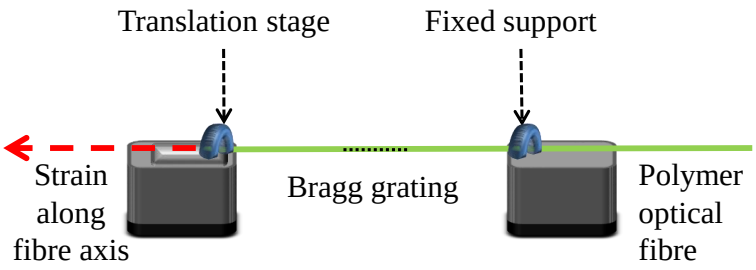

Figure 6.1: Setup for POF straining.

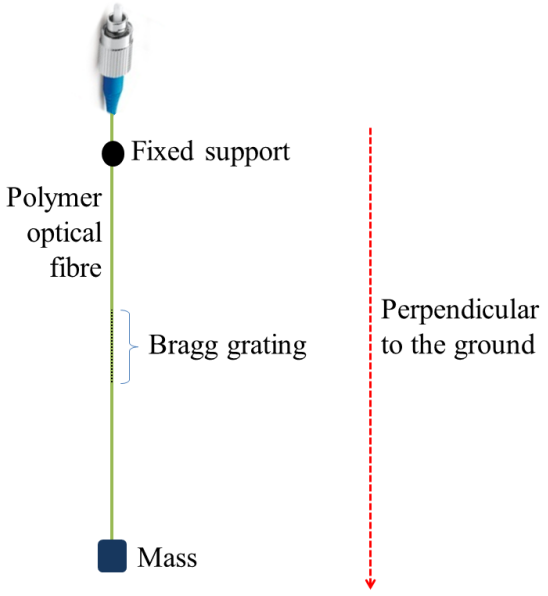

Figure 6.2: Setup for POF stressing.

material called polycaprolactone (PCL), which melts above 42 °C [183], was liquefied using a hot plate at 50°C and it was poured on the POF lying in the V-groove in order to enhance the clamp force on the POF's surface. In that way, the effective area where the force is applied from the clamp to the POF increases and the fibre slippage is avoided. Note that more than 5 minutes were allowed for the PCL to completely solidify and bond with the POF. In the next step, each POF was strained with the translation stage, which has accuracy of 1 μm. The fibre straining has been performed with steps up to 0.5%, which is well below the elastic limit of the material [184]. After the straining, the POF was removed from the clamps and the PCL material that was bonded to the fibre was removed by heating it up again with the hot plate. A few seconds at 50°C are enough for the PCL material to become liquid and be removed from the fibre. Note that only the POF part bonded with the PCL material was heated and not the area where the POFBG was located to avoid any unintended annealing effects.

The stress sensitivity is defined as the Bragg wavelength shift $\Delta\lambda_B$ divided by the stress σ

applied on the POF ($\Delta\lambda_B/\sigma$), and the force sensitivity F is expressed as $\Delta\lambda_B/F$. To stress the fibre, it was placed perpendicular to the ground, and masses with a known value (1-20 g) were successively added and by using the gravitational force the POF was stressed, as shown in Figure 6.2. The stress in this case is defined as

$$\sigma = \frac{F}{A} = \frac{mg}{\pi\left(\frac{d}{2}\right)^2}, \tag{6.1}$$

where F is the force applied on the fibre's cross-sectional area A. The gravitational force equals the gravitational acceleration of the Earth ($g = 9.8$ m/s^2) multiplied by the added mass m. The cross-sectional area can be calculated when the fibre diameter d at the POFBG location is measured with a microscope. The POF diameter increases after the annealing process because of the fibre shrinkage, and it decreases after the chemical etching. Therefore, measuring the fibre diameter before and after each process is essential. During the fibre straining and stressing, the time interval between the experimental steps was 1-3 minutes. This is to allow the Bragg wavelength shift occurring from the hysteresis effect to be stabilised and minimize the resulting readout error.

6.2.3 Thermal Annealing

The polymer chains in amorphous bulk materials (e.g. in PMMA) are mostly randomly oriented and entangled with each other. However, when POFs are produced from performs, the molecular chains can be stretched along the fibre axis by the drawing force. When the drawn POF leaves from the drawing oven, it is cooled down in the ambient room temperature, becomes solid again and the polymer chains become immobilized. The rapid fibre cooling prevents the molecular chains from returning to their amorphous state and as a result they maintain a degree of alignment along the fibre axis [185]. The stretched molecules introduce van der Waals forces between them, which are directly related with the degree of molecular chain alignment. The van der Waals forces can change the mechanical and thermal properties of the material [186]. It has been shown that the drawing conditions define the degree of the chain alignment, and consequently the mechanical properties of the POF, such as its Young modulus [64, 65]. To remove the residual stress from the stretched molecules, the material should receive adequate thermal energy to mobilise again its molecular chains in order to allow them to return to their amorphous state (considering there is not any external force acting on the POF) [187]. Above the β-transition temperature the backbone chain conformation can be reorganized and any residual internal stress can be removed from the material [188, 189]. However, the annealing temperature should be less than the glass transition phase, because otherwise the chain movements stop being localised, large sections of polymer

material become mobilised and any recorded POFBGs in the material can be erased [190, 191]. The prior thermal history of POF, the annealing conditions (temperature, humidity, duration, etc.), the degree of cross-linking, the material chemical composition, and polymerisation can influence the annealing rate of the POF and the degree of the molecular relaxation [38, 174, 192].

In this chapter, a thermal annealing process is utilised for the molecular relaxation of the PMMA optical fibre. The β-transition temperature of PMMA is 50°C [36] and its glass transition temperature is 105°C [56]. The authors who investigated the effects of thermal annealing on strain sensitivity of POFBG sensors in reference [37] compared the sensors inscribed in non-annealed POFs with the sensors inscribed in annealed POFs. However, the drawing conditions fluctuate (especially in custom-made POFs) as a result the mechanical properties of the polymer are not kept constant along the fibre length [64, 65]. Therefore, the mechanical sensitivity of the POFBG sensors could vary when they are inscribed in different positions along the fibre. To prevent this factor from influencing the results, the annealing process reported in this work was performed on the same sensors after their fabrication and initial characterisation.

Furthermore, the POF annealing processes reported until now have been generally performed for extended periods of time from several hours up to several days in climate-controlled chambers [34, 35, 37, 38, 179, 193]. In this thesis, a simpler, but well-controlled, and cost-effective process is demonstrated as shown in Figure 6.3. Each POF was placed for a few minutes (2-30 minutes) in a container filled with tap water that was heated up using a hot plate at 55±2 °C or 60±2 °C. A mercury thermometer (FISONS THL-290-050J) was used to monitor the annealing temperature. The cylindrical container has a 127 mm diameter and 22 mm height, and it is metallic to conduct heat from the hot plate. The reason for the annealing in hot water is to control the relative humidity (100%) during the process to make sure all the sensors were annealed with the same conditions. In addition, it has been demonstrated that the rate of the annealing process can be accelerated in an environment with higher humidity [174]. After the annealing, when the POF was removed from the container, it was kept for at least one hour at ambient room conditions (20-25 °C and 40-50% humidity) before its characterisation, in order to release the absorbed water obtained from the process.

6.2.4 Chemical Etching

As mentioned in the introduction of this chapter, there was a report that chemical etching (cladding removal) of PMMA with acetone can reduce its Young modulus [182]. The authors claimed that perhaps the cause of the Young modulus reduction is the molecular relaxation when the solvent is absorbed from the material. Moreover, the average stress distribution over the cross-sectional area of the POF may be changed if a material with a non-uniform stress distribution has been

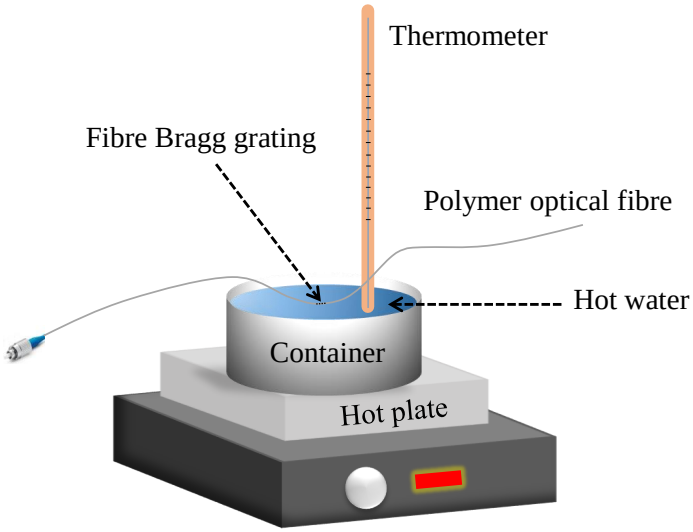

Figure 6.3: Setup for POF annealing.

etched [194]. The non-uniform stress distribution could be due to the drawing conditions [195–197], cooling rate [198], and prior thermal history of the fibre. Let us consider a homogeneous drawing process with the POF being heated up above the glass transition and all the molecules being stretched with the same degree. When the POF leaves the drawing oven and starts to cool down in the room temperature, the material on the outer layer of the fibre tends to cool faster than the inside material. In this case, there is a chance for the polymer chains located closer to the fibre core to move closer to their amorphous state before their immobilisation. Therefore, the residual stress in the inside region of the fibre could be less, creating a non-uniform stress distribution over the cross-sectional area of the POF [196]. In the experiments shown below, a study was made of the effects of chemical etching on the strain, stress, and force sensitivities of POFBG mechanical sensors. Reducing the cross-sectional area of the fibre, the force sensitivity is naturally expected to be increased. The chemical etching is performed by placing the POFs in a container filled with acetone for 4-7 minutes. After the process, there was a diameter reduction between 14% and 48%. Finally, the characterisation of the sensors was performed again to investigate the changes that occurred as a result of the etching process.

6.3 Results

The annealing conditions for each of the 9 sensors are listed in the Table 6.1. The strain, stress, and force sensitivities of each sensor before and after the thermal annealing treatment are listed in Table 6.2. The methodology used to calculate the sensitivities is as follows. To give an instance, Figure 6.4 shows the strain sensitivity of sensor 2 before and after being annealed. To

Table 6.1: Annealing duration and temperature for sensors 1-9.

Sensor	Annealing Duration (min)	Annealing Temperature (°C) ± 2
1	2	60
2	4	60
3	4	60
4	30	55
5	30	55
6	30	55
7	30	55
8	30	60
9	30	60

Table 6.2: Strain, stress, and force sensitivities before and after the thermal annealing.

Sensor	Strain Sensitivity (pm/με)		Stress Sensitivity (pm/kPa)		Force Sensitivity (pm/mN)		Young modulus (GPa)	
	Before	After	Before	After	Before	After	Before	After
1	0.681 ±0.009	0.739 ±0.019	0.141 ±0.018	0.217 ±0.022	10.92 ±1.37	13.65 ±1.37	4.83 ±0.62	3.41 ±0.36
2	0.708 ±0.007	0.902 ±0.016	0.180 ±0.023	0.260 ±0.025	10.92 ±1.37	14.33 ±1.37	3.93 ±0.50	3.47 ±0.34
3	0.541 ±0.019	0.694 ±0.012	0.147 ±0.019	0.201 ±0.021	10.92 ±1.37	13.65 ±1.37	3.68 ±0.49	3.45 ±0.37
4	0.711 ±0.007	0.879 ±0.020	0.163 ±0.026	0.191 ±0.018	12.24 ±1.96	14.37 ±1.34	4.36 ±0.70	4.60 ±0.45
5	0.726 ±0.007	0.875 ±0.020	0.176 ±0.009	0.208 ±0.011	11.44 ±0.59	13.26 ±0.62	4.13 ±0.21	4.21 ±0.24
6	0.728 ±0.004	0.889 ±0.033	0.182 ±0.006	0.220 ±0.011	11.87 ±0.39	14.10 ±0.62	4.00 ±0.13	4.04 ±0.25
7	0.690 ±0.011	0.883 ±0.011	0.191 ±0.016	0.221 ±0.020	12.00 ±0.98	13.87 ±1.23	3.61 ±0.31	4.00 ±0.36
8	0.727 ±0.011	0.849 ±0.011	0.197 ±0.023	0.258 ±0.023	13.56 ±1.54	17.88 ±1.54	3.69 ±0.43	3.29 ±0.30
9	0.771 ±0.011	0.943 ±0.011	0.173 ±0.024	0.202 ±0.026	13.41 ±1.85	14.64 ±1.85	4.46 ±0.62	4.67 ±0.60

calculate its strain sensitivity, the POF was strained in steps up to 0.5% of its original length as described previously. On each step, the Bragg wavelength position was measured 3-4 times (centroid method) in order to calculate its read-out error. The slope of the straight line shown in Figure 6.4 defines the strain sensitivity. The error of the sensitivity is defined by the error of

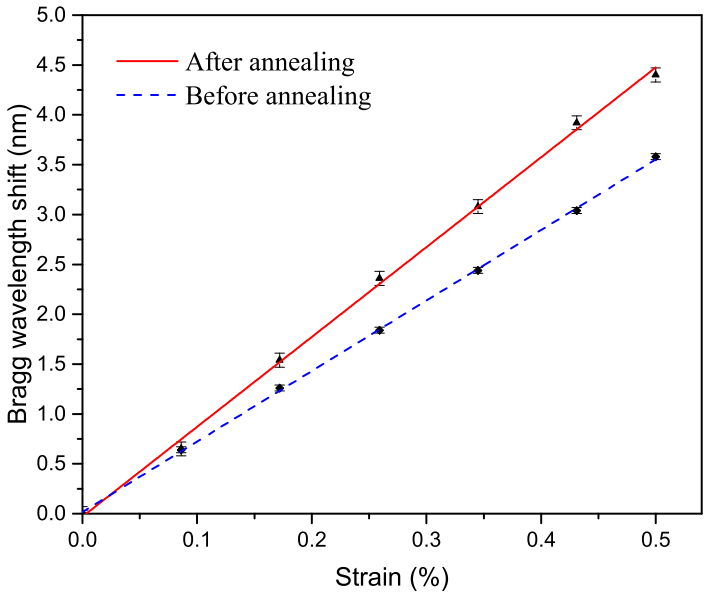

Figure 6.4: Strain sensitivity of sensor 2 before and after the thermal annealing.

the slope. Note that the fibre displacement error (which defines the strain error) can be ignored because the error of the translation stage is less than 0.5% during the applied displacement. The same methodology was used to calculate the other sensitivities. However, the force and stress errors were not negligible. Therefore, the error of the applied mass and the error of the measured fibre diameter were also considered during the data analysis.

As the results show in Table 6.2, all POFBG sensors experienced an enhancement of their strain, stress, and force sensitivities after their thermal treatment. The different annealing conditions do not clearly indicate any consistent influence on the results. A more comprehensive study is needed to investigate the effects of annealing conditions on the sensor's performance, but this is out of the scope of this work. The only observed effect is that the fibre annealing rate increases with the annealing temperature. The Bragg wavelength shift, which is directly related with the fibre shrinkage, can be tracked during the annealing process to study the annealing rate of the fibre (see Figure 6.5). Note that the initial blue-shift of the Bragg wavelength when the POF is submerged in the hot water is not shown in the Figure 6.5. The fibre shrinkage at 55±2 °C and 60±2 °C follows a first order and second order exponential decay respectively, illustrating the complex nature of the molecular relaxation. It was previously reported [174], that the POF annealing rate follows a dynamic exponential decay, depending on the POF prior thermal history and annealing conditions (temperature and humidity). In general, using higher annealing humidity and temperature, the POF shrinkage rate becomes greater and follows more stretched exponential decay [174].

The sensors 7, 8, and 9 were chemically etched after their thermal treatment by placing

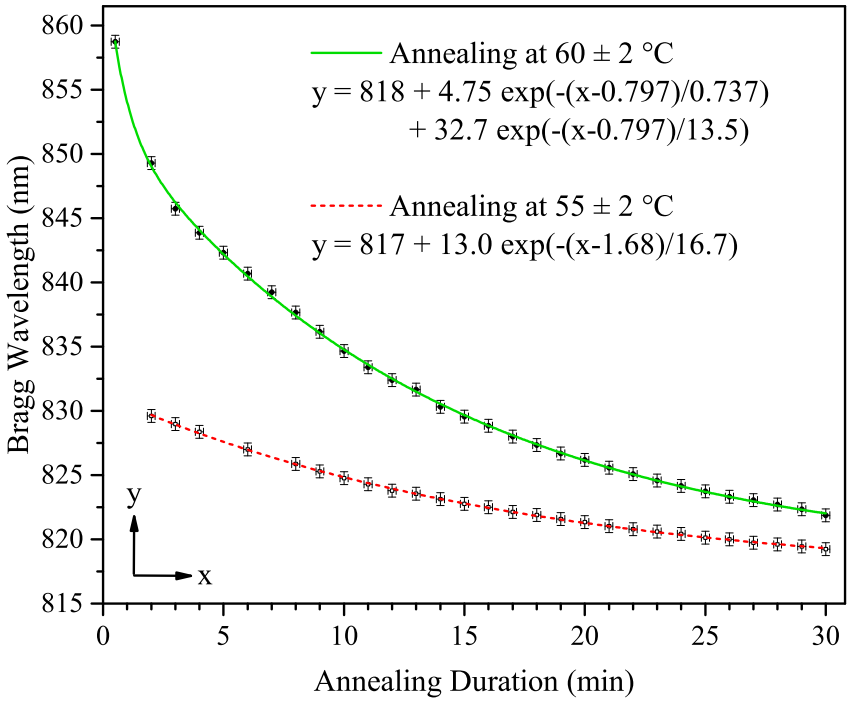

Figure 6.5: POF annealing rate at 55±2 °C and 60±2 °C.

Table 6.3: Etching duration and diameter reduction of sensors 7-9.

Sensor	Etching Duration (min)	Diameter before etching (μm)	Diameter after etching (μm)	Diameter reduction %
7	7	143	98	31
8	7	136	92	32
9	7	133	69	48

Table 6.4: Strain, stress, and force sensitivities before and after etching the annealed sensors.

Sensor	Strain Sensitivity (pm/με)		Stress Sensitivity (pm/kPa)		Force Sensitivity (pm/mN)	
	Before	After	Before	After	Before	After
7	0.883 ±0.011	0.854 ±0.022	0.221 ±0.020	0.259 ±0.020	13.87 ±1.23	34.05 ±2.63
8	0.849 ±0.011	0.755 ±0.012	0.258 ±0.023	0.260 ±0.011	17.88 ±1.54	39.53 ±1.60
9	0.943 ±0.011	0.848 ±0.012	0.202 ±0.026	0.241 ±0.006	14.64 ±1.85	64.97 ±1.75

Table 6.5: Etching duration and diameter reduction of sensors 10-18.

Sensor	Etching Duration (min)	Diameter before etching (μm)	Diameter after etching (μm)	Diameter reduction %
10	4	144	123	14
11	4.5	156	116	26
12	5	152	97	37
13	5	139	92	34
14	5.5	129	81	37
15	7	130	72	44
16	7	152	91	41
17	7	142	84	41
18	7	131	84	36

Table 6.6: Strain, stress, and force sensitivities before and after the chemical etching.

Sensor	Strain Sensitivity (pm/με)		Stress Sensitivity (pm/kPa)		Force Sensitivity (pm/mN)	
	Before	After	Before	After	Before	After
10	0.788 ±0.013	0.791 ±0.008	0.194 ±0.009	0.214 ±0.003	11.98 ±0.53	17.95 ±0.25
11	0.717 ±0.016	0.746 ±0.008	0.209 ±0.003	0.202 ±0.013	10.88 ±0.13	19.12 ±1.19
12	0.720 ±0.040	0.667 ±0.026	0.194 ±0.004	0.238 ±0.002	10.62 ±0.23	32.34 ±0.23
13	0.726 ±0.040	0.768 ±0.034	0.185 ±0.007	0.200 ±0.010	12.28 ±0.46	30.07 ±1.46
14	0.728 ±0.040	0.810 ±0.027	0.189 ±0.003	0.217 ±0.005	14.54 ±0.23	42.06 ±0.91
15	0.810 ±0.019	0.860 ±0.010	0.195 ±0.002	0.201 ±0.002	14.72 ±0.13	49.23 ±0.39
16	0.709 ±0.020	-	0.199 ±0.028	0.191 ±0.012	10.94 ±1.54	29.59 ±1.54
17	0.649 ±0.010	-	0.169 ±0.009	0.183 ±0.011	10.70 ±0.56	33.45 ±1.54
18	0.657 ±0.010	-	0.146 ±0.017	0.211 ±0.010	10.82 ±1.24	37.76 ±1.23

them in the acetone solvent for 7 minutes. Table 6.3 lists the diameter of the sensors and Table 6.4 lists their strain, stress, and force sensitivities before and after the etching process. The reduction of the diameter is mostly depended on the etching duration process and the acetone purity. The acetone solvent is contaminated when is used multiple times for POF etching and the

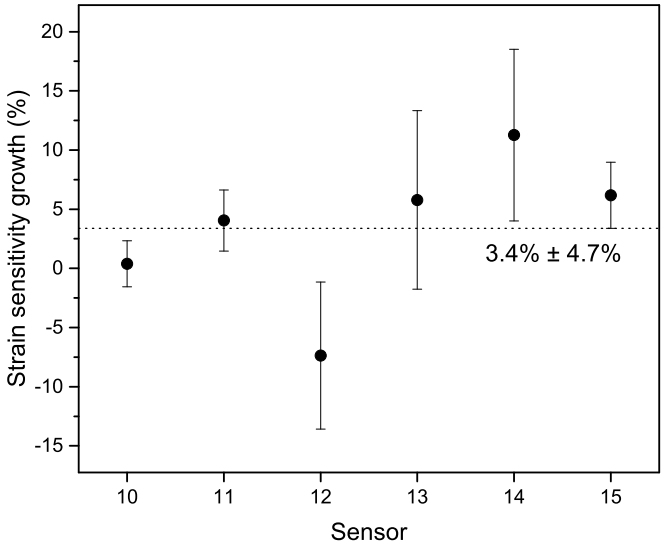

Figure 6.6: Average growth of strain sensitivity after etching.

etching rate can become slower. As a first impression, the strain sensitivity decreases and stress sensitivity increases in some degree after etching. On the other hand, the force sensitivity has been dramatically enhanced as it was expected due to the reduction of the fibre cross-sectional area. To further study the etching effects on the performance of the sensors, an additional 9 non-annealed POFBGs were characterised before and after the etching process. Table 6.5 lists the diameter of the sensors and Table 6.6 lists their strain, stress, and force sensitivities before and after the etching process. In this case, the results are inconsistent and a further analysis is needed. As shown in Figure 6.6, the average mean value of the strain sensitivity change after the etching process is 3.4%±4.7%. Figure 6.7 shows the stress sensitivity change occurring from etching and it has an average mean value of 11.6%±7.6%. Considering the errors associated in the average strain and stress sensitivity change, we cannot convincingly conclude whether the fibre etching enhances the strain and stress sensitivities of the sensors, and if there is such enhancement, it will be minimal. However, the results show that the fibre etching can dramatically enhance the force sensitivity in all sensors. In the last step, the sensors 16-18 have been annealed in water for 30 minutes at 55±2 °C after the etching process. The strain, stress, and force sensitivities were all dramatically improved after the etching and annealing process, as shown in Table 6.7. The strain and stress sensitivity enhancement of each sensor is due to the annealing process and its force sensitivity enhancement is mostly due to etching process.

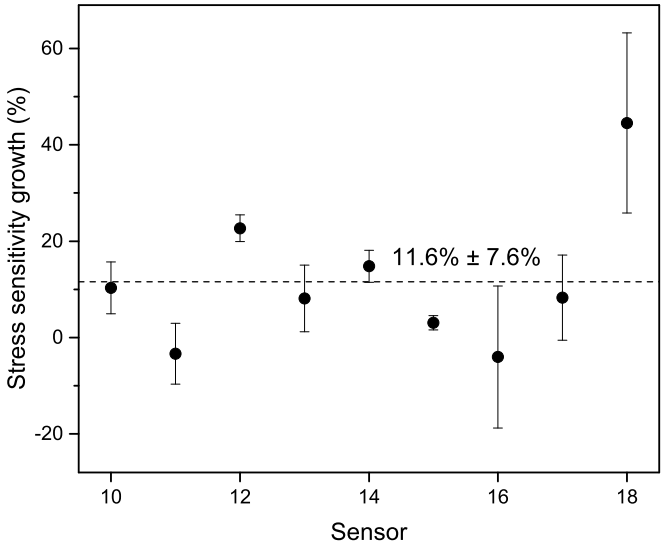

Figure 6.7: Average growth of stress sensitivity after etching.

Table 6.7: Strain, stress, and force sensitivities before and after both treatments

Sensor	Strain Sensitivity (pm/με)		Stress Sensitivity (pm/kPa)		Force Sensitivity (pm/mN)	
	Before	After	Before	After	Before	After
16	0.709 ±0.020	0.834 ±0.022	0.199 ±0.028	0.232 ±0.017	10.94 ±1.54	32.17 ±2.15
17	0.649 ±0.010	0.944 ±0.014	0.169 ±0.009	0.200 ±0.011	10.70 ±0.56	36.63 ±1.54
18	0.657 ±0.010	0.962 ±0.014	0.146 ±0.017	0.223 ±0.001	10.82 ±1.24	37.14 ±0.19

6.4 Conclusion

Both thermal annealing and chemical etching can influence the strain, stress, and force sensitivities of POFBG sensors. A simpler, well-controlled and cost-effective POF annealing process was also demonstrated. It was previously reported in the literature that the annealing can improve the strain sensitivity of the POFBG sensors. In this work, it is shown for the first time that the stress and force sensitivities can be also improved by POF annealing. The relaxation of the molecules, which occurs when the material is heated above its β-transition temperature, is perhaps the reason for the sensitivity enhancement. The influence of fibre etching on strain and stress sensitivities of POFBG sensors seems random and small. The introduced changes after the etching process are possibly due to the change of the non-uniform internal stress distribution caused by the diameter reduction. Despite that, the etching can be useful in applications used to detect force. Combining both POF

annealing and etching can be also proficient in some applications, e.g. humidity detection. The thermal treatment, which relaxes the molecules and renders the material more amorphous, can increase the water absorption rate in the POF. On the other hand, the POF etching (cladding removal) decreases the distance between the external environment and the POFBG location. Therefore, combining both annealing and etching treatments can improve the response time of the humidity POFBG sensor.

7 Applications of Polymer Optical Fibre Bragg Grating Sensors

This chapter describes my contribution in the development of three different applications: ultrasound detection, liquid level monitoring, and erythrocyte concentration measurement. My role was to fabricate the polymer optical fibre Bragg grating (POFBG) sensors, connectorise them, and where needed to perform POFBG sensor multiplexing. The 325 nm He-Cd laser system and the phase mask technique were used to produce the POFBG sensors, as described in chapter 4. Then, the sensors were distributed to 'TRIPOD' partners and other researchers in order to develop novel applications based on POFBGs.

7.1 Ultrasound Detection

POFBG sensors were fabricated in POF 1 (see Table 4.1) and connectorised by me and delivered to our partners in Universidad Carlos III de Madrid, who performed ultrasound detection tests. These sensors can be used in ultrasonic endoscopic applications in the biomedical sector [22]. The most widely used method to detect ultrasonic waves is with piezo electric transducers. However, transducers are susceptible to electromagnetic interference, have limited bandwidth and their sensitivity is inversely proportional to their size. The fibre based sensors on the other hand

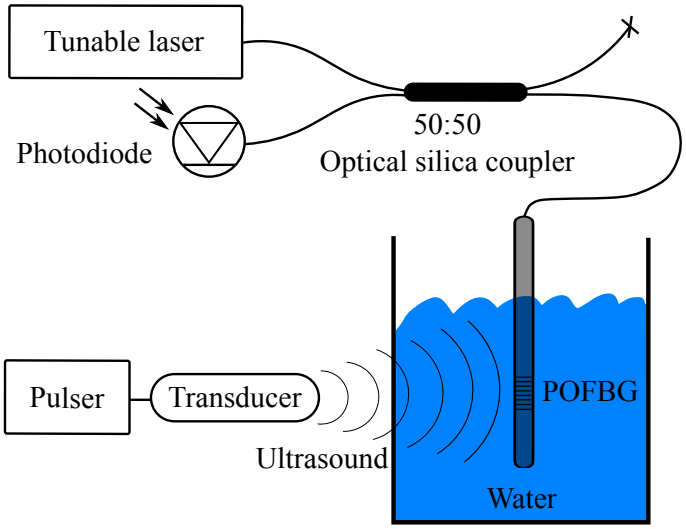

Figure 7.1: Ultrasound detection scheme.

have immunity to electromagnetic interference and high sensitivity (especially the interferometric devices). The fibre based sensors can be also integrated into an endoscope of less than 1 mm in diameter, without their sensitivity being affected by the decreased size. Furthermore, the motivation of using POF instead of SOF based sensors is because the POF has lower Young modulus and acoustic impedance, which provide higher acoustic sensitivity. To detect ultrasonic waves, numerous laser pulses can be sent to a tissue. The targeted tissue absorbs the energy from each laser pulse causing a transient thermoelastic expansion. This rapid expansion pushes all the particles around the expanding medium and generates a pressure wave in the ultrasonic frequency range. Usually, the time delay of the ultrasonic wave determines the distance of the targeted tissue and its amplitude determines the absorbance coefficient of the tissue. For example, tumors can preferentially absorb more light than normal tissue and the amplitude of the ultrasonic wave can be higher. A 2D and 3D opto-acoustic imaging can be constructed with some signal processing when multiple scans are performed around the tissue. The typical opto-acoustic spectrum ranges from 100 kHz to 50 MHz [199].

The experimental setup that our partner used for the ultrasound detection is shown in Figure 7.1. The POF was placed in a container filled with water, which acts as a transmitted medium for the ultrasonic wave. A tunable laser was connected with a fibre coupler, which had at the output the POFBG sensor. The amplitude of reflected light from the grating structure could be read with a photodiode which was connected with an oscilloscope. The tunable laser was tuned at the steepest slope of the POFBG reflected spectrum. Therefore, any Bragg wavelength shift due to ultrasonic wave pressure could change the amplitude of the reflected light arriving at the photodiode. The voltage of the photodiode changes according with the Bragg wavelength

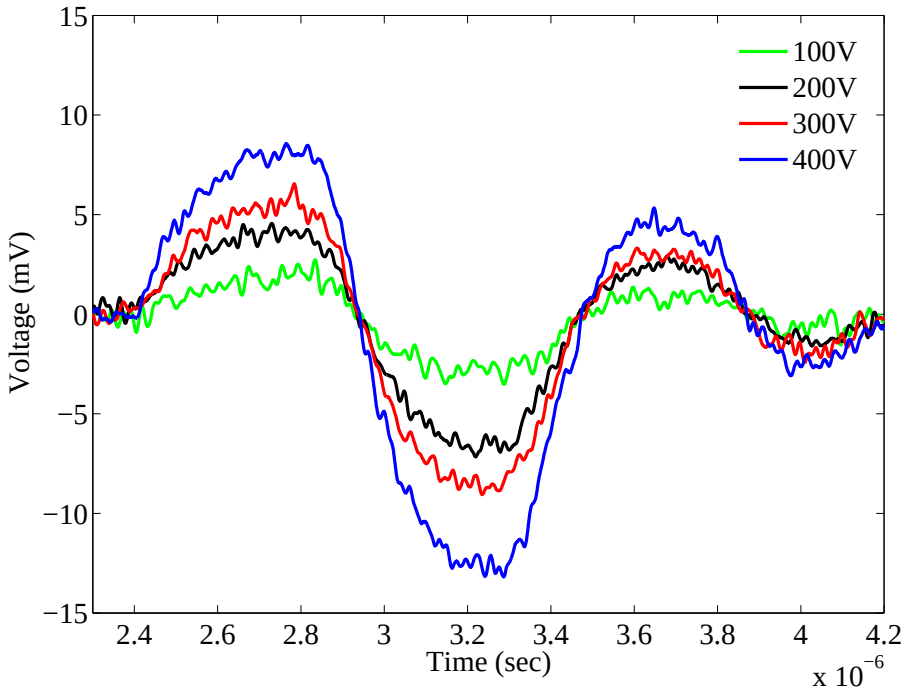

Figure 7.2: Ultrasonic response for 1 MHz at excitation voltages between 100 V and 400 V.

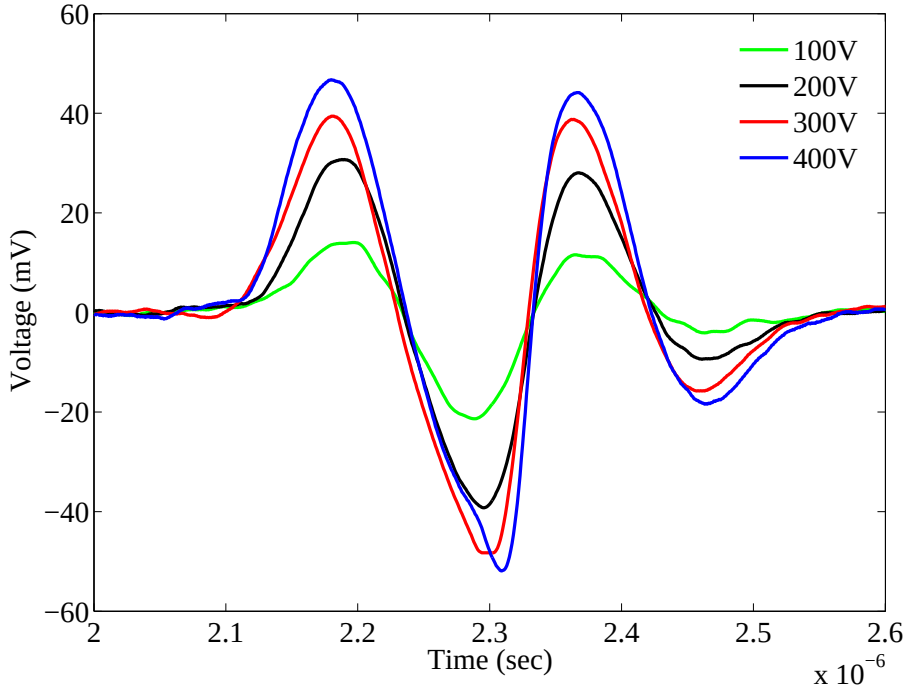

Figure 7.3: Ultrasonic response for 5 MHz at excitation voltages between 100 V and 400 V.

shift that occurs from the pressure of the acoustic wave. The photodetector is connected with an oscilloscope in order to observe the periodic change of voltage with time. The period of the observed voltage determines the period of the acoustic wave. Figure 7.2 shows the ultrasonic

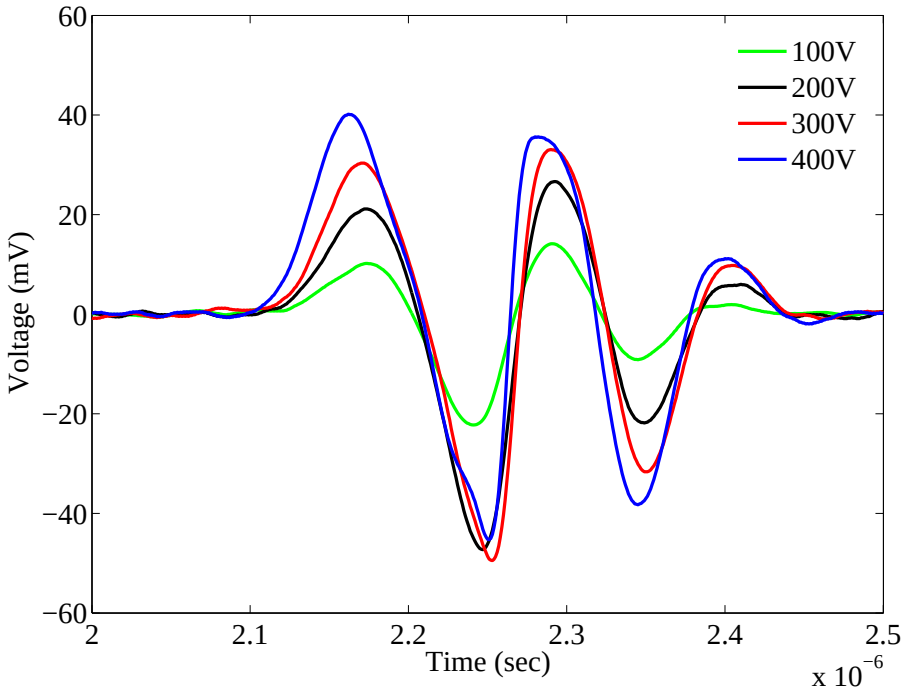

Figure 7.4: Ultrasonic response for 10 MHz at excitation voltages between 100 V and 400 V.

response for 1 MHz in the time domain. Different excitation voltage was used for the transducer: 100 V, 200 V, 300 V, and 400 V. As the transducer excitation voltage increases, the ultrasonic pressure becomes higher and the Bragg wavelength shift is larger. Figure 7.3 and Figure 7.4 show the ultrasonic response for 5 MHz and 10 MHz, respectively. These plots show that the frequency of the voltage change is directly related with the frequency of the ultrasonic wave. The ultrasonic wave pressure of the 1 MHz transducer is weak and approaches the noise level of the photodiode. Higher voltage excitation levels (especially 300 V and 400 V) of the transducer leads to higher pressure waves and larger Bragg wavelength shifts. Therefore, the photodiode voltage changes are more easily detectable when using higher voltage excitation.

In conclusion, the first ultrasound measurements obtained using a PMMA based POFBG are presented. This compact in-fibre sensor has an immunity to electromagnetic interference and it can be integrated into an endoscope of less than 1 mm in diameter, without its sensitivity being affected by the decreased size. The sensor showed the ability to detect ultrasonic frequencies of 1 MHz, 5 MHz, and 10 MHz, which lie in the spectrum range used for 2D and 3D opto-acoustic imaging.

7.2 Liquid Level Monitoring

My role for this application was to fabricate, connectorise and multiplex the POFBG sensors. The sensors were inscribed in POF 1 (see Table 4.1). Thereafter, this array of sensors was been used by C. A. F. Marques to develop a liquid level monitoring system [21]. In general, the liquid level monitoring system can be applied to water supplies, flood warning, and aviation fuel systems to name a few. The most widely used monitoring sensors are based on electrical and mechanical systems. However, their applications cannot be extended to explosive environments due to safety concerns, reliability and maintainability issues. On the other hand, the fibre-based sensors are safer and they offer an alternative method for liquid level monitoring. Several systems based on fibre Bragg gratings were reported [200–205], but they had various issues such as high production cost and complexity, fibre contamination by the liquid, low sensitivity, instability, limited resolution, and limited pressure range. In this work, an alternative technique was used to tackle these issues by utilizing an array of 5 multiplexed POFBG sensors. In addition, the liquid level monitoring system reported in this work shows characteristics that are advantageous in aviation fuel gauging. The sensors were inscribed in 75 cm long POF and they were spatially separated by 15 cm. The POFBGs were inscribed in the POF 1 (see Table 4.1) and they have Bragg wavelengths in the 830 nm wavelength region, where the PMMA material exhibits less optical attenuation compared with the longer wavelengths [31]. There were only two phase masks available for this wavelength region (with 558 nm and 580 nm pitch), producing Bragg wavelengths at 829 nm and 862 nm, respectively. However, the broadband light source is centred at 830 nm and the 862 nm POFBG appears weaker. Therefore, four from the five POFBGs were annealed with the same method described in section 4.5 to permanently blue-shift their Bragg wavelengths. The 829 nm POFBG shown in Figure 7.5 was the only one which was not annealed. Figure 7.5 (a) shows the transmitted spectrum of the POFBG array sensors and Figure 7.5 (b) shows their reflected spectrum.

After the connectorisation process, each sensor was embedded in a silicone rubber diaphragm by C. A. F. Marques. First, the 'SILASTIC T-4 Base' and 'SILASTIC T-4 Catalyst' liquids obtained from 'DowCorning Corporation' were homogeneously mixed in a ratio of 100:10 to compose the silicone solution. To remove any air bubbles from the solution, it was placed in a vacuum chamber. Then, the solution was poured in a container with 1.1 mm height and 50 mm diameter and a POFBG was placed at the center of the container. The mold was left 24 hours in ambient room conditions to set. The process was repeated for all the POFBG sensors. All the diaphragms had thickness of 1.080 ± 0.005 mm. Then, a square tube, which has 800 mm height, 38.1 mm external side length, and 3.2 mm wall thickness, was used to mount the 750 mm POFBG array sensors. Then, 5 circular holes were drilled on the tube at equal distance of 150 mm. The

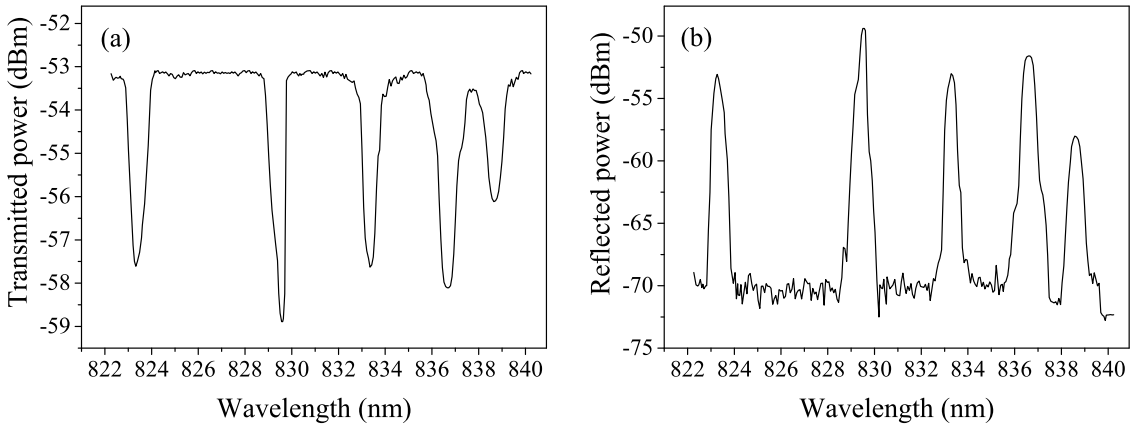

Figure 7.5: Spectrum of POFBG array sensors measured in (a) transmission, and (b) reflection.

diameter of each hole was 15 mm, so the diameter of each diaphragm (which was 50 mm) had to be reduced by cutting the excess silicone rubber in order to fit it into the hole. Silicone sealant was placed around each diaphragm to fix it in position. Note that each POFBG sensor was located at the centre of the hole. After the assembly of the square tube with the POFBG array sensors, the tube was placed in a cylindrical container of 800 mm height and 94 mm inner diameter, as shown in Figure 7.6. The sensors were monitored in reflection utilising a broadband light source (Thorlabs ASE-FL7002-C4), an optical coupler, and an optical spectrum analyser (HP 86142A).

The container is open at the top so that the atmospheric pressure inside it was relatively constant. The operation principle of the sensing system relies on the increasing hydrostatic pressure that deforms the diaphragms and the POFBGs; as a result the Bragg wavelength red-shifts. All the sensors above the liquid surface show the same ambient pressure, and the sensors below the liquid surface show higher pressure that increases linearly with depth. One method to determine the level of the liquid is by identifying the position of the liquid surface, which lies between the sensor that shows higher than ambient pressure and the sensor with the ambient value. However, the precision of this approach is low and multiple POFBG point sensors close to each other are required to increase the resolution of the system. A better approach is to apply a linear regression analysis to the pressure reading from the sensors located under the liquid surface, as shown in Figure 7.6. The intercept value obtained from the linear equation indicates the location of the liquid surface. Using the linear regression method, any malfunctioning sensors can be detected and ignored, and any temperature changes on the whole system can be also compensated. In addition, the operation of the system is independent of liquid density and insensitive to g-force (in the case of aviation fuel monitoring), because these parameters alter the slope of the fitted regression line and not its intercept.

Initially, the performance of the device was characterised using water as liquid, which has a

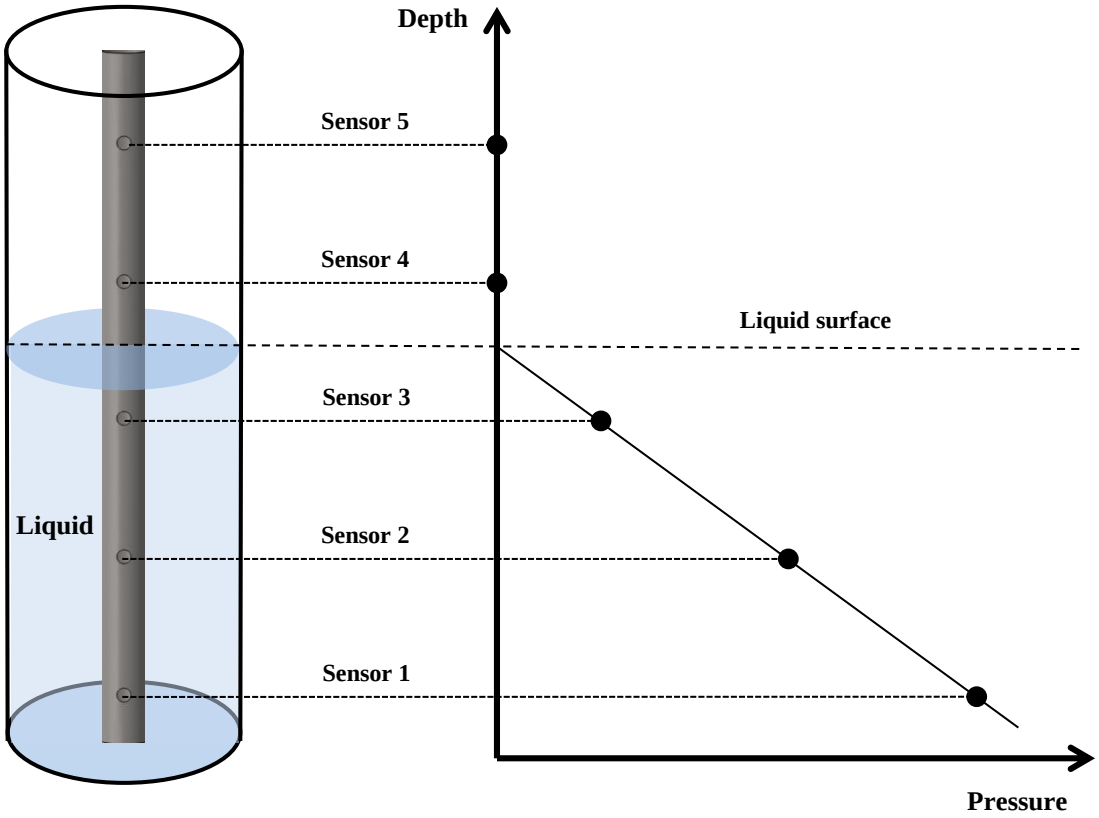

Figure 7.6: Liquid level monitoring approach using an array of sensors. On the left is the location of the sensors in the container and on the right is the liquid level determination by applying a linear regression to the submerged sensors reading.

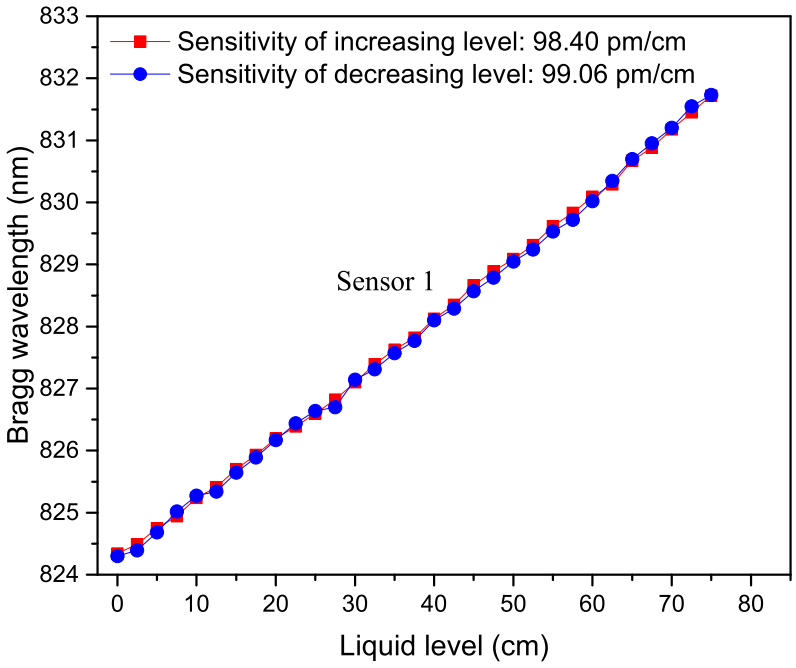

Figure 7.7: Bragg wavelength shift of sensor 1 due to change of water level.

density of 0.999 kg/L at 15 °C. The liquid level was changed with steps of 2.5 cm by filling the container with water in the range of 0 to 75 cm. A time interval of 5 minutes between the steps was maintained to assure the stability of the system. The increasing and decreasing level of liquid was repeated 3 times to investigate the repeatability of the sensor system. For illustration, Figure 7.7 shows the Bragg wavelength shift of sensor 1 due to change of water level. The slope defines the sensitivity of the sensor. Table 7.1 lists the water level sensitivities for all sensors. Surprisingly, sensor 5 shows less sensitivity compared than the other sensors. Realising that sensor 5 is the only sensor that has not been annealed, additional investigation was conducted for this matter [67]. This observation was the motivation of the work described in chapter 6, which comprehensively shows the effects of annealing on POFBG sensors. The results show that fibre annealing can enhance the strain, stress and force sensitivity of POFBG sensors. One example of the annealing effects on a POFBG sensor is shown in the Table 7.2. The force sensitivity, which is directly related with the pressure sensitivity, enhances after the fibre annealing.

In the next experiment, three additional POFBGs were inscribed in another POF (see POF 1 in Table 4.1) and they were embedded 5 cm, 20 cm and 35 cm from the bottom of the container. The liquid used for this experiment is the JET A-1 aviation fuel, which has a density of 0.810 kg/L at 15 °C. The fuel level was varied between 35 cm and 75 cm with steps of 5 cm. Due to the lower density of fuel compared with water, the sensitivities in this case were expected to be 20% lower. However, the results listed in Table 7.3 show similar sensitivity values. A possible reason could be the usage of a different silicone sealant to fix the diaphragm to the fuel container. To test the accuracy of the sensor, the fuel level was set at 48.0$\pm$0.1 cm. Applying linear regression to the reading from the 3 POFBGs, the fuel level can be determined by computing the intercept value. Figure 7.8 shows the equation that describes the linear fit of the readings and the fuel level is defined to be 46.3$\pm$1.1 cm.

Despite the promising results obtained above, the 'SILASTIC' material used to form the diaphragms absorbed the Jet A-1 fuel, and as a result it swelled. Thereafter, a more suitable material called polyurethane resin from 'Liquid Lens' was obtained to develop new diaphragms. The MF633 resin and the DK780 catalyst were mixed in a ratio of 1:1 by volume and the newly formed material was cured at room conditions (23 °C, 40% RH) for 8 hours. Then, the material was placed in Jet A-1 fuel for more than 3 months to test it and no swelling has been observed. The new material proved to be resistant to the fuel, but has less flexibility. In the next stage, an additional 3 POFBGs were embedded in polyurethane diaphragms with the same method described above. To measure the sensitivities, the fuel level was varied between 0 cm and 75 cm with steps of 5 cm. The results are listed in Table 7.4, and it is clear that the sensitivities are much lower in this case because the stiffness of the diaphragms is higher; i.e. the liquid pressure deforms the diaphragm

Table 7.1: Water level sensitivities.

		Increasing level (pm/cm)	Decreasing level (pm/cm)
Sensor 1	Cycle 1	98.4±0.3	99.1±0.4
	Cycle 2	98.7±0.2	98.9±0.5
	Cycle 3	98.5±0.4	98.6±0.2
Sensor 2	Cycle 1	98.1±0.2	98.3±0.4
	Cycle 2	98.4±0.2	98.5±0.3
	Cycle 3	98.7±0.4	98.2±0.6
Sensor 3	Cycle 1	98.2±0.6	98.7±0.5
	Cycle 2	98.7±0.3	99.2±0.6
	Cycle 3	98.9±0.4	98.8±0.3
Sensor 4	Cycle 1	97.4±0.8	97.8±0.7
	Cycle 2	98.2±0.9	97.9±1.0
	Cycle 3	97.9±0.6	98.6±0.8
Sensor 5	Cycle 1	86.1±2.5	86.2±2.7
	Cycle 2	86.4±2.3	86.0±2.2
	Cycle 3	86.5±2.1	86.1±2.4

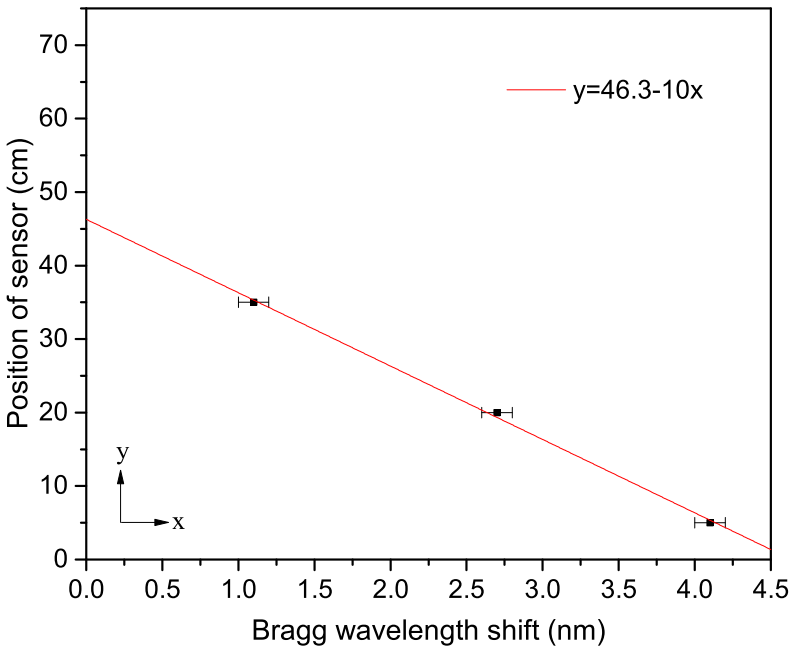

Figure 7.8: Determination of fuel level using linear regression.

Table 7.2: Strain, stress and force sensitivity before and after annealing.

	Before annealing	After annealing
Strain sensitivity (pm/με)	0.681±0.009	0.739±0.019
Stress sensitivity (pm/kPa)	0.141±0.018	0.217±0.022
Force sensitivity (pm/μN)	0.109±0.001	0.137±0.001

Table 7.3: Fuel level sensitivities.

		Increasing level (pm/cm)	Decreasing level (pm/cm)
Sensor 1	Cycle 1	96.7±0.3	96.9±0.4
	Cycle 2	96.1±0.2	97.0±0.3
Sensor 2	Cycle 1	97.4±0.2	97.3±0.4
	Cycle 2	96.9±0.2	96.6±0.3
Sensor 3	Cycle 1	97.8±0.6	98.8±0.5
	Cycle 2	96.6±0.7	97.9±0.6

Table 7.4: Fuel level sensitivities with polyurethane material.

		Increasing level (pm/cm)	Decreasing level (pm/cm)
Sensor 1	Cycle 1	38.4±0.5	38.7±0.4
	Cycle 2	38.7±0.2	38.5±0.3
	Cycle 3	38.5±0.4	38.6±0.2
Sensor 2	Cycle 1	38.4±0.4	38.7±0.6
	Cycle 2	38.2±0.4	37.4±0.3
	Cycle 3	37.5±0.2	38.6±0.4
Sensor 3	Cycle 1	38.8±0.2	39.5±0.4
	Cycle 2	38.4±0.5	38.6±0.4
	Cycle 3	38.5±0.3	38.3±0.4

to a lesser degree. To test again the accuracy of the system, the fuel level was set at 48.0±0.1 cm. Then, the linear regression was applied to the readings of the sensors. Figure 7.9 shows the linear fit with the intercept value being 47.5±1.5 cm.

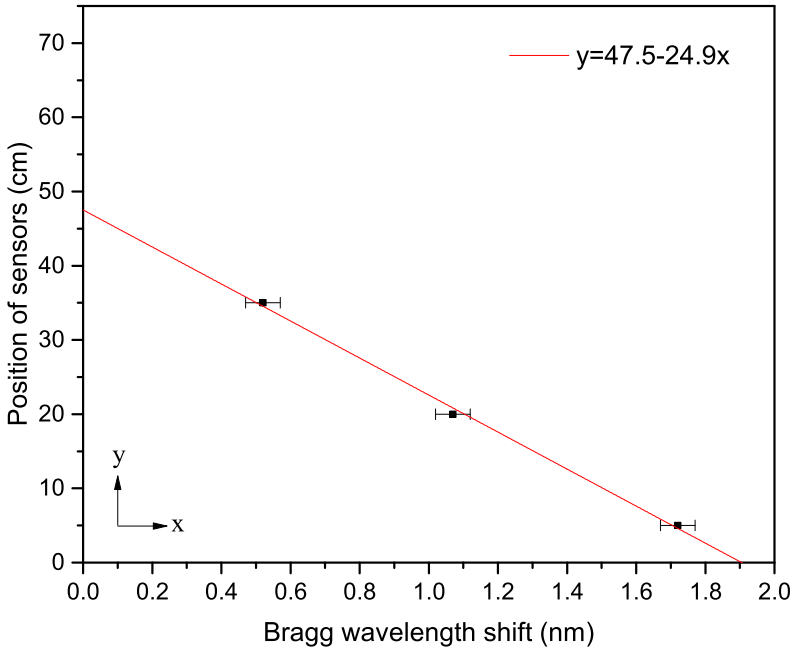

Figure 7.9: Determination of fuel level using linear regression with the new material.

In conclusion, a liquid level monitoring system based on POFBG array sensors has been developed for the first time. The sensors were embedded in silicone rubber diaphragms to make them sensitive to pressure and protect them from the liquid. The performance of the system has been characterised and it shows high liquid level sensitivity with linear and repeatable response. The system reported in this work exhibits 4 times higher sensitivity (98 pm/cm) compared with the reported silica based liquid level monitoring system (23 pm/cm) [205]. This system was also tested with JET A-1 aviation fuel and a suitable material (polyurethane) was employed to avoid the swelling. The work reported here can find application in aviation fuel level monitoring.

7.3 Erythrocyte Concentration Measurement

My contribution for this application was the inscription of Bragg grating sensors in undoped microstructured POFs (see POF 14 in Table 4.1). Then, the sensors were coated with graphene by B. C. Yao, et al., who used them to detect the concentration of human erythrocytes (red blood cells) [206]. The erythrocytes are essential for the survival of a person, since they are responsible for transferring oxygen around the body. The volume percentage of erythrocytes in blood (called hematocrit) defines their capability to effectively deliver the oxygen. The normal hematocrit for men is approximately 45% and for women 40% [207]. Some life-threatening diseases and disorders can also change the hematocrit levels, such as the anemia or the polycythemia [208]. Usually, the hematocrit is not directly measured; it is calculated by an automated analyser, which multiplies the number of red blood cells by the mean cell volume. The most common method

is to perform an electrical analysis, in which the impedance of blood solution can be determined (Coulter principle). Then, the erythrocytes are destructed by adding a lytic reagent to the blood solution, and the impedance is measured again. This allows the counts of erythrocytes to be obtained, and the hematocrit to be calculated. The hematocrit levels can be also measured with optical methods, i.e. with spectrophotometry [209].

In this work, an optical method to measure directly and effectively the concentration of erythrocytes in a blood solution is presented. POFBGs coated with graphene were used for the erythrocyte detection. The reason for using graphene is because the conductivity and the permittivity of graphene dramatically change when it absorbs external molecules [210]. Therefore, coating the POFBGs with graphene enable them to be used as biochemical sensors.

The methodology that was used to develop the biochemical sensor is as follows. A D-shaped POF was first produced by polishing it 50 μm in depth and 8 mm in length at the position of the POFBG. A p-doped monolayer graphene was created by a chemical vapour deposition process on a copper foil and then it was transferred onto a PMMA film. This PMMA/graphene film has been placed on the polished area of the fiber as described in reference [211]. The thicknesses of the PMMA and graphene films are approximately 50 nm and 0.4 nm respectively. Simulating the power confinement for fundamental mode in COMSOL software, it is shown that the percentage of the power outside the D-shaped fibre is 0.3% in the case of POF and 0.1% in the case of SOF, which is the reason why POF has been chosen for this application. Adding a graphene film, the fractional power outside the D-shaped POF became 4.7%, indicating that the graphene assists the fundamental mode to interact with the environment, because graphene influences the penetration of the core mode electric field into the cladding region. When the measurand is absorbed by the film, the permittivity of the graphene is modified and the effective refractive index of the POF is changed causing a Bragg wavelength shift. Four different samples were used to measure the erythrocyte concentration. The first sample was pure saline without any erythrocyte concertation (0 ppm). Then fresh human blood (O-type) was diluted 10^4, 10^3, and 10^2 times. So, the other three samples had 10^2 ppm, 10^3 ppm, and 10^4 ppm concentration, respectively. The refractive index of each sample is listed in Table 7.5.

To detect the erythrocytes, a fibre based microfluidic system has been built, as shown schematically in Figure 7.10. Each erythrocyte-saline solution was injected with a syringe in the microfluidic tube, which had a volume of 0.3 mL. The tunable laser (Agilent 81960A) was used as a light source, which was amplified by an erbium-doped fibre amplifier. The light reaches the POFBG location and reflects back to the optical spectrum analyser (Agilent N744A) via the optical coupler (see Figure 7.10). The results are listed in Table 7.6. The POFBG sensor without graphene coating shows less sensitivity compared with the sensor that is coated with graphene.

Table 7.5: Samples with different erythrocyte concentrations.

Sample	Erythrocyte concentration (ppm)	Refractive index
1	0	1.3340
2	10^2	1.3343
3	10^3	1.3350
4	10^4	1.3370

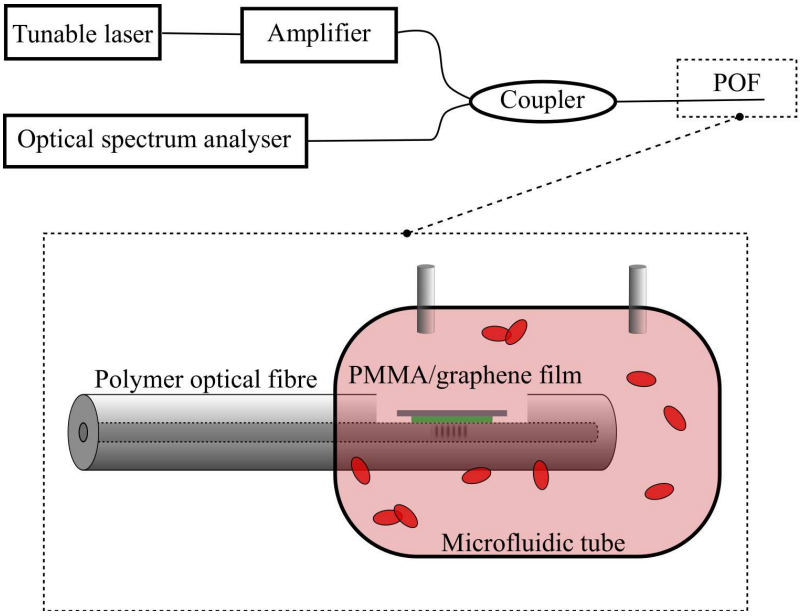

Figure 7.10: POF based microfluidic system for erythrocyte concentration detection.

Table 7.6: Bragg wavelength shift corresponding to erythrocyte concentration.

Sample	Erythrocyte concentration (ppm)	Wavelength shift without graphene (nm)	Wavelength shift with graphene (nm)
1	0	0	0
2	10^2	0.01	0.14
3	10^3	0.16	0.58
4	10^4	0.21	2.03

The latter exhibits a Bragg wavelength shift of 2.03 nm when the erythrocyte concentration is 104 ppm. This means a sensitivity of 0.20 pm/ppm.

In conclusion, a novel fibre-optic sensor for direct measurement of red blood cell (erythrocyte) concentration is demonstrated. The POFBG sensor was photo-inscribed in an undoped PMMA based microstructured optical fibre. The POF was polished to a D-shape and a graphene layer was attached close to the fibre core, where the POFBG is located. The graphene layer enhances the interaction of the electric field of the fibre with the ambient environment. Results show that the POFBG sensor that is coated with graphene exhibits higher sensitivity compared with the sensor without graphene. The POFBG sensor presented in this work is biocompatible, small in size, and offers a state-of-the-art fibre-optic sensing platform for in-situ and in-vivo red blood cell detection applications. Presumably this approach lacks specificity in that it will respond to other biological/biochemical species too.

8 Volume Bragg Grating Inscription and Characterisation

In this chapter, Bragg grating structures have been recorded in a bulk poly(methyl methacrylate) (PMMA) material utilising the He-Cd laser system. The pure PMMA bulk materials have been produced by our partners in Maria Curie-Skłodowska University. The objective was to investigate the possibility to record volume Bragg grating (VBG) devices effectively and repeatable. In general, the diffraction efficiency of the VBG is directly related with the introduced refractive index change in the material. Therefore, this work can be used in the future to record VBG devices in novel polymeric materials and assess their photosensitivity to specific irradiation conditions. In the first experiments, the VBGs were inscribed with the phase mask technique, but unexpectedly multiple VBG structures were observed on each inscription. After some time, it was realised that the extra VBGs were produced due to the additional phase mask diffraction orders (0 and ± 2 orders). The analysis confirming this assumption is presented in this chapter. After the realisation of this issue, a new inscription setup was developed, which was used to produce VBGs with the holographic technique (see Figure 2.10). In this case, only one VBG structure was produced after each inscription process.

The final objective was to inscribe a VBG with the shortest possible period. This work can

be used in the future to investigate the effects of the long polymer chains on the spatial resolution of the refractive index modulation. It is expected that as the grating period becomes shorter, the modulation of refractive index becomes less due to the spatial recording resolution limit, which results from the existence of the long polymer molecules.

In summary, this chapter demonstrates the inscription and characterisation of various VBG structures, with the phase mask and holographic method. The two fabrication techniques are comprehensively compared, discussed and analysed. At the end of the chapter, the shortest grating period reported in PMMA materials is presented. The work described in this chapter can be continued in the future to perform photosensitivity studies of some polymeric materials and investigate the spatial recording resolution limit of Bragg grating devices.

8.1 Introduction

Grating structures can be divided in two types: optically thin (Raman-Nath) diffraction gratings (two-dimensional structures) and optically thick (Bragg) gratings (three-dimensional structures), as illustrated in Figure 8.1. In the case of optically thin gratings, the incident wave is split into a number of waves (known as diffraction orders), which travel in different directions, as shown in Figure 8.1 (a). The diffraction angles depend on the wavelength of the incident light and the grating period. These types of gratings are considered unselective. The multiple diffraction orders can be reduced to one by introducing an inherent selectivity. This can be done by increasing the thickness of the grating; the input wave is forced to cross many fringes (scatter points) before emerging and as a result a constructive interference occurs only at the Bragg angle, as shown in Figure 8.1 (b).

The Bragg grating recorded in a bulk material is called volume Bragg grating (VBG) or hologram. It has a thick periodic structure and it can be recorded inside some transparent materials usually by exposing the material to a laser interference pattern. The main characteristics of a VBG are the selectivity and the potentially high diffraction efficiency. Diffraction efficiencies more than 99% have been reported in silica bulk materials [212]. VBGs have small reflection bandwidth (e.g. typically less than 0.1 nm) and they can be used in laser diodes [213] as output couplers in order to provide narrow emission bandwidth for the laser. In addition, VBGs can be placed into the resonator of a solid-state-laser to tune or stabilise its emission wavelength [214]. For relatively low intracavity powers, VBGs can also be used in spectral beam combining [215].

The original object wave of VBG can be reconstructed after the recording process. If the replay wavelength is the same as the recorded wavelength, the diffraction Bragg angle remains the same. The reconstruction can be used to measure the diffraction efficiency of the recorded

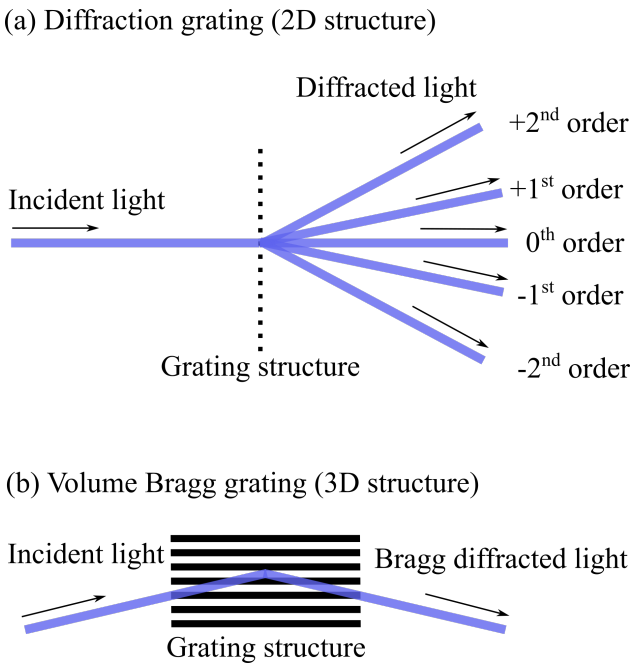

Figure 8.1: Types of gratings: (a) Diffraction grating (2D structure) and (b) Volume Bragg grating (3D structure).

grating, and consequently calculate the maximum change of refractive index introduced in the material. In this chapter, PMMA based VBG inscription and characterisation is presented, which can be continued in the future to define the photosensitivity of some novel polymeric materials and investigate the spatial recording resolution limit of Bragg grating devices. Initially, the VBG inscription was performed with the phase mask technique, however it was proved to be an unsuitable method as more than one VBGs were observed during the reconstruction process. This phenomenon was comprehensively studied and the results are presented in this chapter. A different inscription system was used to produce additional VBGs at a later stage. This system uses a holographic inscription method (see Figure 2.10), which provides the flexibility to produce VBGs with different periods and investigate the possibility to record PMMA VBGs with very small period. Ultimately, the smallest grating period that can be produced equals half of the recording wavelength.

8.2 Inscription with the Phase Mask Technique

8.2.1 Inscription and Characterisation Setup

The first experimental setup that was used for VBG inscription is shown in Figure 8.2. The recorded wavelength was 325 nm, which was generated from a 30 mW He-Cd laser (Kimmon IK3301R-G). The phase mask was placed on the PMMA sample, so that the interference

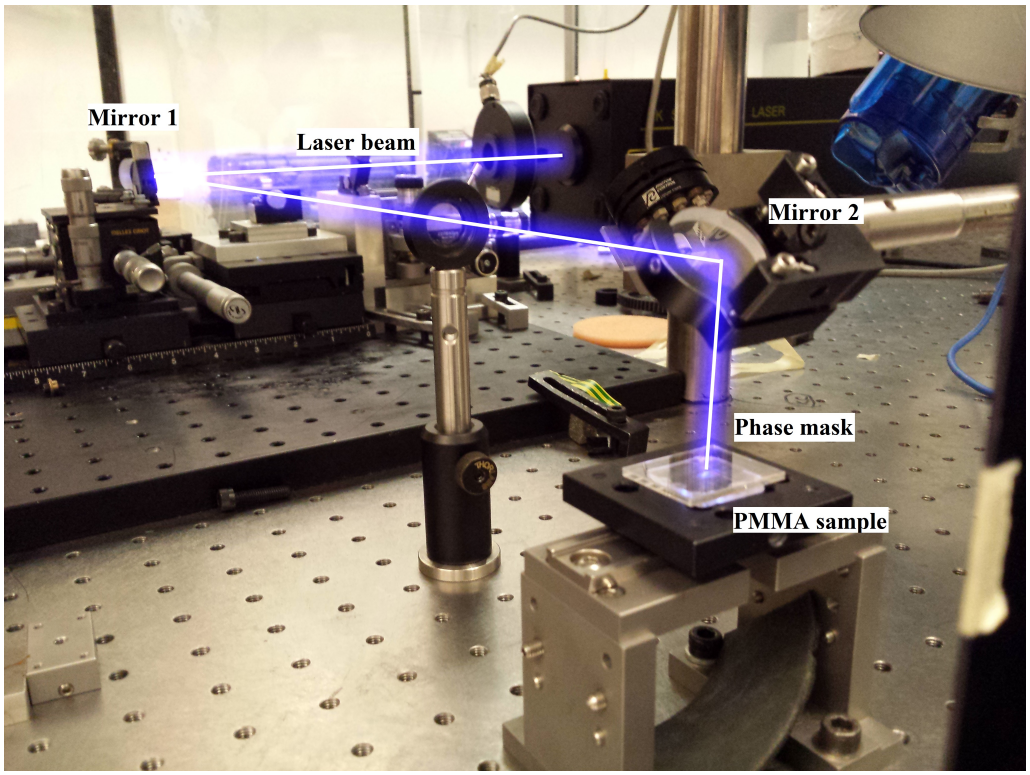

Figure 8.2: Experimental setup of VBG inscription with the phase mask technique.

pattern penetrates the bulk material and forms the periodic grating structure. The laser beam was normal with the surface of the phase mask and PMMA sample, in order to avoid slanted grating planes. Three different phase masks were used in the following experiments with periods of 1062 nm, 1034 nm and 580 nm. The total exposure duration for each VBG was between 45 min and 90 min. The beam size was 1.2 mm and the power density 5 W/cm^2 (see equation 4.1). The thickness of each sample was 1.5$\pm$0.1 mm.

To observe the reconstructed object wave, a visible red laser (He-Ne) operating at 633 nm wavelength with an output power of 1.24 mW was used to probe the grating as a reference wave. The PMMA sample was placed on a rotational stage to control the incident angle of the laser beam, as shown in Figure 8.3. By controlling the incident angle θ_i, the Bragg diffraction condition can be satisfied for a specific angle θ_d, and the diffracted beam can be viewed on the screen behind the sample, as shown in Figure 8.4. Note that the diffracted beam shown in Figure 8.4 occurs only in transmission gratings. In the case of reflection gratings, the beam diffracts at the same side of the sample as the incident beam. The diffracted angles were calculated by measuring the distance between screen and sample, and the distance between transmitted beam and diffracted beam. If the grating planes are parallel with the sample's surface, the diffracted angle equals the incident

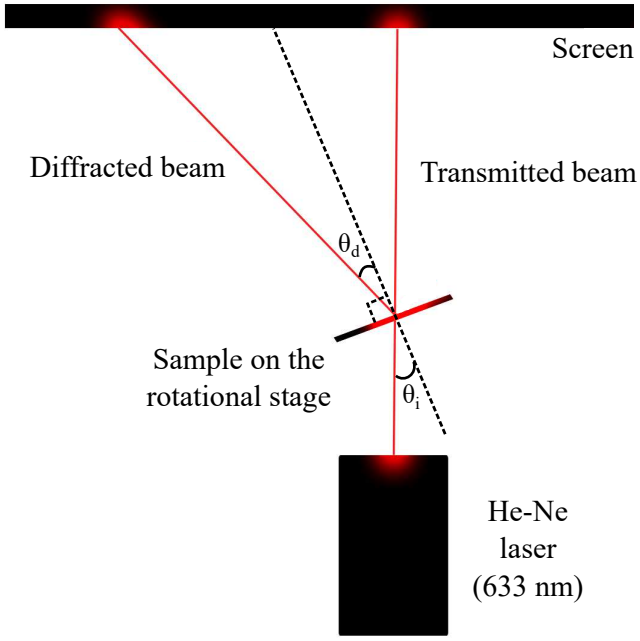

Figure 8.3: Schematic diagram of VBG characterisation.

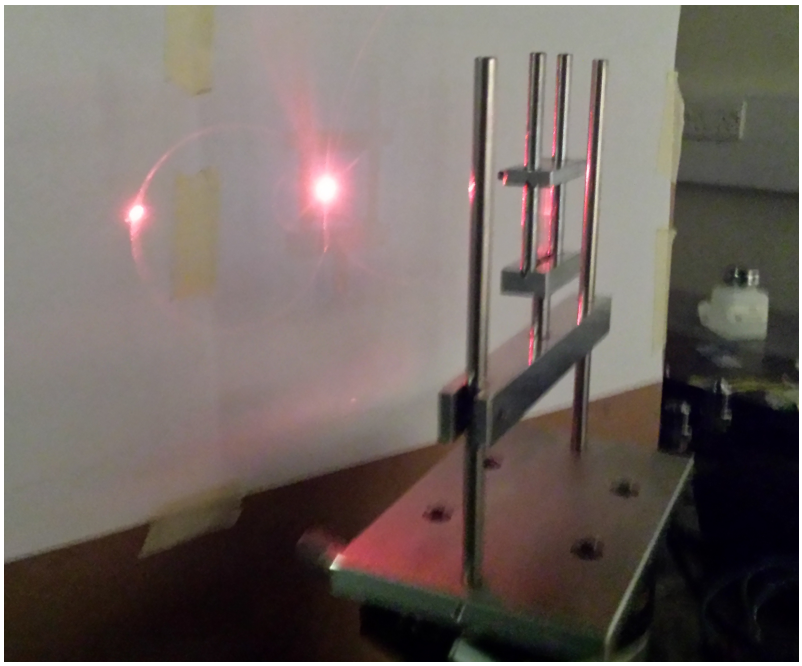

Figure 8.4: VBG characterisation setup. Left: Diffracted beam occurring at the Bragg angle. Right: Transmitted beam.

angle. The diffraction efficiency η equals

$$\eta = \frac{P_d}{P_i}, \tag{8.1}$$

where P_d is the power of the diffracted beam and P_i is the power of the incident beam on the sample. If the diffraction efficiency and the thickness of the material are measured, the maximum

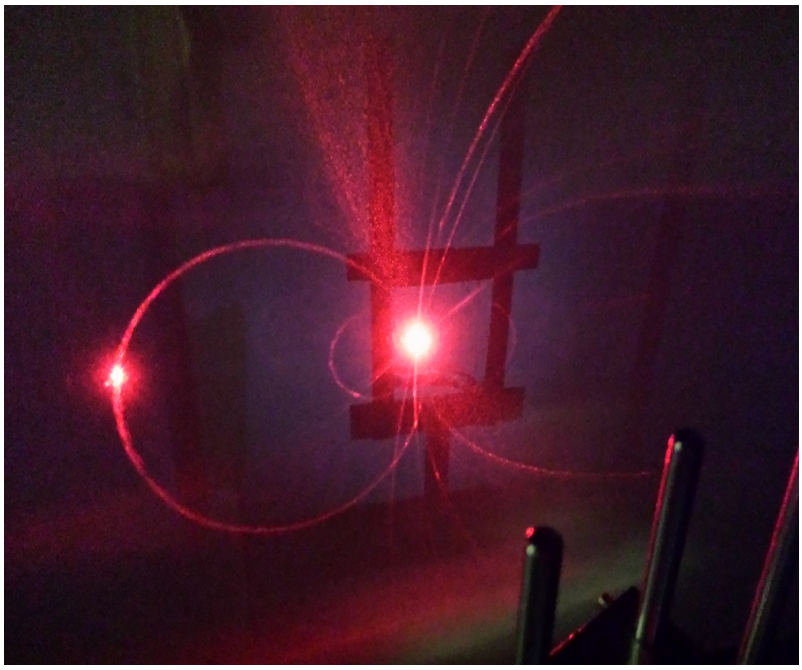

Figure 8.5: Observed rings generated from noise gratings. Left: Diffracted beam at Bragg angle. Right: Transmitted beam.

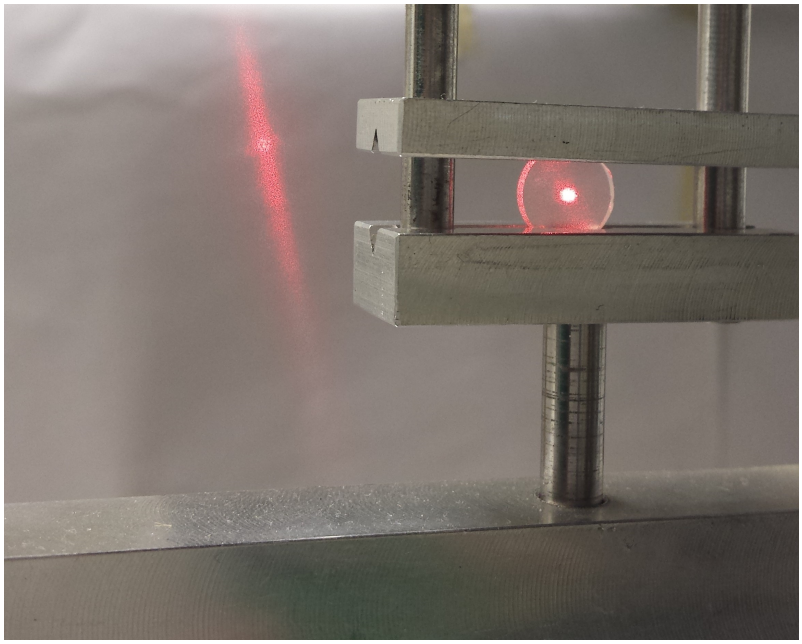

Figure 8.6: Unpolished sample during characterisation.

refractive index modulation can be calculated [216].

Figures 8.4 and 8.5 show a pattern of rings appearing on the far-field transmission. These rings originate from a bright spot, which is the transmitted beam. As the sample is rotated, the ring becomes larger. At the Bragg angle, the ring passes through the transmitted and the diffracted

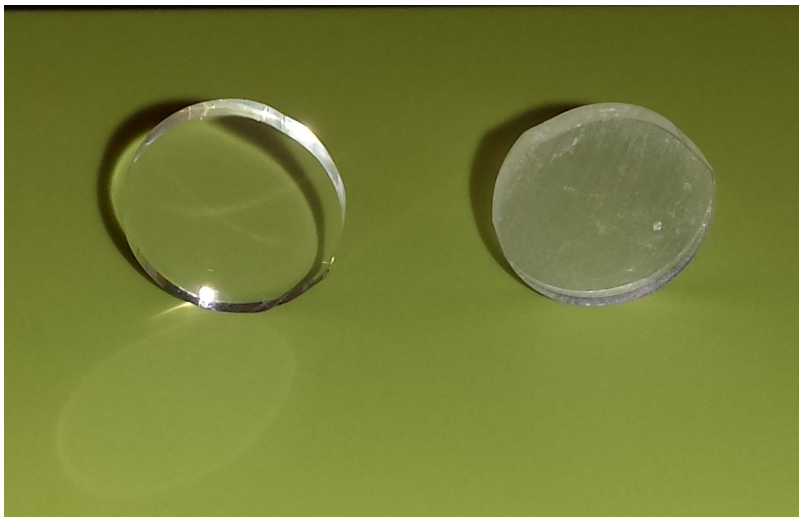

Figure 8.7: PMMA samples. The left is polished and the right is unpolished.

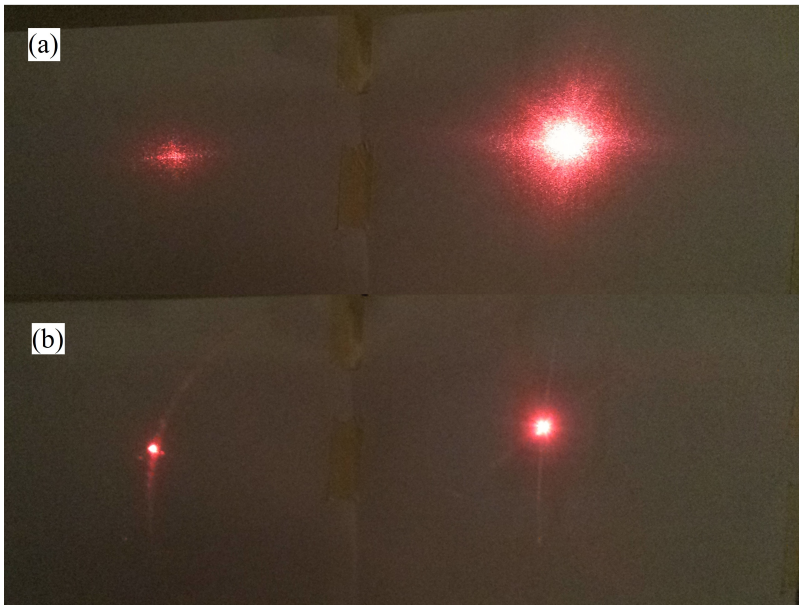

Figure 8.8: (a) Unpolished and (b) polished PMMA sample as shown on the screen during the characterisation. On the right is the transmitted beam and on the left is the diffracted beam.

beam, as is clearly illustrated in Figure 8.5. The first observation of these rings were made in PMMA by Moran and Kaminov in 1973 [101]. The explanation was provided by Forshaw [217] using an Ewald sphere; a geometric construct, which shows the relationship between the wave vectors of the incident and diffracted beams, the diffraction angle, and the reciprocal lattice (grating) vector. Each ring is a replay hologram from noise gratings, also called scatter gratings. These spurious grating structures were produced during the VBG recording, due to light scatter that is produced in the inhomogeneous material. The non-linear relationship between exposure

and the refractive index change of the material can also lead to additional rings (see Figure 8.5), due to additional harmonics in the grating profile. In general, the noise gratings lead to a reduction of diffraction efficiency; therefore, homogenous recording materials are desirable.

The PMMA samples should also be polished. Figure 8.6 shows an unpolished sample during its characterisation. At the far-end screen a blurred transmitted beam is observed. In this work, the PMMA samples were polished using a similar method as described in section 4.4. Figure 8.7 shows the difference between a polished and unpolished sample. The difference can be seen on the screen during the characterisation, as depicted in Figure 8.8.

8.2.2 Results and Discussion

Following the inscription with the phase mask technique, multiple diffracted angles were observed during the reconstruction of each VBG. Two different diffracted beams at the same incident angle were also observed as shown in Figure 8.9. Table 8.1 shows all the diffracted angles observed in various positions on the screen, when a phase mask with period of 1062 nm was used for the VBG recording. The recording process was repeated in 5 different samples and the results show consistent diffracted angles. The VBG inscription duration for each sample is listed in Table 8.2. Table 8.3 and Table 8.4 list the diffracted angles when the phase masks with period 1034 nm and 580 nm were used respectively for the recording. The total VBG inscription time was 60 min and 75 min with each phase mask, respectively.

The results above indicate multiple Bragg grating diffractions at unknown angles, while it was anticipated to observe only the fundamental grating period and possibly its higher harmonics. An assumption was made that the phase mask has additional orders (0 and ± 2 orders) that can effectively interact with the main ± 1 orders creating additional Bragg grating structures. As mentioned in the introduction, the Ewald sphere diagram can be used to show the relationship between the wave vectors (incident and diffracted beams), the diffraction angle, and the grating vector. As shown in Figure 8.10, two identical wave vectors at some angle can form a grating vector K, which equals

$$h\,K = 2\,k\,sin\left(\frac{\theta}{2}\right), \tag{8.2}$$

where h is the harmonic of grating, k is the wave vector and θ is the angle between the wave vectors. The angles α and β shown in Figure 8.10 are between each wave vector and the normal of sample's surface. If the angles α and β of the recording wave vectors are different, the recorded grating will be slanted with the sample's surface. The grating vector K equals $2\pi n/\Lambda$, where Λ is the period of the grating, and the wave vector k equals with $2\pi n/\lambda$, where λ is the recording or the replay free-space wavelength and n is the refractive index of the medium. We should note that when the reference beam hits the developed VBG, its wavelength change due

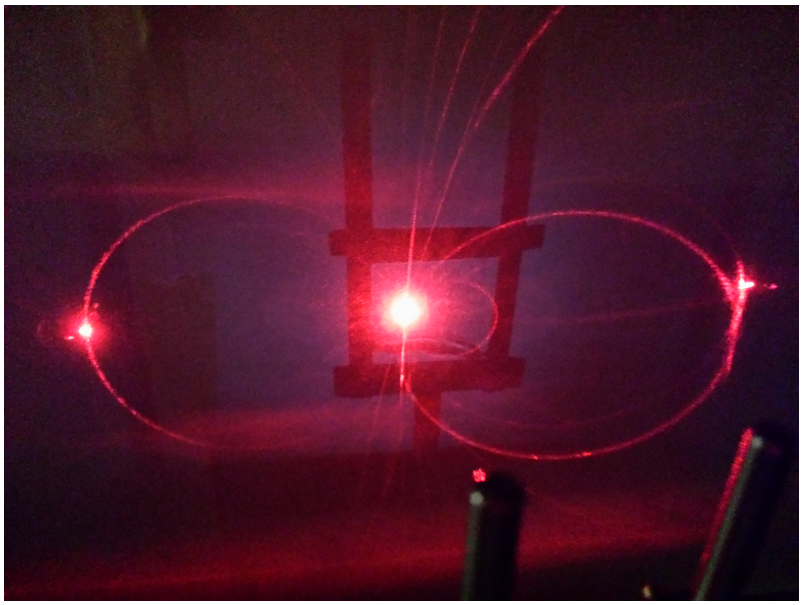

Figure 8.9: Two diffracted beams (left and right) at the same incident angle. At the centre is the transmitted beam.

to refractive index difference (from free-space to PMMA medium), but so do the angles due to refraction (Snell's law), therefore the grating period in the above equations remains the same. Therefore, the refractive index of the material can be neglected, since any changes occurred when the light is entering the VBG are cancelled out, when the light is exiting the material. In this work, the recording wavelength is 325 nm (free-space wavelength of He-Cd laser) and the replay wavelength is 633 nm (free-space wavelength of He-Ne laser). Due to different recording and replay wavelengths, the recording angles and the replay (diffracted) angles were different (see equation 8.2). When the phase mask technique is used for the VBG recording, the recording angles can be calculated. In general, the phase mask diffracted angle z is equal to

$$z = sin^{-1}\left(\frac{m\,\lambda_{UV}}{\Lambda_{PM}}\right), \tag{8.3}$$

where Λ_{PM} is the period of phase mask, λ_{UV} is the recording wavelength, and m is the diffraction order of phase mask. If the phase mask has only the ± 1 orders, the interference pattern from these two wave vectors create only one grating vector K, which means only one grating structure. However, the presence of 0 and ± 2 orders creates additional interference patterns, and consequently increases the number of the recording gratings to 10, as shown in Figure 8.11.

Table 8.5 lists the diffraction angle of each phase mask's order, when the phase mask is placed parallel with the sample's surface. These angles were used to calculate the replay angles α and β of each grating structure. Table 8.6 lists the theoretical Bragg angles for all VBGs recorded with the 1062 nm phase mask when a red laser (633 nm) was used for the reconstruction. The grating

Table 8.1: Diffracted angles observed with the 1062 nm phase mask.

VBG position	Sample	Incident angle	Diffracted angle	Diffraction efficiency
1	1	10°	26°	1%
	2	10°	27°	1%
	3	10°	26°	10%
	4	10°	24°	1%
	5	5°	29°	-
2	2	10°	-48°	9%
	3	10°	-50°	10%
	5	5°	-44°	-
3	1	28°	8°	1%
	2	28°	9°	1%
	3	28°	8°	1%
	4	28°	7°	1%
	5	23°	11°	-
4	5	33°	39°	-
5	1	50°	-10°	15%
	2	49°	-8°	8%
	3	50°	-10°	2%
	4	50°	-10°	1%
	5	44°	-6°	-
6	1	-7°	46°	8%
	2	-8°	49°	23%
	3	-7°	34°	33%
	4	-7°	45°	3%
	5	-12°	51°	-
7	5	-12°	-23°	-
8	1	-25°	-4°	10%
	2	-26°	-9°	1%
	3	-25°	-0.1°	1%
	4	-26°	-10°	1%
	5	-30°	-6°	-
9	5	-41°	-34°	-
10	1	-46°	9°	8%
	2	-47°	9°	26%
	3	-45°	5°	44%
	4	-46°	6°	3%
	5	-52°	13°	-

Table 8.2: Total VBG inscription time for each sample.

Sample	VBG inscription time (min)
1	60
2	90
3	60
4	45
5	60

Table 8.3: Diffracted angles observed with the 1034 nm phase mask.

VBG position	Incident angle	Diffraction angle
1	7°	29°
2	7°	-48°
3	25°	16°
4	35°	39°
5	47°	-8°
6	-10°	51°
7	-10°	-27°
8	-30°	-7°
9	-40°	-36°
10	-51°	10°

Table 8.4: Diffracted angles observed with the 580 nm phase mask.

VBG position	Incident angle	Diffraction angle
1	15°	55°
2	53°	17°
3	-18°	-52°
4	-44°	-26°

Table 8.5: Angle from the normal of sample's surface for each phase mask order.

	0 order	$\pm$1 order	$\pm$2 order
1062 nm	0°	17.8°	37.8°
1034 nm	0°	18.3°	38.9°
580 nm	0°	34.1°	-

K_4 cannot be reconstructed because its period is too short for the replay wavelength (633 nm); i.e. the grating vector K_4 is longer than the diameter of Ewald sphere. Table 8.7 and Table 8.8 list the theoretical angles for 1034 nm and 580 nm phase masks, respectively. In the case of inscription with the 580 nm phase mask, only the wave vectors K_2 and K_3 can be reconstructed with the

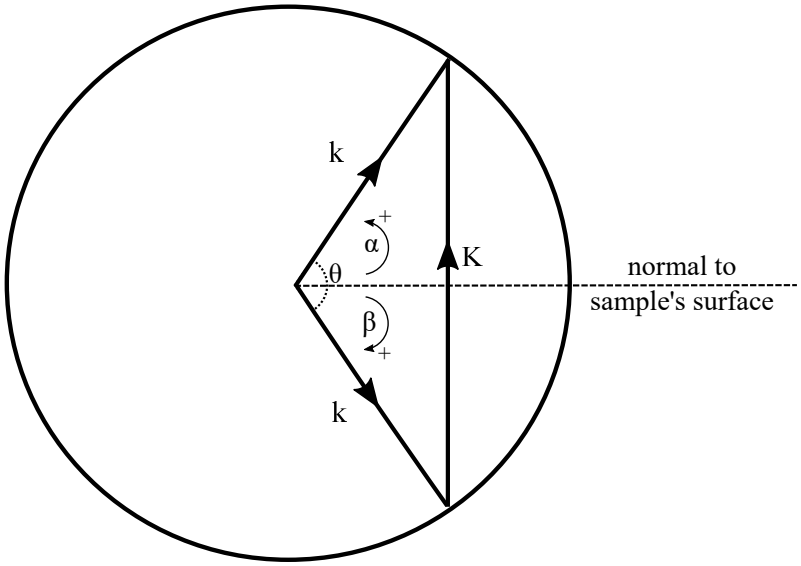

Figure 8.10: Ewald sphere representation of grating recording.

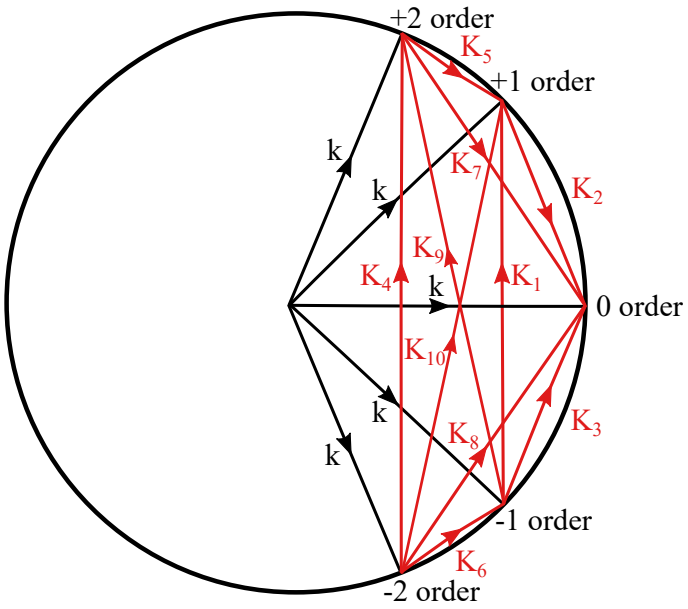

Figure 8.11: Multiple recording gratings due to multiple wave vectors.

Table 8.6: Replay angles for each grating vector (1^{st} harmonic) for 1062 nm phase mask.

	K_1	K_2	K_3	K_4	K_5	K_6	K_7	K_8	K_9	K_{10}
α	36.6°	26.4°	8.7°	-	47.5°	-8.1°	58.0°	20.2°	59.0°	39.0°
β	36.6°	8.7°	26.4°	-	-8.1°	47.5°	20.2°	58.0°	39.0°	59.0°

633 nm replay wavelength. Comparing the experimental results from the Tables 8.1, 8.3, and 8.4, the observed diffracted angles are similar with the theoretical replay angles listed in Tables 8.6, 8.7, and 8.8. Each observed VBG can be linked with one of the grating vectors, which indicates

Table 8.7: Replay angles for each grating vector (1^{st} harmonic) for 1034 nm phase mask.

	K_1	K_2	K_3	K_4	K_5	K_6	K_7	K_8	K_9	K_{10}
α	37.7°	26.8°	9.2°	-	49.0°	-8.2°	59.9°	21.0°	79.1°	58.5°
β	37.7°	9.2°	26.8°	-	-8.2°	49.0°	21.0°	59.9°	58.5°	79.1°

Table 8.8: Replay angles for each grating vector (1^{st} harmonic) for 580 nm phase mask.

	K_1	K_2	K_3
α	-	51.9°	17.7°
β	-	17.7°	51.9°

that the assumption of multiple diffraction orders of phase mask is correct. The observed VBGs related with the respective theoretical grating vectors are summarised in Tables 8.9, 8.10, and 8.11.

Table 8.9: VBG positions related with grating vectors (1062 nm phase mask).

VBG position	1	2	3	4	5	6	7	8	9	10
Grating vector	K_3	$-K_6$	K_2	K_1	K_5	K_6	$-K_3$	$-K_2$	$-K_1$	$-K_5$

In conclusion, the phase mask approach, although simple for recording, leads to a complex response making it difficult to use in practice. The complex behaviour observed has been explained with the presence of the additional phase mask's orders, which produced multiple VBG structures in the material. Despite the explanation provided for the additional VBGs, the phase mask inscription is not suitable to produce VBGs with high diffraction efficiency. In addition, the grating period is defined only by the phase mask period; therefore, the phase mask approach cannot be used to investigate the spatial recording resolution limit of Bragg grating devices, which was one of the milestones of 'TRIPOD' project.

8.3 Inscription with the Holographic Technique

A new inscription system has been developed by my colleague Michał Zubel as shown in Figure 8.12, which was used by me to inscribe the following VBGs. The He-Cd laser beam is first split by utilising the 580 nm phase mask, which is located after the third mirror. The last two mirrors are placed at the right position in order to receive only the ± 1 orders of the phase mask. The zeroth order is blocked by placing an obstacle in front of the phase mask. The advantage of this system is that there are only two laser beams, which record only one VBG structure each

Table 8.10: VBG positions related with grating vectors (1034 nm phase mask).

VBG position	1	2	3	4	5	6	7	8	9	10
Grating vector	K_3	$-K_6$	K_2	K_1	K_5	K_6	$-K_3$	$-K_2$	$-K_1$	$-K_5$

Table 8.11: VBG positions related with grating vectors (580 nm phase mask).

VBG position	1	2	3	4
Grating vector	K_3	K_2	$-K_3$	$-K_2$

time. However, higher harmonics of the grating may possibly be observed, due to the non-linear relationship between exposure and refractive index modulation. Another advantage of this system is that the last two mirrors before the PMMA sample in the inscription setup (see Figure 8.12) are able to rotate and change the angle between the two interfered beams. This characteristic provides the flexibility to record a VBG with any desired period. The grating period Λ is equal to

$$\Lambda = \frac{\lambda_{UV}}{2sin\beta}, \tag{8.4}$$

where β is the half angle between the interfered beams as shown in Figure 8.12. The angle β equals

$$\beta = tan^{-1}\left(\frac{x}{y}\right), \tag{8.5}$$

where x is the half distance between the last two mirrors and y is the distance between the centre of mirrors and the sample, as illustrated in Figure 8.12. When the two incident beams are from the same side of the sample, the recorded VBG is a transmission hologram, as illustrated in Figure 8.13 (a). When the incident beams are from the opposite sides, then the recorded VBG is a reflection hologram, as shown in Figure 8.13 (b). The transmission and reflection grating can be defined such as each Bragg plane is across the 'A' and 'B' axes, respectively (see Figure 8.13).

In general, to observe the diffraction angle of the VBG during the reconstruction process, its period should be equal to or greater than half of the replay wavelength (similar as equation 8.4). This means if the He-Ne laser is used as the replay wavelength (633 nm), the shortest VBG period that can be observed in vacuum is 316.5 nm and in PMMA 215 nm. To observe VBGs with shorter periods, a different laser with a shorter wavelength should be used. Therefore, to investigate the spatial recording resolution limit of Bragg grating structures and record a VBG with a very small period, the He-Cd laser was used as both reconstructed and replay wavelength. However, the laser intensity was reduced to 40% in total during the reconstruction process in order

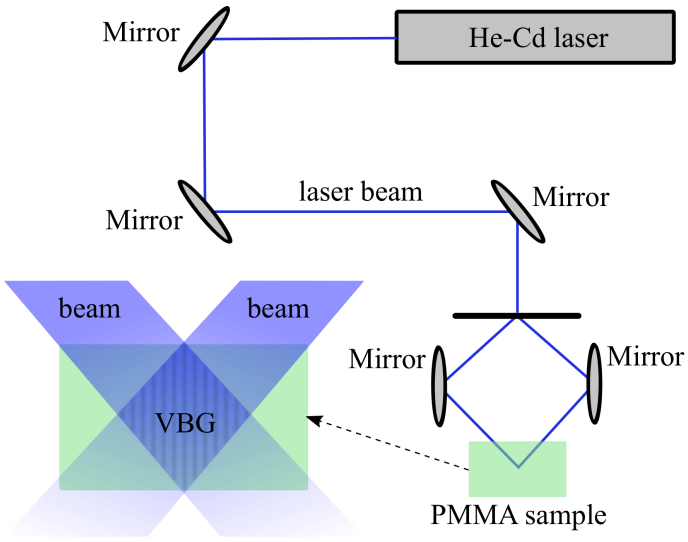

Figure 8.12: Inscription setup of VBG devices with the holographic technique.

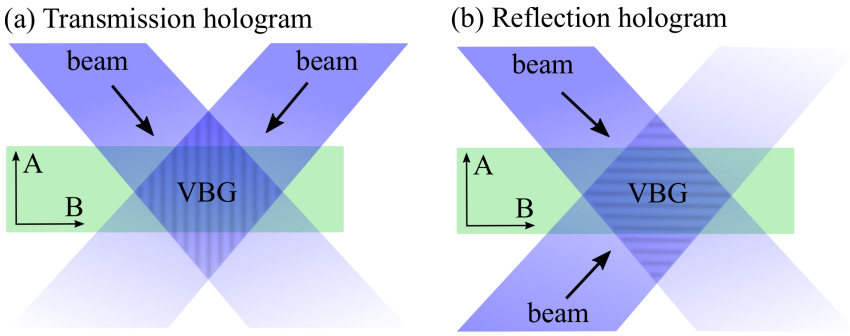

Figure 8.13: (a) Transmission and (b) reflection grating.

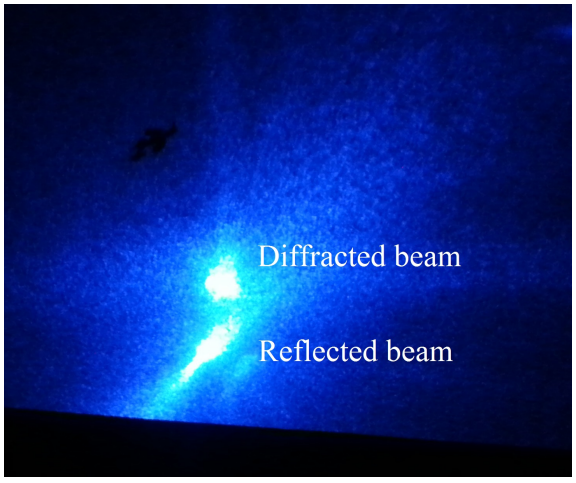

Figure 8.14: Diffracted and reflected beam from a reflection hologram.

to avoid erasing the VBG during its characterisation. In addition, to characterise the VBG takes

Table 8.12: VBGs recorded with different periods in PMMA.

VBG	Inscription time (hours)	Grating period (nm)	Bragg wavelength (nm)	Diffraction efficiency
1	1.5	385	1132	10%
2	1.5	364	1070	0.3%
3	1.5	294	864	0.3%
4	3	165	485	7%

less than 5 minutes, which is much less than the inscription duration. Table 8.12 lists various VBGs that have been recorded with different periods. The VBGs 1-3 are transmission holograms and they were exposed 1.5 hour at 30 mW. The VBG 4 is a reflection hologram and it was exposed 3 hours at 12 mW (40% of total power). The Bragg wavelengths listed in Table 8.12 are calculated by assuming a refractive index of 1.47. Note that the the refractive index change introduced in the material, which defines the diffraction efficiency, can be affected by the disturbances of the recording system (e.g. vibration). It is assumed that for shorter periods, this phenomenon is worse. On the other hand, when inscribing a VBG with shorter period, there are more Bragg planes in the VBG structure, because the grating length remains the same; the grating length is defined by the laser beam width, which is 1.2 mm.

The shortest VBG period that can be inscribed with the He-Cd laser (operating at 325 nm) is 162.5 nm, with the incident angle β being equal to 0 or π (see equation 8.4). However, observing the VBG will be practically difficult, because the diffracted beam will coincide with the incident replay beam. For this reason, VBG 4 was placed between the mirrors with some offset distance ($y < 1$ cm), so that the two incident beams had slightly less than 180° difference. Therefore, the recorded VBG 4 was a reflection hologram with its diffracted beam being close to the reflected beam, as shown in Figure 8.14.

8.4 Discussion and Conclusion

To investigate the limitations of the Bragg grating structures in polymer optical devices is important. First, this chapter investigates the ability to inscribe VBGs in PMMA bulk materials with the He-Cd laser. The phase mask technique proved to be an unreliable method to produce VBG structure due to the existence of multiple diffraction orders from the phase mask. On the other hand, VBG inscription with the holographic method seems reliable to produce only one VBG structure and provides the flexibility to produce a Bragg grating with any desired period. However, the difficulty of getting repeatable efficiency measurements was the main reason of not

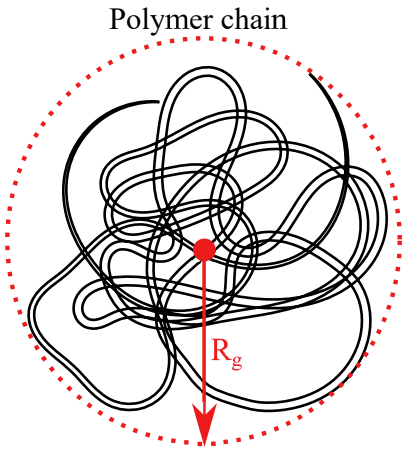

Figure 8.15: Defining the size of the polymer chain.

progressing this work to the next stage, which is the photosensitivity evaluation of different PMMA materials. The last two mirrors shown in Figure 8.13 rotate manually, which possibly introduce an error during the beam combining on the sample's surface. This could be the main reason for the fluctuation on the diffraction efficiency measurements. Using an automatic rotation of mirrors with the help of a software can solve this issue.

This chapter also investigates the possibility to inscribe a VBG of short period in PMMA, because the existence of long polymer molecules in the PMMA material could possibly affect the spatial recording resolution. The physical size of a polymer is described by the radius of gyration R_g, which is the root mean square distance of each point on the polymer chain from its center of mass, as shown in Figure 8.15. The average radius of gyration of PMMA is usually 4 nm, which means a diameter of approximately 8 nm [218]. This molecular size could affect the recording resolution of Bragg grating devices. The shortest Bragg grating period reported in literature is 204 nm (600 nm Bragg wavelength in the PMMA medium) [219]. In this work, a VBG structure with period equal to 165 nm is demonstrated and its Bragg wavelength is 485 nm in the PMMA medium. This period is the lowest possible that can be inscribed with the He-Cd laser. The work reported in this chapter can be continued in the future in order to explore the influence of the size of the grating period on the change of the refractive index introduced in the polymeric material. Someone will expect as the period becomes shorter, the modulation of refractive index is less due to the spatial recording resolution limit, which results from the existence of the long polymer molecules.

9 Discussion and Future Work

This chapter summarises the research objectives and accomplishments, and it provides the directions for future work. In general, the main objective was to fabricate, optimise and characterise the Bragg grating based devices, and help other researchers to use this technology to develop novel end-user applications for sensing.

9.1 Review of the Research Challenges and Objectives

As mentioned previously, POFBG sensors have various advantages in certain situations over silica based sensors, due to their different material and optical properties (see section 2.1.2). Since the first report of POF in 1967 [40] and the first demonstration of POFBG in 1999 [102], the POF technology has not reached a mature level yet with various drawbacks still being existent. The 'TRIPOD' project was formed to tackle most of the existing challenges, establish a mature version of the POF technology and increase their commercial exploitation. The main tasks of the project were to produce new types of polymeric materials and optical fibres, fabricate optimised POFBGs, and develop novel applications for sensing.

The objectives of the work described in this thesis are:

1. Investigate the attenuation effects on POFBGs and Bragg grating based Fabry-Pérot sensors. As mentioned in section 2.1.2, one of the main drawbacks of POF technology is the high optical attenuation. The fibre loss can influence the performance of Bragg grating and Fabry-Pérot (FP) interferometric sensors. The sensitivity of FP sensors can be decreased by the attenuation present in the interferometric cavity, while in the case of POFBGs, the reflection and transmission coefficients can be also reduced. Therefore, there was a need to investigate the attenuation effects on the POF based sensors.

2. Inscribe POFBGs in various types of POFs with the He-Cd laser system. The inscription time of POFBG device depends on the fibre chemical composition.

3. Connectorise the POFBGs with connection loss less than 2 dB.

4. Multiplex the POFBG sensors using the thermal annealing process.

5. Inscribe POFBG devices with more than 90% reflectivity in less than 10 minutes.

6. Optimise the performance of POFBG sensors utilising the thermal annealing process to enhance their strain, stress, and force sensitivities.

7. Distribute the sensors to other researchers in order to develop novel applications.

8. Investigate the possibility to effectively record volume Bragg gratings (VBGs) in PMMA materials. The inscribed VBGs can be used to calculate the introduced refractive index change and assess the photosensitivity of the polymer material.

9. Inscribe a Bragg grating structure with the shortest possible period. Inscribing Bragg gratings with very short periods can be used to investigate the spatial recording resolution limit of some polymeric materials.

9.2 Summary of Research Accomplishments

In this section, the work that was performed to reach the above objectives is summarised and discussed. As already mentioned, the main objective was to produce Bragg grating based devices for 'TRIPOD' partners. At the beginning, there was a question of how the fibre loss influences the characteristics of Bragg gratings and the sensitivity of interferometers when they are fabricated in POFs. For this reason, the attenuation effects on the POFBGs and Bragg grating based FP sensors were investigated. Chapter 3 presents a system model that was developed in MATLAB and it was used to perform this investigation. First, the attenuation term was added in coupled-wave equations in order to investigate how the fibre loss affects the reflection and transmission coefficients of

POFBGs. Then, Bragg grating based FP sensors used for stress sensing were studied. Results show that the stress sensitivity of FP sensors depend on the operational wavelength which influence the fibre loss, reflection and transmission coefficients of Bragg gratings forming the interferometric cavity, and fibre type used to produce the FP sensors. Three different fibre materials were used in this model for illustration: PMMA, CYTOP and fused silica. These materials have different material properties (Young modulus), but also different attenuation values. The FP sensors have been also characterised in three different wavelength regions, where commercial components and detectors are readily available: 650 nm, 850 nm, and 1550 nm. The presented model can be used to calculate the optimum interferometric cavity length in which the FP sensor exhibits maximum stress sensitivity. In the case of FP interferometers formed with two Bragg gratings, the optimum grating length for maximum stress sensitivity can be also calculated. The presented model is not limited to these materials or wavelengths, and it can be also used to characterise any FP interferometric device with the right adjustments. The work presented in chapter 3 can be used to evaluate the performance of the FP stress sensor and identify which optical medium can offer the highest sensitivity when the physical dimensions of the device have been already decided. On the other hand, it can be also used to calculate the physical dimensions of the FP device when the type of optical medium and the operational wavelength have been predefined.

Chapter 4 describes the experimental process that was followed to produce POFBG sensors for 'TRIPOD' partners. The POFBGs were produced in various types of POFs using the common He-Cd laser system. The chapter lists the time required to inscribe a POFBG in each type of POF. The results show that the inscription time is strongly depended on the chemical composition of POF. The chapter also demonstrates two additional accomplishments. First, a novel demountable connectorisation method of POF was demonstrated, by placing it in FC/PC connectors. The achieved connection loss was less than 0.85 dB, which is the lowest reported until now. The objective of the 'TRIPOD' consortium was to achieve a connection loss less than 2 dB. The second accomplishment was the demonstration of a novel methodology for POFBG multiplexing. Until now, the thermal annealing process was being used to permanently tune the Bragg wavelength only to shorter wavelengths. In this thesis, a permanent Bragg wavelength shift to longer wavelengths was demonstrated for the first time by combining the thermal annealing and fibre stretching. This work can be used to multiplex the POFBG sensors at any desirable wavelength utilising only one phase mask for the POFBG inscription. In the case where the thermal annealing is used for other purposes (i.e. change material properties of POF), the Bragg wavelength can be kept at its original desired spectral position by utilising the right degree of fibre stretching and thermal annealing conditions.

In chapter 5, a new methodology was developed to produce POFBG sensors fast, reliably,

effectively and with high reflectivity, which was one of the objectives. Instead of trying to produce POFs with higher photosensitivity at the common 325 nm wavelength, the idea was to expose the PMMA POF to a shorter UV wavelength, where it exhibits enhanced photosensitivity. The motivation for this work was the first demonstration of a POFBG produced using a 248 nm KrF laser system in 2015 [33]. It was impossible before to inscribe with UV wavelengths shorter than 325 nm, due to ablation issues. However, chapter 5 shows that one KrF laser pulse is adequate to produce a POFBG sensor with physical length of 1 cm and 98.4% reflectivity in a single-mode PMMA POF doped with BDK. This is the fastest POFBG inscription time (15 ns) reported until now. In the work reported in this chapter, my objectives as written in section 1.2 were also reached (grating physical length > 1 cm, reflectivity > 90%, and inscription time < 10 minutes).

In general, optimised sensors with enhanced sensitivity are desired. As previously mentioned, the thermal annealing used for multiplexing purposes, increased the pressure sensitivity of one of the sensors used for liquid level monitoring. A further study was performed and presented in chapter 6. The results show that thermal annealing can enhance not only the strain sensitivity of POFBG sensors, as previously reported, but also the stress and force sensitivity. A simpler, well-controlled and cost-effective POF annealing process was also demonstrated. Chemical etching the POFBG can also influence the strain, and stress sensitivities. However, the changes seem random and small. The introduced changes after the etching process are possibly due to the change of the non-uniform internal stress distribution caused by the diameter reduction. Despite that, the etching can be useful in applications used to detect axial force.

Chapter 7 presents three novel applications that were developed by other researchers using my POFBG sensors produced by the work described in chapter 4. The first application was developed for ultrasound detection. The PMMA based sensors are small in size and they can detect frequencies of 1 MHz, 5 MHz, and 10 MHz, which lie in the spectrum range used for 2D and 3D opto-acoustic imaging. In the second application, an array of POFBG sensors was developed for liquid level monitoring. The system reported in this work exhibits 4 times higher sensitivity (98 pm/cm) compared with the reported silica based liquid level monitoring system (23 pm/cm). This system was also tested with JET A-1 aviation fuel and it can find application in aviation fuel level monitoring. In the last application, a POFBG sensor was coated with graphene and it was used to detect directly the concentration of human erythrocytes (red blood cells), which are essential for the survival of a person. The sensor presented in this work is biocompatible, compact, and offers a state-of-the-art fibre-optic sensing platform for in-situ and in-vivo erythrocyte concentration monitoring. Presumably this approach lacks specificity in that it will respond to other biological/biochemical species too.

Chapter 8 demonstrates the inscription of VBGs in PMMA materials. Initially, the inscriptions

of VBGs were performed with the phase mask technique, but it was proved unsuitable for our purpose; the existing multiple diffraction orders of the phase mask produced multiple VBG structures, which were eventually identified by theoretical modelling. Thereafter, the holographic inscription method was used to produce the VBG devices, but the diffraction efficiency was not repeatable and the process was time-consuming. The shortest Bragg grating period with Bragg wavelength of 485 nm in PMMA medium was also reported.

9.3 Future Work

First, the model system presented in chapter 3, which investigates the effects of fibre loss on the performance of Bragg grating based sensors, can be experimentally implemented to confirm the theoretical results. The model system can be easily tested with the KrF laser system, which can be used to effectively inscribed the Bragg grating mirrors of FP interferometer. Inscribing FP interferometers with different cavity lengths, their stress sensitivity will vary according to the theoretical model.

Although the POFBG technology has been dramatically improved by the 'TRIPOD' consortium, there is still room for a further improvement and optimisation. Additional photosensitivity studies to investigate the mechanisms involved during the photo-inscription are needed. Lasers emitting at 325 nm were being used for two decades for POF based device inscription. However, the inscription process typically requires tens of minutes (see chapter 4), which increases the fabrication cost of each POFBG sensor. In this thesis, a fast inscription with a 248 nm wavelength is demonstrated (see chapter 5) and it shows the huge potential for moving to a shorter inscription wavelength. Despite the introduced refractive index change of 0.74×10^{-4} with one laser pulse, the irradiation conditions (i.e. energy density) need to be further optimised for higher refractive index change. On the other hand, the benzyl dimethyl ketal dopant added in the POF seems very promising, but its concentration in the fibre core needs also to be optimised for enhanced photosensitivity.

Additional work is required in the future to repeat some of the results regarding the permanent tuning of Bragg wavelength to longer wavelengths (see chapter 4). My suggestion is to apply a constant fibre stress rather than constant strain during the thermal annealing process, and try to investigate different annealing durations and temperatures. This work will have high impact on future multiplexing procedures applied on the POFBG sensors and it could be beneficial when the annealing method is used to improve the characteristics of POFBG sensors (i.e. enhanced strain and stress sensitivity) and the Bragg wavelength is desired to be kept at its original spectral position.

In addition, the thermal annealing has a positive impact on the performance (see chapter 6) and lifetime (see chapter 5) of POFBG sensors. The thermal annealing impact on strain, stress, and force sensitivities of POFBG sensors can be further explored with different annealing temperatures and durations. The chemical etching process can be also repeated to confirm the results shown in chapter 6, and in order to have a clearer picture on the effects of chemical etching on POFBG sensors. In general, the thermal and chemical treatment can be applied in the future to optimise the POFBG sensors to have enhanced sensitivity when they are used in strain, stress, force, pressure, and acoustic-wave detection applications.

The novel applications presented in chapter 7 shows the potential of POFBG sensors to be used in ultrasound imaging, aviation fuel level monitoring, and erythrocyte concentration monitoring. However, the POFBG applications are not limited on these fields and additional applications can be developed in the future for various industrial sectors, including the biomedical, aerospace, civil, energy, and environmental sectors.

References

[1] H. Stoll and A. Yariv, "Coupled-mode analysis of periodic dielectric waveguides," *Opt. Comm.*, vol. 8, no. 1, pp. 5–8, 1973.

[2] G. Meltz, W. W. Morey, and W. H. Glenn, "Formation of Bragg gratings in optical fibers by a transverse holographic method," *Opt. Lett.*, vol. 14, no. 15, pp. 823–5, 1989.

[3] V. Lecoeuche, P. Niay, M. Douay, P. Bernage, S. Randoux, and J. Zemmouri, "Bragg grating based Brillouin fibre laser," *Opt. Commun.*, vol. 177, no. 1-6, pp. 303–306, 2000.

[4] H. Y. Liu, H. B. Liu, G. D. Peng, and P. L. Chu, "Polymer optical fibre Bragg gratings based fibre laser," *Opt. Commun.*, pp. 132–135, 2006.

[5] F. Ouellette, "All-fiber filter for efficient dispersion compensation," *Opt. Lett.*, vol. 16, no. 5, pp. 303–305, 1991.

[6] T. A. S. Strasser, P. J. Chandonnet, J. DeMarco, C. E. Soccolich, J. R. Pedrazzani, D. J. DiGiovanni, M. J. Andrejco, and D. S. Shenk, "UV-induced Fiber Grating OADM Devices for Efficient Bandwidth Utilization," in *Optical Fiber Comm. Conf.* Optical Society of America, 1996.

[7] H. S. Park, S. H. Yun, I. K. Hwang, S. B. Lee, and B. Y. Kim, "All-fiber add-drop wavelength-division multiplexer based on intermodal coupling," *Photon. Technol. Lett.*, 2001.

[8] C. Headley and G. Agrawal, *Raman amplification in fiber optical communication systems*. Academic press, 2005.

[9] S.-K. Liaw, L. Dou, and A. Xu, "Fiber-Bragg-grating-based dispersion-compensated and gain-flattened raman fiber amplifier," *Opt. Express*, vol. 15, no. 19, pp. 12 356–12 361, 2007.

[10] W. W. Morey, G. Meltz, and W. H. Glenn, "Fiber Optic Bragg Grating Sensors," in *Fiber Optic and Laser Sensors VII*. Proc. SPIE 1169, 1990.

[11] R. Yun-Jiang, "In-fibre Bragg grating sensors," *Meas. Sci. Technol.*, vol. 8, no. 4, p. 355, 1997.

[12] B. Lee, "Review of the present status of optical fiber sensors," *Opt. Fiber Technol.*, vol. 9, no. 2, pp. 57–79, 2003.

[13] S. A. Vasil'ev, O. I. Medvedkov, I. G. Korolev, A. S. Bozhkov, A. S. Kurkov, and E. M. Dianov, "Fibre gratings and their applications," *Quant. Electron.*, vol. 35, no. 12, p. 1085, 2005.

[14] D. J. Webb, "Fibre Bragg grating sensors in polymer optical fibres," *Meas. Sci. Technol.*, vol. 26, no. 9, p. 092004, 2015.

[15] M. C. J. Large, J. H. Moran, and L. Ye, "The role of viscoelastic properties in strain testing using microstructured polymer optical fibres (mPOF)," *Meas. Sci. Technol.*, vol. 20, no. 3, p. 034014, 2009.

[16] F. Bischoff, "Organic polymer biocompatibility and toxicology," *Clin. Chem.*, vol. 18, no. 9, pp. 869–94, 1972.

[17] E. Yoshii, "Cytotoxic effects of acrylates and methacrylates: relationships of monomer structures and cytotoxicity," *J. Biomed. Mater. Res. A*, vol. 37, no. 4, pp. 517–524, 1997.

[18] M. Silva-Lopez, A. Fender, W. N. MacPherson, J. S. Barton, J. D. Jones, D. Zhao, H. Dobb, D. J. Webb, L. Zhang, and I. Bennion, "Strain and temperature sensitivity of a single-mode polymer optical fiber," *Opt. Lett.*, vol. 30, no. 23, pp. 3129–31, 2005.

[19] G. W. C. Kaye and T. H. Laby, *Tables of Physical and Chemical Constants*. London, 1921.

[20] T. X. Wang, Y. H. Luo, G. D. Peng, and Q. J. Zhang, "High-sensitivity stress sensor based on Bragg grating in BDK-doped photosensitive polymer optical fiber," in *Third Asia Pacific Optical Sensors Conf.* Proc. SPIE 8351, 2012.

[21] C. A. F. Marques, A. Pospori, D. Saez-Rodriguez, K. Nielsen, O. Bang, and D. J. Webb, "Aviation Fuel Gauging Sensor Utilizing Multiple Diaphragm Sensors Incorporating Polymer Optical Fiber Bragg Gratings," *Sensors*, vol. 16, no. 15, pp. 6122–6129, 2016.

[22] C. Broadway, D. Gallego, A. Pospori, M. Zubel, D. J. Webb, K. Sugden, G. Carpintero, and H. Lamela, "Microstructured polymer optical fibre sensors for opto-acoustic endoscopy," in *Micro-Structured and Specialty Optical Fibres IV*. Proc. SPIE 9886, 2016.

[23] W. Zhang, D. J. Webb, and G. D. Peng, "Investigation Into Time Response of Polymer Fiber Bragg Grating Based Humidity Sensors," *J. Lightwave Technol.*, vol. 30, no. 8, pp. 1090–1096, 2012.

[24] Z. Zhang, P. Zhao, P. Lin, and F. Sun, "Thermo-optic coefficients of polymers for optical waveguide applications," *Polym. J.*, vol. 47, no. 14, pp. 4893–4896, 2006.

[25] R. M. Waxler and G. Cleek, "Effect of temperature and pressure on refractive-index of some oxide glasses," *J. Res. Nat. Bur. Stand. A: Phys. and Chem.*, no. 6, pp. 755–763, 1973.

[26] H. B. Liu, H. Y. Liu, G. D. Peng, and P. L. Chu, "Strain and temperature sensor using a combination of polymer and silica fibre Bragg gratings," *Opt. Commun.*, vol. 219, pp. 139–142, 2003.

[27] C. Zhang, W. Zhang, D. Webb, and G.-D. Peng, "Optical fibre temperature and humidity sensor," *Electron. Lett.*, vol. 46, p. 643, 2010.

[28] M. G. Kuzyk, U. C. Paek, and C. W. Dirk, "Guest-host polymer fibers for nonlinear optics," *Appl. Phys. Lett.*, vol. 59, no. 8, pp. 902–904, 1991.

[29] A. Tagaya, Y. Koike, T. Kinoshita, E. Nihei, T. Yamamoto, and K. Sasaki, "Polymer optical fiber amplifier," *Appl. Phys. Lett.*, vol. 63, no. 7, pp. 883–884, 1993.

[30] G. Emiliyanov, J. B. Jensen, O. Bang, P. E. Hoiby, L. H. Pedersen, E. M. Kjaer, and L. Lindvold, "Localized biosensing with TOPAS microstructured polymer optical fiber: Erratum," *Opt. Lett.*, vol. 32, p. 1059, 2007.

[31] H. P. A. Van den Boom, W. Li, P. K. Van Bennekom, I. T. Monroy, and K. Giok-Djan, "High-capacity transmission over polymer optical fiber," *J. Sel. Topics Quantum Electron.*, vol. 7, no. 3, pp. 461–470, 2001.

[32] W. R. White, L. L. Blyler Jr, R. Ratnagiri, and M. Park, "Manufacture of perfluorinated plastic optical fibers," in *Optical Fiber Comm. Conf.* OSA, 2004.

[33] R. Oliveira, L. Bilro, and R. Nogueira, "Bragg gratings in a few mode microstructured polymer optical fiber in less than 30 seconds," *Opt. Express*, vol. 23, no. 8, pp. 10 181–7, 2015.

[34] A. Abang and D. J. Webb, "Effects of annealing, pre-tension and mounting on the hysteresis of polymer strain sensors," *Meas. Sci. Technol.*, vol. 25, no. 1, 2014.

[35] I. P. Johnson, D. J. Webb, and K. Kalli, "Utilisation of thermal annealing to record multiplexed FBG sensors in multimode microstructured polymer optical fibre," in *Int. Conf. on Optical Fiber Sensors (OFS21).* Proc. SPIE 7753, 2011.

[36] K. Fukao, S. Uno, Y. Miyamoto, A. Hoshino, and H. Miyaji, "Dynamics of α and β processes in thin polymer films: Poly(vinyl acetate) and poly(methyl methacrylate)," *Phys. Rev. E*, vol. 64, no. 5, p. 051807, 2001.

[37] W. Yuan, A. Stefani, M. Bache, T. Jacobsen, B. Rose, N. Herholdt-Rasmussen, F. K. Nielsen, S. Andresen, O. B. Sorensen, K. S. Hansen, and O. Bang, "Improved thermal and strain performance of annealed polymer optical fiber Bragg gratings," *Opt. Commun.*, vol. 284, no. 1, pp. 176–182, 2011.

[38] G. Woyessa, K. Nielsen, A. Stefani, C. Markos, and O. Bang, "Temperature insensitive hysteresis free highly sensitive polymer optical fiber Bragg grating humidity sensor," *Opt. Express*, vol. 24, no. 2, pp. 1206–13, 2016.

[39] K. Carroll, A. Argyros, K. Kalli, M. Large, D. J. Webb, and C. Zhang, "Extending the working temperature range of Bragg gratings in microstructured polymer optical fibre by annealing," in *Sensors-I.* Int. Coop. of Plastic Optical Fibers, 2007.

[40] T. C. Hager, R. G. Brown, and B. N. Derick, "Plastic fiber optics," *SAE Techn. Paper*, vol. 6, no. 7, pp. 1269–1270, 1967.

[41] D. Kelker and M. G. Kuzyk, "Optical and mechanical multistability in a dye-doped polymer fiber Fabry-Perot waveguide," *Appl. Phys. Lett.*, vol. 66, pp. 2792–2794, 1995.

[42] G. DW, K. Zimmerman, P. Young, J. Tostenrude, T. JS, Z. Zhou, M. Lobel, M. Dayton, R. Wittorf, K. MG, J. Sounick, and D. CW, "Single-mode nonlinear-optical polymer fibers," *J. Opt. Soc. Am. B*, vol. 13, pp. 2017–2023, 1996.

[43] G. D. Peng, P. L. Chu, Z. Xiong, T. Whitbread, and R. P. Chaplin, "Broadband tunable optical amplification in Rhodamine B-doped step-index polymer optical fibre," *Opt. Commun.*, vol. 129, pp. 353–357, 1996.

[44] G. Peng, P. Chu, Z. Xiong, T. Whitbread, and R. Chaplin, "Dye-doped step-index polymer optical fiber for broadband optical amplification," *J. Lightwave Technol.*, vol. 14, pp. 2215–2223, 1996.

[45] M. V. Eijkelenborg, M. Large, A. Argyros, J. Zagari, S. Manos, N. A. Issa, I. M.

Bassett, S. C. Fleming, R. C. McPhedran, C. M. d. Sterke, and N. A. P. Nicorovici", "Microstructured polymer optical fibre," *Opt. Express*, vol. 9, pp. 319–327, 2001.

[46] T. Kaino, M. Fujiki, and S. Nara, "Low-loss polystyrene core-optical fibers," *J. Appl. Phys.*, vol. 52, no. 12, pp. 7061–7063, 1981.

[47] L. Dvořanek, L. Machová, M. Šorm, Z. Pelzbauer, J. Švantner, and V. Kubánek, "Effects of drawing conditions on the properties of optical fibers made from polystyrene and poly(methyl methacrylate)," *Die Angewandte Makromolekulare Chemie*, vol. 174, no. 1, pp. 25–39, 1990.

[48] L. HY, P. GD, C. PL, Y. Koike, and Y. Watanabe, "Photosensitivity in low-loss perfluoropolymer (CYTOP) fibre material," *Electron. Lett.*, vol. 37, pp. 347–348, 2001.

[49] AGC, "Amorphous Fluoropolymer CYTOP," 2009. [Online]. Available: http://www.bellexinternational.com/products/cytop/pdf/cytop-catalog.pdf

[50] I. Johnson, W. Yuan, a. Stefani, K. Nielsen, H. Rasmussen, L. Khan, D. Webb, K. Kalli, and O. Bang, "Optical fibre Bragg grating recorded in TOPAS cyclic olefin copolymer," *Electron. Lett.*, vol. 47, p. 271, 2011.

[51] J. Anthony, R. Leonhardt, A. Argyros, and M. C. J. Large, "Characterization of a microstructured Zeonex terahertz fiber," *J. Opt. Soc. Am. B*, vol. 28, no. 5, pp. 1013–1018, 2011.

[52] A. Tanaka, H. Sawada, T. Takoshima, and N. Wakatsuki, "New plastic optical fiber using polycarbonate core and fluorescence-doped fiber for high temperature use," *Fiber Integrated Opt.*, vol. 7, no. 2, pp. 139–158, 1988.

[53] Z. H. Guerrero G. V. Guinea J, "Mechanical Properties of Polycarbonate Optical Fibers," *Fiber Integrated Opt.*, vol. 17, no. 3, pp. 231–242, 1998.

[54] R. P. Kusy and A. R. Greenberg, "Influence of molecular weight on the dynamic mechanical properties of poly(methyl methacrylate)," *J. Therm. Anal.*, vol. 18, no. 1, pp. 117–126, 1980.

[55] J. M. Yu, X. M. Tao, and H. Y. Tam, "Trans-4-stilbenemethanol-doped photosensitive polymer fibers and gratings," *Opt. Lett.*, vol. 29, no. 2, pp. 156–158, 2004.

[56] S. Saito and T. Nakajima, "Glass transition in polymers," *J. Appl. Polym. Sci.*, vol. 2, no. 4, pp. 93–99, 1959.

[57] M. Foerthner, M. Rumler, F. Stumpf, R. Fader, M. Rommel, L. Frey, M. Girschikofsky, S. Belle, R. Hellmann, and J. Klein, "Hybrid polymers processed by substrate conformal imprint lithography for the fabrication of planar Bragg gratings," *âĂŐAppl. Phys. A*, vol. 122, no. 3, p. 240, 2016.

[58] M. C. Boyce, D. M. Parks, and A. S. Argon, "Large inelastic deformation of glassy polymers. part I: rate dependent constitutive model," *Mech. Mater.*, vol. 7, no. 1, pp. 15–33, 1988.

[59] J. Brandrup, E. H. Immergut, E. A. Grulke, A. Abe, and D. R. Bloch, *Polymer handbook*. Wiley New York, 1999.

[60] C. Jiang, M. G. Kuzyk, J.-L. Ding, W. E. Johns, and D. J. Welker, "Fabrication and mechanical behavior of dye-doped polymer optical fiber," *J. Appl. Phys.*, vol. 92, pp. 04–Dec, 2002.

[61] D. Yang, J. Yu, X. Tao, and H. Tam, "Structural and mechanical properties of polymeric optical fiber," *Mat. Sci. Eng. A*, vol. 364, pp. 256–259, 2004.

[62] S. Kiesel, K. Peters, T. Hassan, and M. Kowalsky, "Behaviour of intrinsic polymer optical fibre sensor for large-strain applications," *Meas. Sci. Technol.*, vol. 18, pp. 3144–3154, 2007.

[63] A. Sophie, M. Patrick, O. Heidi, G. Thomas, T. Hugo, C. A. F. Marques, D. J. Webb, G.-D. Peng, P. Mergo, and B. Francis, "Thermal effects on the photoelastic coefficient of polymer optical fibers," *Opt. Lett.*, vol. 41, no. 11, pp. 2517–2520, 2016.

[64] D. Bosc and C. Toinen, "Tensile Mechanical-Properties and Reduced Internal-Stresses of Polymer Optical-Fiber," *Polym. Composites*, vol. 14, no. 5, pp. 410–413, 1993.

[65] C. A. Buckley, E. P. Lautenschlager, and J. L. Gilbert, "Deformation Processing of PMMA into High-Strength Fibers," *J. Appl. Polym. Sci.*, vol. 44, no. 8, pp. 1321–1330, 1992.

[66] T. Ishigure, M. Hirai, M. Sato, and Y. Koike, "Graded-index plastic optical fiber with high mechanical properties enabling easy network installations. II," *J. Appl. Polym. Sci.*, vol. 91, no. 1, pp. 410–416, 2004.

[67] A. Pospori, C. A. F. Marques, D. Sáez-Rodríguez, K. Nielsen, O. Bang, and D. J. Webb, "Thermal and chemical treatment of polymer optical fiber Bragg grating sensors for enhanced mechanical sensitivity," *Opt. Fiber Technol.*, vol. 36, pp. 68–74, 2017.

[68] C. R. Kurkjian, J. T. Krause, and M. J. Matthewson, "Strength and Fatigue of Silica Optical Fibers," *J. Lightwave Technol.*, vol. 7, no. 9, pp. 1360–1370, 1989.

[69] K. S. C. Kuang, S. T. Quek, C. G. Koh, W. J. Cantwell, and P. J. Scully, "Plastic Optical Fibre Sensors for Structural Health Monitoring: A Review of Recent Progress," *J. Sensors*, vol. 2009, p. 13, 2009.

[70] A. Abang and D. J. Webb, "Influence of mounting on the hysteresis of polymer fiber Bragg grating strain sensors," *Opt. Lett.*, vol. 38, no. 9, p. 1376, 2013.

[71] P. Kara, "Polymer optical fiber sensors–a review," *Smart Mater. Struct.*, vol. 20, no. 1, p. 013002, 2011.

[72] J. Pospíšil, Z. Horák, Z. Kruliš, S. Nešpůrek, and S. I. Kuroda, "Degradation and aging of polymer blends I. Thermomechanical and thermal degradation," *Polym. Degrad. Stab.*, vol. 65, no. 3, pp. 405–414, 1999.

[73] A. Göpferich, "Mechanisms of polymer degradation and erosion," *Biomaterials*, vol. 17, no. 2, pp. 103–114, 1996.

[74] R. W. Lenz, *Biodegradable polymers*. Springer Berlin Heidelberg, 1993.

[75] H. A. Larsen and H. G. Drickamer, "Mechanical Degradation and Cross Linking of Polymers by Plastic Deformation at High Pressure," *J. Phys. Chem.*, vol. 61, no. 12, pp. 1643–1646, 1957.

[76] R. B. Fox, L. G. Isaacs, and S. Stokes, "Photolytic degradation of poly(methyl methacrylate)," *J. Polym. Sci. A*, vol. 1, no. 3, pp. 1079–1086, 1963.

[77] B. G. Ranby and J. F. Rabek, *Photodegradation, photo-oxidation, and photostabilization of polymers*. New York, Wiley, 1975.

[78] A. Torikai, M. Ohno, and K. Fueki, "Photodegradation of poly(methyl methacrylate) by monochromatic light: Quantum yield, effect of wavelengths, and light intensity," *J. Appl. Polym. Sci.*, vol. 41, no. 5-6, pp. 1023–1032, 1990.

[79] L. E. Manring, "Thermal degradation of poly(methyl methacrylate). 4. Random side-group scission," *Macromolecules*, vol. 24, no. 11, pp. 3304–3309, 1991.

[80] Y. Takezawa, S. Tanno, N. Taketani, S. Ohara, and H. Asano, "Analysis of thermal degradation for plastic optical fibers," *J. Appl. Polym. Sci.*, vol. 42, no. 10, pp. 2811–2817, 1991.

[81] O. Ziemann, J. Krauser, P. E. Zamzow, and W. Daum, *POF handbook: optical short range transmission systems*. Springer Science & Business Media, 2008.

[82] K. Makino, T. Kado, A. Inoue, and Y. Koike, "Low loss graded index polymer optical fiber with high stability under damp heat conditions," *Opt. Express*, vol. 20, no. 12, pp. 12 893–12 898, 2012.

[83] W. Groh, "Overtone absorption in macromolecules for polymer optical fibers," *Macromol. Chem. Phys.*, vol. 189, no. 12, pp. 2861–2874, 1988.

[84] S. Ando, T. Matsuura, and S. Sasaki, "Perfluorinated polymers for optical waveguides," *ChemTech*, vol. 24, no. 12, pp. 20–27, 1994.

[85] T. Ishigure, Y. Koike, and J. W. Fleming, "Optimum index profile of the perfluorinated polymer-based GI polymer optical fiber and its dispersion properties," *J. Lightwave Technol.*, vol. 18, no. 2, pp. 178–184, 2000.

[86] Y. Ebihara, T. Ishigure, and Y. Koike, "Low dispersion perfluorinated polymer based graded index polymer optical fiber," in *54th SPSJ Annual Meeting*, 2005.

[87] M. Gaztelumendi and J. Nazabal, "Effects of extrusion conditions on the orientation and mechanical properties of high-impact polystyrene," *Eur. Polym. J.*, vol. 22, no. 1, pp. 79–81, 1986.

[88] O. Ziemann, W. Daum, A. Bräuer, J. Schlick, and W. Frank, "Results of a German 6.000 hours accelerated aging test of PMMA POF and consequences for the practical use of POF," in *9th Int. Conf. Plastic Optical Fibres*, 2000.

[89] R. Buczynski, "Photonic crystal fibers," *Acta. Phys. Pol. A*, vol. 106, no. 2, pp. 141–168, 2004.

[90] S. G. Leon-Saval, R. Lwin, and A. Argyros, "Multicore composite single-mode polymer fibre," *Opt. Exp.*, vol. 20, no. 1, pp. 141–148, 2012.

[91] K. Cook, J. Canning, S. Leon-Saval, Z. Reid, M. A. Hossain, J.-E. Comatti, Y. Luo, and G.-D. Peng, "Air-structured optical fiber drawn from a 3D-printed preform," *Opt. Lett.*, vol. 40, no. 17, pp. 3966–3969, 2015.

[92] O. Abdi, K. C. Wong, T. Hassan, K. J. Peters, and M. J. Kowalsky, "Cleaving of solid single mode polymer optical fiber for strain sensor applications," *Opt. Commun.*, vol. 282, no. 5, pp. 856–861, 2009.

[93] S. H. Law, J. D. Harvey, R. J. Kruhlak, M. Song, E. Wu, G. W. Barton, M. A. van Eijkelenborg, and M. C. J. Large, "Cleaving of microstructured polymer optical fibres," *Opt. Commun.*, vol. 258, pp. 193–202, 2006.

[94] S. H. Law, M. A. van Eijkelenborg, G. W. Barton, C. Yan, R. Lwin, and J. Gan, "Cleaved end-face quality of microstructured polymer optical fibres," *Opt. Commun.*, vol. 265, no. 2, pp. 513–520, 2006.

[95] D. Sáez-Rodríguez, K. Nielsen, O. Bang, and D. J. Webb, "Simple Room Temperature Method for Polymer Optical Fibre Cleaving," *J. Lightwave Technol.*, vol. 33, no. 23, pp. 4712–4716, 2015.

[96] R. Oliveira, L. Bilro, and R. Nogueira, "Smooth end face termination of microstructured, graded-index, and step-index polymer optical fibers," *Appl. Opt.*, vol. 54, no. 18, pp. 5629–5633, 2015.

[97] I. P. Johnson, D. J. Webb, K. Kalli, M. C. Large, and A. Argyros, "Multiplexed FBG sensor recorded in multimode microstructured polymer optical fibre," in *Photonic Crystal Fibres IV*. Proc. SPIE 7714, 2010.

[98] A. Abang, D. Saez-Rodriguez, K. Nielsen, O. Bang, and D. J. Webb, "Connectorisation of fibre Bragg grating sensors recorded in microstructured polymer optical fibre," in *Fifth European Workshop on Optical Fibre Sensors*. Proc. SPIE 8794, 2013.

[99] A. Abang and D. J. Webb, "Demountable connection for polymer optical fiber grating sensors," *Opt. Eng.*, vol. 51, no. 8, p. 080503, 2012.

[100] W. J. Tomlinson, I. P. Kaminow, E. A. Chandross, R. L. Fork, and W. T. Silfvast, "Photoinduced refractive index increase in poly (methylmethacrylate) and its applications," *Appl. Phys. Lett.*, vol. 16, no. 12, pp. 486–489, 1970.

[101] J. M. Moran and I. P. Kaminow, "Properties of holographic Gratings photoinduced in polymethyl methacrylate," *Appl. Opt.*, vol. 12, no. 8, pp. 1964–1970, 1973.

[102] G. D. Peng, Z. Xiong, and P. L. Chu, "Photosensitivity and gratings in dye-doped polymer optical fibers," *Opt. Fiber Technol.*, vol. 5, pp. 242–251, 1999.

[103] Z. Xiong, G. D. Peng, B. Wu, and P. L. Chu, "Highly tunable Bragg gratings in single-mode polymer optical fibers," *Photon. Technol. Lett.*, vol. 11, pp. 352–354, 1999.

[104] M. Kopietz, M. D. Lechner, D. G. Steinmeier, J. Marotz, H. Franke, and E. Krätzig, "Light-induced refractive index changes in polymethylmethacrylate (PMMA) blocks," *Polym. Photochem.*, vol. 5, no. 1, pp. 109–119, 1984.

[105] J. Marotz, "Holographic storage in sensitized polymethyl methacrylate blocks," *Appl. Phys. B*, vol. 37, no. 4, pp. 181–187, 1985.

[106] W. Schnabel, *Polymers and Light: Fundamentals and Technical Applications*. John Wiley and Sons, 2007.

[107] A. K. Baker and P. E. Dyer, "Refractive-index modification of polymethylmethacrylate (PMMA) thin films by KrF-laser irradiation," *Appl. Phys. A*, vol. 57, no. 6, pp. 543–544, 1993.

[108] T. Mitsuoka, A. Torikai, and K. Fueki, "Wavelength sensitivity of the photodegradation of poly(methyl methacrylate)," *J. Appl. Polym. Sci.*, vol. 47, no. 6, pp. 1027–1032, 1993.

[109] C. Wochnowski, S. Metev, and G. Sepold, "UV-laser-assisted modification of the optical properties of polymethylmethacrylate," *Appl. Surf. Sci.*, vol. 154, pp. 706–711, 2000.

[110] C. Wochnowski, M. A. Shams Eldin, and S. Metev, "UV-laser-assisted degradation of poly(methyl methacrylate)," *Polym. Degrad. Stab.*, vol. 89, no. 2, pp. 252–264, 2005.

[111] D. Sáez-Rodríguez, K. Nielsen, O. Bang, and D. J. Webb, "Photosensitivity mechanism of undoped poly(methyl methacrylate) under UV radiation at 325 nm and its spatial resolution limit," *Opt. Lett.*, vol. 39, no. 12, pp. 3421–3424, 2014.

[112] D. R. Tyler, "Mechanistic Aspects of the Effects of Stress on the Rates of Photochemical Degradation Reactions in Polymers," *J. Macromol. Sci. C*, vol. 44, no. 4, pp. 351–388, 2004.

[113] R. C. Estler and N. S. Nogar, "Mass spectroscopic identification of wavelength dependent UV laser photoablation fragments from polymethylmethacrylate," *Appl. Phys. Lett.*, vol. 49, no. 18, pp. 1175–1177, 1986.

[114] R. Srinivasan, B. Braren, R. W. Dreyfus, L. Hadel, and D. E. Seeger, "Mechanism of the ultraviolet laser ablation of polymethyl methacrylate at 193 and 248 nm: laser-induced fluorescence analysis, chemical analysis, and doping studies," *J. Opt. Soc. Am. B*, vol. 3, no. 5, pp. 785–791, 1986.

[115] S. Küper and M. Stuke, "UV-excimer-laser ablation of polymethylmethacrylate at 248 nm: Characterization of incubation sites with Fourier transform IR- and UV-Spectroscopy," *Appl. Phys. A*, vol. 49, no. 2, pp. 211–215, 1989.

[116] F. P. Laming, "Holographic grating formation in photopolymers–Polymethylmethacrylate," *Polym. Eng. Sci.*, vol. 11, no. 5, pp. 421–425, 1971.

[117] A. McNaught, A. Wilkinson, I. U. o. Pure, and A. Chemistry, *Compendium of Chemical Terminology: IUPAC Recommendations*. Blackwell Science, 1997.

[118] Y. Luo, Q. Zhang, H. Liu, and G. D. Peng, "Gratings fabrication in benzildimethylketal doped photosensitive polymer optical fibers using 355 nm nanosecond pulsed laser," *Opt. Lett.*, vol. 35, no. 5, pp. 751–3, 2010.

[119] D. Sáez-Rodríguez, K. Nielsen, H. K. Rasmussen, O. Bang, and D. J. Webb, "Highly photosensitive polymethyl methacrylate microstructured polymer optical fiber with doped core," *Opt. Lett.*, vol. 38, no. 19, pp. 3769–72, 2013.

[120] I. P. Kaminow, H. P. Weber, and E. A. Chandross, "Poly(methyl methacrylate) dye laser with internal diffraction grating resonator," *Appl. Phys.Lett.*, vol. 18, p. 497, 1971.

[121] R. M. Ahmed, "Optical Study on Poly(methyl methacrylate)/Poly(vinyl acetate) Blends," *Int. J. Photoenergy*, vol. 2009, pp. 1–7, 2009.

[122] H. Y. Liu, G. D. Peng, and P. L. Chu, "Polymer fiber Bragg gratings with 28-dB transmission rejection," *Photon. Technol. Lett.*, vol. 14, pp. 935–937, 2002.

[123] G. D. Peng and P. L. Chu, "Polymer optical fiber photosensitivities and highly tunable fiber gratings," *Fiber Integrated Opt.*, vol. 19, pp. 277–293, 2000.

[124] H. Dobb, K. Kalli, and D. J. Webb, "Temperature-insensitive long period grating sensors in photonic crystal fibre," *Electron. Lett.*, vol. 40, no. 11, pp. 657–658, 2004.

[125] H. Dobb, D. J. Webb, K. Kalli, A. Argyros, M. C. J. Large, and M. a. van Eijkelenborg, "Continuous wave ultraviolet light-induced fiber Bragg gratings in few- and single-mode microstructured polymer optical fibers." *Opt. Lett.*, vol. 30, pp. 3296–8, 2005.

[126] H. Y. Liu, G. D. Peng, and P. L. Chu, "Thermal tuning of polymer optical fiber Bragg gratings," *Photon. Technol. Lett.*, vol. 13, pp. 824–826, 2001.

[127] N. G. Harbach, "Fiber Bragg gratings in polymer optical fibers," Ph.D. dissertation, Ecole Polytechnique Federale de Lausanne, 2008.

[128] K. Nielsen, H. K. Rasmussen, A. J. L. Adam, P. C. M. Planken, O. Bang, and P. U. Jepsen, "Bendable, low-loss Topas fibers for the terahertz frequency range," *Opt. Express*, vol. 17, no. 10, pp. 8592–8601, 2009.

[129] W. Yuan, L. Khan, D. J. Webb, K. Kalli, H. K. Rasmussen, A. Stefani, and O. Bang, "Humidity insensitive TOPAS polymer fiber Bragg grating sensor," *Opt. Express*, vol. 19, pp. 19 731–19 739, 2011.

[130] W. Zhang, D. Webb, and G. Peng, "Polymer optical fiber Bragg grating acting as an intrinsic biochemical concentration sensor," *Opt. Lett.*, vol. In press, 2012.

[131] A. Stefani, S. Andresen, W. Yuan, and O. Bang, "Dynamic Characterization of Polymer Optical Fibers," *J. Sensors*, vol. 12, pp. 3047–3053, 2012.

[132] H. Kogelnik, "Coupled Wave Theory for Thick Hologram Gratings," *Bell Syst. Tech. J.*, vol. 48, no. 9, pp. 2909–2947, 1969.

[133] S. Kiesel, P. Van Vickle, K. Peters, T. Hassan, and M. Kowalsky, "Intrinsic polymer optical fiber sensors for high-strain applications," in *ASME 2005 Int. Mechan. Eng. Congress and Exposition*. Proc. SPIE 6167, 2006.

[134] Z. F. Zhang and X. M. Tao, "Synergetic Effects of Humidity and Temperature on PMMA Based Fiber Bragg Gratings," *J. Lightwave Technol.*, vol. 30, pp. 841–845, 2012.

[135] W. Zhang and D. J. Webb, "Humidity responsivity of poly(methyl methacrylate)-based optical fiber Bragg grating sensors," *Opt. Lett.*, vol. 39, no. 10, pp. 3026–3029, 2014.

[136] H. Singh and M. Zippin, "Apodized fiber Bragg gratings for DWDM applications using uniform phase mask," in *24th European Conf. on Optical Commun.* IEEE, 1998.

[137] F. Ouellette, "Dispersion cancellation using linearly chirped Bragg grating filters in optical waveguides," *Opt. Lett.*, vol. 12, no. 10, pp. 847–849, 1987.

[138] R. I. Laming, W. H. Loh, X. Gu, M. N. Zervas, M. J. Cole, and A. D. Ellis, "Dispersion compensation with chirped fiber Bragg grating to 400 km at 10 Gbit/s in nondispersion-shifted fiber," in *Optical Fiber Commun.* IEEE, 1996.

[139] Z. C. Li, H. Y. Tam, L. X. Xu, and Q. J. Zhang, "Fabrication of long-period gratings in poly(methyl methacrylate-co-methyl vinyl ketone-cobenzyl methacrylate)-core polymer optical fiber by use of a mercury lamp," *Opt. Lett.*, vol. 30, pp. 1117–1119, 2005.

[140] W. J. Stephen and P. T. Ralph, "Optical fibre long-period grating sensors: characteristics and application," *Meas. Sci. Technol.*, vol. 14, no. 5, p. R49, 2003.

[141] V. Bhatia, "Applications of long-period gratings to single and multi-parameter sensing," *Opt. Express*, vol. 4, no. 11, pp. 457–466, 1999.

[142] V. Bhatia, D. K. Campbell, D. Sherr, T. G. DâĂŹAlberto, N. A. Zabaronick, G. A. Ten Eyck, K. A. Murphy, and R. O. Claus, "Temperature-insensitive and strain-insensitive long-period grating sensors for smart structures," *Opt. Eng.*, vol. 36, no. 7, pp. 1872–1876, 1997.

[143] X. Hu, C.-F. J. Pun, H.-Y. Tam, P. MÃl'gret, and C. Caucheteur, "Tilted Bragg gratings in step-index polymer optical fiber," *Opt. Lett.*, vol. 39, no. 24, pp. 6835–6838, 2014.

[144] Y. Chun, W. Yong, and X. Chang-Qing, "A novel method to measure modal power distribution in multimode fibers using tilted fiber Bragg gratings," *Photon. Technol. Lett.*, vol. 17, no. 10, pp. 2146–2148, 2005.

[145] K. Zhou, X. Chen, L. Zhang, and I. Bennion, "Optical chemsensors based on etched fibre Bragg gratings in D-shape and multimode fibres," in *Int. Society for Opt. and Photon.* Proc. SPIE 5855, 2005.

[146] G. Laffont and P. Ferdinand, "Tilted short-period fibre-Bragg-grating-induced coupling to cladding modes for accurate refractometry," *Meas. Sci. Technol.*, vol. 12, no. 7, p. 765, 2001.

[147] K. O. Hill, Y. Fujii, D. C. Johnson, and B. S. Kawasaki, "Photosensitivity in optical fiber waveguides: Application to reflection filter fabrication," *Appl. Phys. Lett.*, vol. 32, no. 10, pp. 647–649, 1978.

[148] K. O. Hill, B. Malo, F. Bilodeau, D. C. Johnson, and J. Albert, "Bragg gratings fabricated in monomode photosensitive optical fiber by UV exposure through a phase mask," *Appl. Phys. Lett.*, vol. 62, no. 10, pp. 1035–1037, 1993.

[149] Z. Xiong, G. D. Peng, B. Wu, and P. L. Chu, "Effects of the zeroth-order diffraction of a phase mask on Bragg gratings," *J. Lightwave Tech.*, vol. 17, no. 11, pp. 2361–2365, 1999.

[150] A. Othonos and X. Lee, "Novel and improved methods of writing Bragg gratings with phase masks," *Photon. Technol. Lett.*, vol. 7, no. 10, pp. 1183–1185, 1995.

[151] R. J. Campbell and R. Kashyap, "Spectral profile and multiplexing of Bragg gratings in photosensitive fiber," *Opt. Lett.*, vol. 16, no. 12, pp. 898–900, 1991.

[152] A. Martinez, M. Dubov, I. Khrushchev, and I. Bennion, "Direct writing of fibre Bragg gratings by femtosecond laser," *Electron. Lett.*, vol. 40, no. 19, pp. 1170–1172, 2004.

[153] A. Royon, *Nonlinear femtosecond near infrared laser structuring in oxide glasses*. ProQuest, 2009.

[154] S. J. Mihailov, C. W. Smelser, P. Lu, R. B. Walker, D. Grobnic, H. Ding, G. Henderson, and J. Unruh, "Fiber Bragg gratings made with a phase mask and 800-nm femtosecond radiation," *Opt. Lett.*, vol. 28, no. 12, pp. 995–997, 2003.

[155] K. Zhou, M. Dubov, C. Mou, L. Zhang, V. K. Mezentsev, and I. Bennion, "Line-by-Line Fiber Bragg Grating Made by Femtosecond Laser," *Photon. Technol. Lett.*, vol. 22, no. 16, pp. 1190–1192, 2010.

[156] A. Theodosiou, A. Lacraz, M. Polis, K. Kalli, M. Tsangari, A. Stassis, and M. Komodromos, "Modified fs-Laser Inscribed FBG Array for Rapid Mode Shape Capture of Free-Free Vibrating Beams," *Photon. Technol. Lett.*, vol. 28, no. 14, pp. 1509–1512, 2016.

[157] K. Kalli, C. Koutsides, E. Davies, M. Komodromos, D. J. Webb, and L. Zhang, "Femtosecond laser inscribed superstructure fibre gratings," in *21st Int. Conf. on Opt. Fibre Sensors*. Proc. SPIE 7753, 2011.

[158] K. Kalli, C. Riziotis, A. Posporis, C. Markos, C. Koutsides, S. Ambran, A. S. Webb, C. Holmes, J. C. Gates, J. K. Sahu, and P. G. R. Smith, "Flat fibre and femtosecond laser technology as a novel photonic integration platform for optofluidic based biosensing devices and lab-on-chip applications: Current results and future perspectives," *Sens. Actuators B Chem.*, vol. 209, pp. 1030–1040, 2015.

[159] Y.-L. Zhang, Q.-D. Chen, H. Xia, and H.-B. Sun, "Designable 3D nanofabrication by femtosecond laser direct writing," *Nano Today*, vol. 5, no. 5, pp. 435–448, 2010.

[160] B. P. Abbott, R. Abbott, T. Abbott, M. Abernathy, F. Acernese, K. Ackley, C. Adams, T. Adams, P. Addesso, R. Adhikari *et al.*, "Observation of Gravitational Waves from a Binary Black Hole Merger," *Phys. Rev. Lett.*, vol. 116, no. 6, p. 061102, 2016.

[161] D. Gardner, T. Hofler, S. Baker, R. Yarber, and S. Garrett, "A fiber-optic interferometric seismometer," *J. Lightwave Technol.*, vol. 5, no. 7, pp. 953–960, 1987.

[162] B. T. Cox, E. Z. Zhang, J. G. Laufer, and P. C. Beard, "Fabry Perot polymer film fibre-optic hydrophones and arrays for ultrasound field characterisation," *J. Phys. Conf. Ser.*, vol. 1, no. 1, p. 32, 2004.

[163] A. Pospori and D. J. Webb, "Stress Sensitivity Analysis of Optical Fiber Bragg Grating Based Fabry-Pérot Interferometric Sensors," *J. Lightwave Technol.*, vol. PP, no. 99, pp. 1–1, 2017.

[164] A. Yariv, "Coupled-mode theory for guided-wave optics," *J. Quantum Electron.*, vol. 9, no. 9, pp. 919–933, 1973.

[165] H. Kogelnik, "Filter Response of Nonuniform Almost-Periodic Structures," *Bell Syst. Tech. J.*, vol. 55, no. 1, pp. 109–126, 1976.

[166] T. Erdogan, "Fiber grating spectra," *J. Lightwave Technol.*, vol. 15, no. 8, pp. 1277–1294, 1997.

[167] Y. O. Barmenkov, D. Zalvidea, S. Torres-Peiró, J. L. Cruz, and M. V. Andrés, "Effective length of short Fabry-Perot cavity formed by uniform fiber Bragg gratings," *Opt. Express*, vol. 14, no. 14, pp. 6394–6399, 2006.

[168] C. D. Butter and G. B. Hocker, "Fiber optics strain gauge," *Appl. Opt.*, vol. 17, no. 18, pp. 2867–2869, 1978.

[169] I. H. Malitson, "Interspecimen Comparison of the Refractive Index of Fused Silica," *J. Opt. Soc. Am.*, vol. 55, no. 10, pp. 1205–1208, 1965.

[170] N. Sultanova, S. Kasarova, and I. Nikolov, "Dispersion properties of optical polymers," *Acta. Phys. Pol. A*, vol. 116, no. 4, pp. 585–587, 2009.

[171] R. M. Waxler, D. Horowitz, and A. Feldman, "Optical and physical parameters of Plexiglas 55 and Lexan," *Appl. Opt.*, vol. 18, no. 1, pp. 101–104, 1979.

[172] A. Bertholds and R. Dandliker, "Determination of the individual strain-optic coefficients in single-mode optical fibres," *J. Lightwave Technol.*, vol. 6, no. 1, pp. 17–20, 1988.

[173] D. D. Raftopoulos, D. Karapanos, and P. S. Theocaris, "Static and dynamic mechanical and optical behaviour of high polymers," *J. Phys. D: Appl. Phys.*, vol. 9, no. 5, p. 869, 1976.

[174] P. Stajanca, O. Cetinkaya, M. Schukar, P. Mergo, D. J. Webb, and K. Krebber, "Molecular alignment relaxation in polymer optical fibers for sensing applications," *Opt. Fiber Technol.*, vol. 28, pp. 11–17, 2016.

[175] G. B. Blanchet, P. Cotts, and C. R. Fincher, "Incubation: Subthreshold ablation of poly-(methyl methacrylate) and the nature of the decomposition pathways," *J. Appl. Phys.*, vol. 88, no. 5, pp. 2975–2978, 2000.

[176] H. Schmidt, J. Ihlemann, B. Wolff-Rottke, K. Luther, and J. Troe, "Ultraviolet laser ablation of polymers: spot size, pulse duration, and plume attenuation effects explained," *J. Appl. Phys.*, vol. 83, no. 10, pp. 5458–5468, 1998.

[177] H. B. Liu, H. Y. Liu, G. D. Peng, and P. L. Chu, "Novel Growth Behaviors of Fiber Bragg Gratings in Polymer Optical Fiber Under UV Irradiation With Low Power," *Photon. Technol. Lett.*, vol. 16, no. 1, pp. 159–161, 2004.

[178] X. Hu, D. Kinet, P. Megret, and C. Caucheteur, "Control over photo-inscription and thermal annealing to obtain high-quality Bragg gratings in doped PMMA optical fibers," *Opt. Lett.*, vol. 41, no. 13, pp. 2930–3, 2016.

[179] K. E. Carroll, C. Zhang, D. J. Webb, K. Kalli, A. Argyros, and M. C. Large, "Thermal response of Bragg gratings in PMMA microstructured optical fibers," *Opt. Express*, vol. 15, no. 14, pp. 8844–50, 2007.

[180] G. Rajan, B. Liu, Y. H. Luo, E. Ambikairajah, and G. D. Peng, "High Sensitivity Force and Pressure Measurements Using Etched Singlemode Polymer Fiber Bragg Gratings," *Sensors*, vol. 13, no. 5, pp. 1794–1800, 2013.

[181] G. Rajan, Y. M. Noor, B. Liu, E. Ambikairaja, D. J. Webb, and G.-D. Peng, "A fast response intrinsic humidity sensor based on an etched singlemode polymer fiber Bragg grating," *Sens. Actuators A Phys.*, vol. 203, pp. 107–111, 2013.

[182] K. Bhowmik, G. D. Peng, Y. H. Luo, E. Ambikairajah, V. Lovric, W. R. Walsh, and G. Rajan, "High Intrinsic Sensitivity Etched Polymer Fiber Bragg Grating Pair for Simultaneous Strain and Temperature Measurements," *Sensors*, vol. 16, no. 8, pp. 2453–2459, 2016.

[183] D. Cohn and A. Hotovely Salomon, "Designing biodegradable multiblock PCL/PLA thermoplastic elastomers," *Biomaterials*, vol. 26, no. 15, pp. 2297–2305, 2005.

[184] A. Stefani, S. Andresen, W. Yuan, N. Herholdt-Rasmussen, and O. Bang, "High Sensitivity Polymer Optical Fiber-Bragg-Grating-Based Accelerometer," *Photon. Technol. Lett.*, vol. 24, pp. 763–765, 2012.

[185] Y. Termonia and P. Smith, "Kinetic-Model for Tensile Deformation of Polymers," *Macromolecules*, vol. 20, no. 4, pp. 835–838, 1987.

[186] J. De Boer, "The influence of van der Waals' forces and primary bonds on binding energy, strength and orientation, with special reference to some artificial resins," *J. Chem. Soc. Faraday Trans.*, vol. 32, pp. 10–37, 1936.

[187] G. Yeh, R. Hosemann, J. Loboda-Čačković, and H. Čačković, "Annealing effects of

polymers and their underlying molecular mechanisms," *Polym. J.*, vol. 17, no. 4, pp. 309–318, 1976.

[188] K. Schmidt-Rohr, A. S. Kulik, H. W. Beckham, A. Ohlemacher, U. Pawelzik, C. Boeffel, and H. W. Spiess, "Molecular Nature of the Beta-Relaxation in Poly(Methyl Methacrylate) Investigated by Multidimensional NMR," *Macromolecules*, vol. 27, no. 17, pp. 4733–4745, 1994.

[189] E. Muzeau, J. Perez, and G. P. Johari, "Mechanical Spectrometry of the Beta-Relaxation in Poly(Methyl Methacrylate)," *Macromolecules*, vol. 24, no. 16, pp. 4713–4723, 1991.

[190] S. C. Kuebler, D. J. Schaefer, C. Boeffel, U. Pawelzik, and H. W. Spiess, "2D Exchange NMR Investigation of the Îś-Relaxation in Poly(ethyl methacrylate) as Compared to Poly(methyl methacrylate)," *Macromolecules*, vol. 30, no. 21, pp. 6597–6609, 1997.

[191] J. F. de Deus, G. P. Souza, W. A. Corradini, T. D. Z. Atvars, and L. Akcelrud, "Relaxations of Poly(methyl methacrylate) Probed by Covalently Attached Anthryl Groups," *Macromolecules*, vol. 37, no. 18, pp. 6938–6944, 2004.

[192] J. J. Tribone, J. M. O'Reilly, and J. Greener, "Analysis of enthalpy relaxation in poly(methyl methacrylate): effects of tacticity, deuteration, and thermal history," *Macromolecules*, vol. 19, no. 6, pp. 1732–1739, 1986.

[193] W. Zhang and D. J. Webb, "Factors influencing the temperature sensitivity of PMMA based optical fiber Bragg gratings," in *Micro-Structured and Specialty Optical Fibres III*. Proc. SPIE 9128, 2014.

[194] K. S. Lim, H. Z. Yang, W. Y. Chong, Y. K. Cheong, C. H. Lim, N. M. Ali, and H. Ahmad, "Axial contraction in etched optical fiber due to internal stress reduction," *Opt. Express*, vol. 21, no. 3, pp. 2551–62, 2013.

[195] P. L. Chu and T. Whitbread, "Measurement of stresses in optical fiber and preform," *Appl. Opt.*, vol. 21, no. 23, pp. 4241–4245, 1982.

[196] P. Ji, A. D. Li, and G.-D. Peng, "Transverse birefringence in polymer optical fiber introduced in drawing process," in *Optical Science and Technology, SPIE's 48th Annual Meeting*. Proc. SPIE 5212, 2003.

[197] M. K. Szczurowski, T. Martynkien, G. Statkiewicz-Barabach, W. Urbanczyk, L. Khan, and D. J. Webb, "Measurements of stress-optic coefficient in polymer optical fibers," *Opt. Lett.*, vol. 35, pp. 2013–2015, 2010.

[198] J. R. Saffell and A. H. Windle, "The influence of thermal history on internal stress distributions in sheets of PMMA and polycarbonate," *J. Appl. Polym. Sci.*, vol. 25, no. 6, pp. 1117–1129, 1980.

[199] R. P. De Paula, J. H. Cole, and J. A. Bucaro, "Ultrasonic Sensing From 100 kHz to 50 MHz Using Single Mode Optical Fiber," in *Fiber Optic and Laser Sensors I*. Proc. SPIE 0412, 1983.

[200] B. Yun, N. Chen, and Y. Cui, "Highly Sensitive Liquid-Level Sensor Based on Etched Fiber Bragg Grating," *Photon. Technol. Lett.*, vol. 19, no. 21, pp. 1747–1749, 2007.

[201] G. Tuan, Z. Qida, D. Qingying, Z. Hao, X. Lifang, H. Guiling, and D. Xiaoyi, "Temperature-insensitive fiber Bragg grating liquid-level sensor based on bending cantilever beam," *Photon. Technol. Lett.*, vol. 17, no. 11, pp. 2400–2402, 2005.

[202] H. Fu, X. Shu, A. Zhang, W. Liu, L. Zhang, S. He, and I. Bennion, "Implementation and Characterization of Liquid-Level Sensor Based on a Long-Period Fiber Grating Mach-Zehnder Interferometer," *Sensors*, vol. 11, no. 11, pp. 2878–2882, 2011.

[203] C. Mou, K. Zhou, Z. Yan, H. Fu, and L. Zhang, "Liquid level sensor based on an excessively tilted fibre grating," *Opt. Commun.*, vol. 305, pp. 271–275, 2013.

[204] B. Gu, W. Qi, Y. Zhou, Z. Wu, P. P. Shum, and F. Luan, "Reflective liquid level sensor based on modes conversion in thin-core fiber incorporating tilted fiber Bragg grating," *Opt. Express*, vol. 22, no. 10, pp. 11 834–11 839, 2014.

[205] D. Sengupta and P. Kishore, "Continuous liquid level monitoring sensor system using fiber Bragg grating," *Opt. Eng.*, vol. 53, no. 1, pp. 017 102–017 102, 2014.

[206] B. C. Yao, Y. Wu, D. J. Webb, J. H. Zhou, Y. J. Rao, A. Pospori, C. B. Yu, Y. Gong, Y. F. Chen, and Z. G. Wang, "Graphene-Based D-Shaped Polymer FBG for Highly Sensitive Erythrocyte Detection," *Photon. Technol. Lett.*, vol. 27, no. 22, pp. 2399–2402, 2015.

[207] W. K. Purves, G. H. Orians, D. Sadava, and H. C. Heller, *Life: The Science of Biology: Volume III: Plants and Animals*. Macmillan, 2003, vol. 3.

[208] H. Huber, S. M. Lewis, and L. Szur, "The Influence of Anaemia, Polycythaemia and Splenomegaly on the Relationship between Venous Haematocrit and Red-Cell Volume," *British Journal of Haematology*, vol. 10, no. 4, pp. 567–575, 1964.

[209] J. Schmitt, "Method and apparatus for improving the accuracy of noninvasive hematocrit measurements," 2003, US Patent 6,606,509. [Online]. Available: https://www.google.com/patents/US6606509

[210] F. Schedin, A. K. Geim, S. V. Morozov, E. W. Hill, P. Blake, M. I. Katsnelson, and K. S. Novoselov, "Detection of individual gas molecules adsorbed on graphene," *Nat. Mater.*, vol. 6, no. 9, pp. 652–655, 2007.

[211] Z. Wang, Y. Chen, P. Li, X. Hao, J. Liu, R. Huang, and Y. Li, "Flexible Graphene-Based Electroluminescent Devices," *ACS Nano*, vol. 5, no. 9, pp. 7149–7154, 2011.

[212] D. Ott, I. Divliansky, B. Anderson, G. Venus, and L. Glebov, "Scaling the spectral beam combining channels in a multiplexed volume Bragg grating," *Opt. Exp.*, vol. 21, no. 24, pp. 29 620–29 627, 2013.

[213] T. yuan Chung, A. Rapaport, V. Smirnov, L. B. Glebov, M. C. Richardson, and M. Bass, "Solid-state laser spectral narrowing using a volumetric photothermal refractive Bragg grating cavity mirror," *Opt. Lett.*, vol. 31, no. 2, pp. 229–231, 2006.

[214] B. L. Volodin, S. V. Dolgy, E. D. Melnik, E. Downs, J. Shaw, and V. S. Ban, "Wavelength stabilization and spectrum narrowing of high-power multimode laser diodes and arrays by use of volume Bragg gratings," *Opt. Lett.*, vol. 29, no. 16, pp. 1891–1893, 2004.

[215] O. Andrusyak, V. Smirnov, G. Venus, and L. Glebov, "Beam combining of lasers with high spectral density using volume Bragg gratings," *Opt. Commun.*, vol. 282, no. 13, pp. 2560 – 2563, 2009.

[216] Y. Xie, Q. Ding, M. Kang, W. Li, Z. Li, and B. Wang, "Study on measuring refractive index modulation of volume phase holographic gratings," *Optik*, vol. 125, no. 13, pp. 3366–3369, 2014.

[217] M. R. Forshaw, "Explanation of the two-ring diffraction phenomenon observed by moran and kaminow," *Appl. Opt.*, vol. 13, no. 1, p. 2, 1974.

[218] K. A. Peterson, A. D. Stein, and M. D. Fayer, "Quantitative measurement of chain contraction in a solid blend of two incompatible polymers: poly(methyl methacrylate)/poly(vinyl acetate)," *Macromolecules*, vol. 23, no. 1, pp. 111–120, 1990.

[219] C. A. F. Marques, L. B. Bilro, N. J. Alberto, D. J. Webb, and R. N. Nogueira, "Narrow bandwidth Bragg gratings imprinted in polymer optical fibers for different spectral windows," *Opt. Commun.*, vol. 307, pp. 57–61, 2013.

A Publications arising from the work described in this thesis

Journal articles

1. **A. Pospori**, C. A.F. Marques, D. J. Webb, P. André, "Polymer optical fiber Bragg grating inscription with a single UV laser pulse," *Opt. Express*, vol. 25, no. 8, pp. 9028-9038, 2017.

2. C.A. F. Marques, **A. Pospori**, D. J. Webb, "Time-dependent variation of POF Bragg grating reflectivity and wavelength submerged in different liquids," *Opt. Laser Technol.*, vol. 94, pp. 234-239, 2017.

3. **A. Pospori**, D. J. Webb, "Stress Sensitivity Analysis of Polymer Optical Fiber Based Fabry-Pérot Interferometric Sensor," *J. Lightwave Technol.*, vol. 35, no. 13, 2017.

4. C. A. F. Marques, **A. Pospori**, G. Demirci, O. Çetinkaya, B. Gawdzik, P. Antunes, O. Bang, P. Mergo, P. André, D. J. Webb, "Fast Bragg Grating Inscription in PMMA Polymer Optical Fibres: Impact of Thermal Pre-Treatment of Preforms," *Sensors*, vol. 17, no. 4, p. 891, 2017.

5. **A. Pospori**, C. A. F. Marques, D. Sáez-Rodríguez, K. Nielsen, O. Bang, D. J. Webb,

"Thermal and chemical treatment of polymer optical fiber Bragg grating sensors for enhanced mechanical sensitivity," *Opt. Fiber Technol.*, vol. 36, pp. 68-74, 2017.

6. C. A. F. Marques, **A. Pospori**, D. Sáez-Rodríguez, K. Nielsen, O. Bang, D. J. Webb, "Aviation fuel gauging sensor utilizing multiple diaphragm sensors incorporating polymer optical fiber Bragg gratings," *Sensors*, vol. 16, no. 15, pp. 6122-6129, 2016.

7. B. Yao, Y. Wu, D. J. Webb, J. Zhou, Y. Rao, **A. Pospori**, C. Yu, Y. Gong, Y. Chen, "Graphene-Based D-Shaped Polymer FBG for Highly Sensitive Erythrocyte Detection," *Photon. Technol. Lett.*, vol. 27, no. 22, pp. 2399-2402, 2015.

Conference papers

8. C. A. F. Marques, **A. Pospori**, L. Pereira, S. Marques, P. Antunes, O. Bang, D. J. Webb, and P. André, "High-quality phase-shifted Bragg grating sensor inscribed with only one laser pulse in a polymer optical fiber," in *International Microwave and Optoelectronics Conference*, 2017. (In press)

9. G. Sagias, **A. Pospori**, D. J. Webb, H. L. Rivera, "Wavelength tuning of polymer optical fibre Bragg grating at longer wavelengths permanently," Proc. SPIE 10453 in *Third International Conference on Applications of Optics and Photonics*, 1045333, 2017.

10. C. A. F. Marques, **A. Pospori**, P. Mergo, P. André, D. J. Webb, "Impact of thermal pre-treatment on preforms for fast Bragg gratings inscription using undoped PMMA POFs," Proc. SPIE 10232 in *Optics & Optoelectronics*, Micro-structured and Specialty Optical Fibres V, 102320A, 2017.

11. **A. Pospori**, C. A. F. Marques, D. Sáez-Rodríguez, K. Nielsen, O. Bang, D. J. Webb, "Annealing and etching effects on strain and stress sensitivity of polymer optical fibre Bragg grating sensors," in *25th International Conference on Plastic Optical Fibres*, published by Aston University Research Archive, pp. 260-263, ISBN: 9781854494085, 2016.

12. C. A. F. Marques, **A. Pospori**, G. Demirci, O. Çetinkaya, B. Gawdzik, P. Antunes, O. Bang, P. Mergo, P. André, D. J. Webb, "Bragg gratings inscription using PMMA polymer optical fibers drawn from preforms with specific thermal pre-treatment," in *25th International Conference on Plastic Optical Fibres*, published by Aston University Research Archive, pp. 40-45, ISBN: 9781854494085, 2016.

13. **A. Pospori**, C. A. F. Marques, D. Sáez-Rodríguez, K. Nielsen, O. Bang, D. J. Webb, "Sensitivity enhancement using annealed polymer optical-fibre-based sensors for pressure sensing application," Proc. SPIE 9916 in *Sixth European Workshop on Optical Fibre Sensors (EWOFS)*, 99160E, 2016.

14. **A. Pospori**, D. J. Webb, "Performance analysis of polymer optical fibre based Fabry-Pérot sensor formed by two uniform Bragg gratings," Proc. SPIE 9886 in *Photonics Europe*, Micro-Structured and Specialty Optical Fibres IV, 98861F, 2016.

15. **A. Pospori**, C. A. F. Marques, M. G. Zubel, D. Sáez-Rodríguez, K Nielsen, O. Bang, D. J. Webb, "Annealing effects on strain and stress sensitivity of polymer optical fibre based sensors," Proc. SPIE 9886 in *Photonics Europe*, Micro-Structured and Specialty Optical Fibres IV, 98860V, 2016.

16. C. A. F. Marques, **A. Pospori**, D. Sáez-Rodríguez, K. Nielsen, O. Bang, D. J. Webb, "Fuel level sensor based on polymer optical Fiber Bragg gratings for aircraft applications," Proc. SPIE 9886 in *Photonics Europe*, Micro-Structured and Specialty Optical Fibres IV, 98860W, 2016.

17. C. Broadway, D. Gallego, **A. Pospori**, M. Zubel, D. J. Webb, K. Sugden, G. Carpintero, H. Lamela, "Microstructured polymer optical fibre sensors for opto-acoustic endoscopy," Proc. SPIE 9886 in *Photonics Europe*, Micro-Structured and Specialty Optical Fibres IV, 98860S, 2016.

18. C. Broadway, D. Gallego, **A. Pospori**, M. Zubel, D. J. Webb, K. Sugden, G. Carpintero, H. Lamela, "A compact polymer optical fibre ultrasound detector," Proc. SPIE 9708 in *Photonics West BiOS*, Photons Plus Ultrasound: Imaging and Sensing 2016, 970813, 2016.

19. C. A. F. Marques, **A. Pospori**, D. Sáez-Rodríguez, K. Nielsen, O. Bang, D. J. Webb, "High performance liquid-level sensor based on mPOFBG for aircraft applications," in *IEEE Avionics and Vehicle Fiber-Optics and Photonics Conference (AVFOP)*, ISBN: 9781479974825, 2015.

20. **A. Pospori**, D. J. Webb, "Optimisation of polymer optical fibre based interferometric sensors," Proc. SPIE 9507 in *Optics & Optoelectronics*, Micro-structured and Specialty Optical Fibres IV, 95070M, 2015.

21. C. A. F. Marques, **A. Pospori**, D. Sáez-Rodríguez, K. Nielsen, O. Bang, D. J. Webb, "Fiber optic liquid level monitoring system using microstructured polymer fiber Bragg grating

array sensors: performance analysis," Proc. SPIE 9634 in *International Conference on Optical Fibre Sensors (OFS24)*, 96345V, 2015.

22. C. Broadway, D. Gallego, G. Woyessa, **A. Pospori**, O. Bang, D. J. Webb, G. Carpintero, H. Lamela, "Polymer Optical Fibre Sensors for Endoscopic Opto-Acoustic Imaging," Proc. SPIE 9539 in *European Conference on Biomedical Optics*, Opto-Acoustic Methods and Applications in Biophotonics II, 953907, 2015.

23. C. Broadway, D. Gallego, G. Woyessa, **A. Pospori**, G. Carpintero, O. Bang, K. Sugden, H. Lamela, "Fabry-Pérot micro-structured polymer optical fibre sensors for opto-acoustic endoscopy," Proc. SPIE 9531 in *Biophotonics South America*, 953116, 2015.